

Scuola Internazionale Superiore di Studi Avanzati
Condensed Matter Theory and Simulation Sector



Dynamics of doped ^4He and ^3He clusters from reptation quantum Monte Carlo

A thesis submitted for the degree of
Doctor Philosophiæ

Candidate:
Tatjana Škrbić

Supervisors:
Dr. Saverio Moroni
Prof. Stefano Baroni

December 2009

Contents

Introduction	1
1 Quantum Monte Carlo	7
1.1 The Metropolis algorithm	8
1.2 Langevin dynamics	9
1.3 Variational Monte Carlo	10
1.3.1 Wave function optimization	11
1.4 Diffusion Monte Carlo	12
1.5 Reptation Monte Carlo	14
1.5.1 The original formulation	14
1.5.2 Excited states	17
2 Implementation: doped He clusters	19
2.1 The model system	19
2.2 Algorithm	21
2.3 Rotational energies	23
2.4 Convergence issues	25
3 CO-doped ^4He clusters	29
3.1 Effect of the anisotropy: CO <i>vs</i> HCN	33
3.2 Structural properties	35
3.3 Vibrational shift	39
3.4 Rotational excitations	46
3.5 Combining experimental and simulation data	48

4	Fine features in the spectra of doped ^4He clusters	51
4.1	Theory	52
4.2	$\text{CO-}^4\text{He}$	55
4.3	Line splittings and assignments in $\text{CO@}^4\text{He}_N$ clusters	57
4.4	Satellite band in $\text{CO}_2\text{@}^4\text{He}_N$ clusters	63
4.4.1	The ring model	63
4.4.2	Results and discussion	65
5	^3He clusters	69
5.1	Small doped mixed $^3\text{He}/^4\text{He}$ clusters	71
5.2	Fermionic excitations	74
5.2.1	A toy problem	76
5.3	Small doped ^3He clusters	78
5.3.1	Theory	79
5.3.2	Results and discussion	83
	Conclusions	89
A	More details on the spectra of CO isotopomers	91
A.1	Rotational energies of CO isotopomers	91
A.2	Separation of rotational and vibrational effects	96
B	Coupling of antisymmetrized single particle orbitals	101
B.1	General procedure	101
B.2	An example	102
	Bibliography	105
	Acknowledgments	111

Introduction

The spectroscopic investigation of single molecules solvated in He droplets of nanoscopic dimensions (containing $\sim 10^3$ – 10^4 atoms) was first attempted after Scoles *et al.* developed the so-called Helium Nanodroplet Isolation (HENDI) spectroscopy technique [1, 2]. The goal was to establish He droplets as an *ultimate spectroscopic matrix* [3], since the large zero-point motion that prevents He from solidifying even down to absolute zero, along with the weakness of interatomic interactions and the ultracold environment it provides, are expected to lead to a much better spectral resolution than achieved with conventional matrices. Another fundamental aspect became apparent soon when the resolution of molecular spectra appeared one order of magnitude larger than expected [4]. In the celebrated *microscopic Andronikashvili experiment* by Toennies *et al.* [5] it was demonstrated that the sharpness of the rotational lines of carbonyl sulphide (OCS) molecule solvated in ^4He nanodroplets—resembling the spectra and the symmetry of a free rotor in the gas-phase, although with a renormalized rotational constant—is a manifestation of superfluidity of ^4He in such extremely confined conditions. This stood in contrast with the spectra recorded in fermionic ^3He nanodroplets that displayed only one broad and structureless transition. This discovery prompted a thorough experimental and theoretical effort targeting small and medium-sized doped ^4He clusters [6, 7, 8], aiming at understanding how the phenomenon of superfluidity arises at the atomic scale and evolves with the size of the system.

The main feature of the rotational spectra of the molecules solvated in ^4He is a non-classical rotational inertia (NCRI), observed as a function of the cluster size N , which leads to an energy spectrum closely resembling that of a free rotor, although with a reduced effective rotational constant

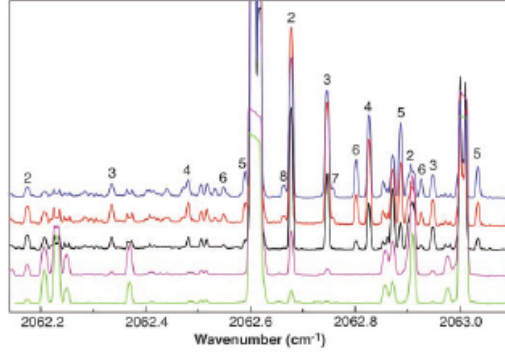


Figure 1: Part of the roto-vibrational spectra of $\text{OCS}@^4\text{He}_N$ clusters (Ref. [6]), observed in the region of the C-O stretching vibration of OCS ($\approx 2062 \text{ cm}^{-1}$). The spectra are stacked in order of increasing values of an experimental parameter, backing pressure, which favors larger clusters. Some transitions are indicated with N , the number of ^4He atoms in the cluster.

$B_N = \hbar^2/2I_N$, *i.e.* an increased moment of inertia. In the specific case of a linear molecule embedded in ^4He , the energy expression takes the form

$$E_N(J) = B_N J(J+1) - D_N J^2(J+1)^2, \quad (1)$$

where J is the angular momentum and D_N is an effective centrifugal distortion constant, accounting for the non-rigidity of a molecule and partly for the residual effects of the environment. As an illustration, Fig. 1 shows the roto-vibrational spectra of small $\text{OCS}@^4\text{He}_N$ clusters, as reported in Ref. [6], corresponding to the transitions with $\Delta J = 1$ and involving $J = 0, 1$ and 2 rotational states. The most remarkable feature of the NCRI that is observed for certain molecules is a turnaround of the effective rotational constant B_N as a function of the cluster size N , that takes place well before the completion of the first solvation shell of ^4He atoms around a molecule. This was evidenced both experimentally and theoretically for OCS [6, 8, 9], carbon dioxide (CO_2) [10], nitrous oxide (N_2O) [11] and cyanoacetylene (HCCCN) [12]. The turnaround for some of these molecules is displayed in Fig. 2, which demonstrates a remarkable agreement between numerical simulations and experiments.

Thanks to the interplay between theory and experiment, all of the principal spectral features are now well understood. Much of this progress is

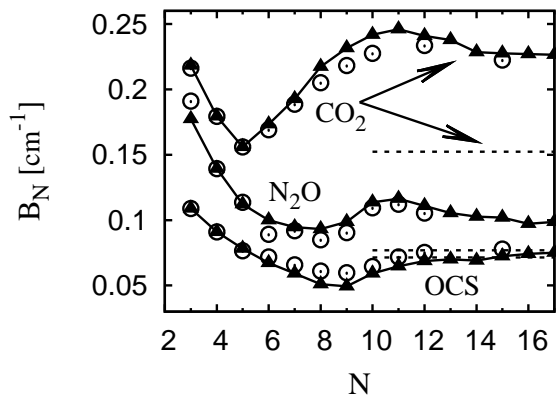


Figure 2: The cluster size evolution of the effective rotational constants B_N of CO_2 , N_2O and OCS molecules solvated in ^4He ; experimental data (open circles) and RQMC simulation data (filled triangles). The horizontal dashed lines correspond to their limiting values, *i.e.* B_∞ measured in ^4He nanodroplets.

due to recent advances in the quantum simulation methodology, particularly the development of the reptation quantum Monte Carlo (RQMC) technique [13, 14], that has allowed the study of doped ^4He clusters to be extended from the structure of the ground state to the dynamical regime, at least in the low-frequency portion of the spectrum. RQMC proved to be a powerful tool, yielding accurate rotational excitation energies (see Fig. 2). Even more importantly, RQMC provides much microscopic information not accessible to experiments, such as binding energies, ^4He density profiles and dynamical correlations between the solvated molecule and the ^4He solvent, thus helping unveil the relationship between structural and dynamical properties and the onset of superfluidity [8].

Despite the fact that the main characteristics of doped ^4He clusters spectra are now well understood (for a comprehensive overview see Refs. [15, 16, 17, 18]), a growing body of new and unexpectedly rich experimental information is becoming available in both small and medium-sized clusters, as well as in large ^4He nanodroplets. These studies display a wealth of subtle features that do not fit a free-rotor picture and still remain to be understood. They include such phenomena as line broadening and splitting and the detection of faint spectral lines. Further, RQMC simulations indicate that the

convergence of the size-dependent rotational constant B_N to the nanodroplet limit, B_∞ , is fast or slow for light and heavy molecules, respectively [19, 20]. This finding is in quantitative agreement with experimental data available for small to medium-sized clusters [10, 21, 22] and in qualitative agreement with the spectra of heavy OCS molecule in larger clusters containing up to $N \approx 100$ ^4He atoms [9]. However, the value of B_∞ for the light carbon monoxide (CO) molecule in ^4He nanodroplets, reported in Ref. [23], is significantly lower than the value inferred from the dynamics of the molecule in medium-sized clusters [24].

In this thesis we will address these open issues in the spectroscopy of doped ^4He clusters. Some of the techniques developed to this purpose will turn out to be instrumental in tackling one of the hardest problems in quantum simulation today, namely the simulation of interacting fermions. In particular, we will address the splitting of roto-vibrational lines observed in the spectra of small $\text{CO}@^4\text{He}_N$ clusters for some cluster sizes N [25], that led in turn to ambiguous assignments of experimental lines around this size range [26]. Then, we will investigate the nature of the weak satellite band, experimentally seen to accompany the roto-vibrational line in the infrared spectrum of CO_2 solvated in ^4He nanodroplets [27]. Further, the controversial convergence of CO effective rotational constant towards the nanodroplet limit will be discussed. Finally, we will study the effect that particle exchanges in a quantum solvent exhibit on the spectra of embedded molecules. This physical issue is particularly interesting because the NCRI manifests itself in quantum clusters already for extremely small system sizes. Experimentally, this effect was studied by Grebenev *et al.* [28, 29] by comparing the rotational spectra of OCS molecule solvated with para-hydrogen molecules, that are indistinguishable bosons, and ortho-deuterium molecules, an essentially distinguishable bosonic mixture. On the theoretical side, this issue was tackled by finite temperature simulations of N_2O solvated with distinguishable particles [11]. In this thesis we will address it by zero-temperature simulations of doped ^3He clusters.

The thesis is organized as follows. Quantum Monte Carlo methods are introduced in Chapter 1, with emphasis on RQMC. In Chapter 2 we present the implementation of RQMC for doped He clusters, together with several

technical details of the simulation. Chapter 3 addresses the approach of CO effective rotational constant to its nanodroplet value. In Chapter 4 we cope with fine spectral features such as line splittings in small $\text{CO}@^4\text{He}_N$ clusters and the satellite band in the infrared spectra of CO_2 solvated in ^4He nanodroplets. To this purpose, we introduce symmetry-adapted, imaginary-time correlation functions (SAITCFs), that are specifically devised for an explicit theoretical characterization of individual excitations, as well as for an enhanced computational efficiency in the calculation of weak spectral features. Also, we show how RQMC data help to discriminate between different assignments of experimental lines proposed for $\text{CO}@^4\text{He}_N$ clusters around the cluster size where one of the splittings is observed. In Chapter 5 we address the effect of particle statistics on the rotational spectra of ^3He -solvated molecules. We introduce a new method, based on a generalization of SAITCF approach that allows us to access rotational states of systems obeying Fermi statistics, still performing RQMC simulations for bosons. We apply this method to CO_2 solvated with ^3He atoms. Our preliminary results indicate that a certain amount of NCRI is found also in these fermionic clusters.

Chapter 1

Quantum Monte Carlo

Monte Carlo (MC) methods represent a wide class of computational techniques relying on sequences of (pseudo) random numbers, which aim at calculating multidimensional integrals involving a very large number of degrees of freedom. The statistical error of MC methods scales as the inverse of the square root of the number of samples, independent of the dimensionality of the integral. This scaling favors MC over deterministic computational schemes whenever the dimensionality becomes larger than $\sim 5 - 10$.

Quantum Monte Carlo (QMC) methods have the objective to accurately describe quantum systems. They are variational or projective in nature. Variational MC relies on the Ritz variational principle and it is an approximate method. Projection QMC algorithms are exact in principle, as they solve the Schrödinger equation. This is done by simulating a random walk that mimics a quantum evolution, so that a wave function is propagated starting from some suitable initial guess. The random walk asymptotically samples a probability distribution which is proportional (at least for bosons¹) to the ground state wave function [30, 31].

¹In this Chapter we are concerned with QMC methods that are tailored for bosons. A possible extension of the methods exposed here that allows one to access fermionic properties will be presented in Chapter 5.

1.1 The Metropolis algorithm

The expectation value of the physical observable $\hat{\mathcal{O}}$ (either quantum or classical) is given by

$$\langle \hat{\mathcal{O}} \rangle = \frac{\int d\mathbf{R} \mathcal{O}(\mathbf{R}) \pi(\mathbf{R})}{\int d\mathbf{R} \pi(\mathbf{R})}, \quad (1.1)$$

where \mathbf{R} is a $3N$ -dimensional vector, denoting the configuration of a system consisting of N particles and $\pi(\mathbf{R})$ is a positive function, proportional to an appropriate probability distribution.

The simple and powerful Metropolis rejection algorithm [32] defines a computationally convenient kinetics that asymptotically leads a *random walk* towards equilibrium where the desired probability $\pi(\mathbf{R})$ is sampled. A sufficient requirement for a random walk to reach equilibrium is the so-called *detailed balance* condition

$$T(\mathbf{R}', \mathbf{R}) \pi(\mathbf{R}) = T(\mathbf{R}, \mathbf{R}') \pi(\mathbf{R}'), \quad (1.2)$$

where $T(\mathbf{R}', \mathbf{R})$ is the transition probability of a (discrete-time) stochastic process. The Metropolis algorithm sets up a random walk generation as a two-step procedure: starting from some initial position \mathbf{R} , the trial position \mathbf{R}' is sampled, using some *a priori* transition probability $T^0(\mathbf{R}', \mathbf{R})$. This trial move is then accepted according to

$$a(\mathbf{R}', \mathbf{R}) = \min \left\{ 1, \frac{T^0(\mathbf{R}, \mathbf{R}') \pi(\mathbf{R}')}{T^0(\mathbf{R}', \mathbf{R}) \pi(\mathbf{R})} \right\}, \quad (1.3)$$

the so-called *Metropolis acceptance probability*. Such a rejection test modifies the transition probability of a random walk from the initial $T^0(\mathbf{R}', \mathbf{R})$ to the asymptotic $T(\mathbf{R}', \mathbf{R}) = T^0(\mathbf{R}', \mathbf{R}) a(\mathbf{R}', \mathbf{R})$, so that the detailed balance condition, Eq. (1.2), is satisfied. This allows a fairly wide choice for the transition probability $T^0(\mathbf{R}', \mathbf{R})$ to be employed, with ergodicity being the only requirement. Also, very conveniently, the algorithm does not depend on the explicit knowledge of the normalization of the sampled distribution, that is usually unknown.

1.2 Langevin dynamics

The approach of a random walk towards a system equilibrium can be described phenomenologically by the discretized (over-damped) Langevin equation [33]

$$\mathbf{R}' = \mathbf{R} + D\varepsilon\mathbf{F}(\mathbf{R}) + \xi, \quad (1.4)$$

where $\mathbf{F}(\mathbf{R}) = -\partial V(\mathbf{R})/\partial\mathbf{R}$ is the *drift force* that governs the classical diffusion in the external field $V(\mathbf{R})$, ε is the step of the time discretization, D is a diffusion constant and ξ 's are independent Gaussian random numbers of zero mean and variance $2D\varepsilon$.

The equilibrium probability distribution of the Langevin random walk is $\pi(\mathbf{R}) = e^{-V(\mathbf{R})}$. In the continuum limit, $\varepsilon \rightarrow 0$, Langevin dynamics satisfies the detailed balance condition in Eq. (1.2) exactly, while in the discrete case the Langevin transition probability

$$T(\mathbf{R}', \mathbf{R}) = \frac{1}{\sqrt{(4\pi D\varepsilon)^{3N}}} \exp \left\{ -\frac{[\mathbf{R}' - \mathbf{R} - D\varepsilon\mathbf{F}(\mathbf{R})]^2}{4D\varepsilon} \right\}, \quad (1.5)$$

satisfies the detailed balance approximatively, as:

$$T(\mathbf{R}', \mathbf{R}) e^{-V(\mathbf{R})} = T(\mathbf{R}, \mathbf{R}') e^{-V(\mathbf{R}')} + o(\varepsilon^{3/2}). \quad (1.6)$$

The Langevin random walk asymptotically samples the unique stationary solution of the so-called Fokker-Planck equation [33]

$$\frac{\partial P(\mathbf{R}, \tau)}{\partial \tau} = \widehat{\mathcal{F}}P(\mathbf{R}, \tau), \quad (1.7)$$

that governs the time-evolution of the probability $P(\mathbf{R}, \tau)$ to find a classical particle, undergoing a thermal motion in the field $V(\mathbf{R})$ of an external force, in the position \mathbf{R} at the time τ ; and $\widehat{\mathcal{F}}$ is the so-called Fokker-Planck operator:

$$\widehat{\mathcal{F}} = D \frac{\partial^2}{\partial \mathbf{R}^2}(\cdot) - D \frac{\partial}{\partial \mathbf{R}} \frac{\partial V(\mathbf{R})}{\partial \mathbf{R}}(\cdot). \quad (1.8)$$

The unique stationary solution of Eq. (1.7), sampled by Langevin dynamics, is $P_s(\mathbf{R}) = \lim_{\tau \rightarrow \infty} P(\mathbf{R}, \tau) = e^{-V(\mathbf{R})}$.

The Fokker-Planck equation is quite similar to the Schrödinger equation in imaginary time, apart from the presence of a term proportional to

$\frac{\partial V(\mathbf{R})}{\partial \mathbf{R}} \frac{\partial P(\mathbf{R}, \tau)}{\partial \mathbf{R}}$. However, this term can be eliminated by introducing the transformation [34]

$$P(\mathbf{R}, \tau) = \psi(\mathbf{R}, \tau)\psi_T(\mathbf{R}) \quad \text{with} \quad \psi_T(\mathbf{R}) \propto e^{-V(\mathbf{R})/2}, \quad (1.9)$$

so that the formal analogy between the classical diffusion and the quantum imaginary-time Schrödinger equation is found

$$\frac{\partial P(\mathbf{R}, \tau)}{\partial \tau} = \widehat{\mathcal{F}}P(\mathbf{R}, \tau) \iff \frac{\partial \psi(\mathbf{R}, \tau)}{\partial \tau} = \widehat{\mathcal{H}}\psi(\mathbf{R}, \tau), \quad (1.10)$$

where

$$\widehat{\mathcal{H}} = -D \frac{\partial^2}{\partial \mathbf{R}^2} + D \frac{1}{\psi_T(\mathbf{R})} \frac{\partial^2 \psi_T(\mathbf{R})}{\partial \mathbf{R}^2} \quad (1.11)$$

is the Hamiltonian of some fictitious quantum system. By inspection, one could verify that $|\psi_T\rangle$ is the ground state of $\widehat{\mathcal{H}}$ with the zero eigenvalue, *i.e.* $\widehat{\mathcal{H}}|\psi_T\rangle = 0$.

The classical-quantum analogy established in this way allows us to interpret the Langevin drift force $\mathbf{F}(\mathbf{R}) = -\partial V(\mathbf{R})/\partial \mathbf{R}$ in Eq. (1.4), that governs the classical diffusion—by substituting $V(\mathbf{R}) = -2 \log \psi_T(\mathbf{R})$, in accordance with Eq. (1.9)—as the *quantum force* $F(\mathbf{R}) = 2\nabla_{\mathbf{R}}(\log \psi_T(\mathbf{R}))$ that governs the quantum evolution in imaginary time.

1.3 Variational Monte Carlo

The practical application of the Ritz variational principle in quantum mechanics requires our ability to compute the expectation value of the Hamiltonian operator over a *trial function* of a given functional form, and possibly depending on some set of control parameters α , $\psi_T(\alpha, \mathbf{R})$, where \mathbf{R} is a $3N$ -dimensional vector, representing the configuration of a system. Variational Monte Carlo (VMC) is the method that calculates the multidimensional integrals of the type given by Eq. (1.1), by realizing a stochastic sampling of the probability distribution $\pi(\mathbf{R}) = \psi_T^2(\alpha, \mathbf{R})$. The VMC energy estimate

$$E_{\text{VMC}}(\alpha) = \frac{\langle \psi_T(\alpha) | \widehat{H} | \psi_T(\alpha) \rangle}{\langle \psi_T(\alpha) | \psi_T(\alpha) \rangle} = \frac{\int d\mathbf{R} E_L(\alpha, \mathbf{R}) \psi_T^2(\alpha, \mathbf{R})}{\int d\mathbf{R} \psi_T^2(\alpha, \mathbf{R})} \geq E_0 \quad (1.12)$$

is the expectation value of the so-called *local energy*:

$$E_L(\alpha, \mathbf{R}) = \frac{\hat{H}\psi_T(\alpha, \mathbf{R})}{\psi_T(\alpha, \mathbf{R})}. \quad (1.13)$$

VMC is an approximate method whose accuracy depends entirely on the quality of a trial wave function. In our calculations we use VMC to optimize the trial wave function for the system of a doped He cluster. We perform the stochastic sampling of the probability $\pi(\mathbf{R}) = \psi_T^2(\alpha, \mathbf{R})$, by employing the discrete Langevin dynamics, Eq. (1.4). Then, we minimize the VMC energy in Eq. (1.12) with respect to the set of variational parameters α . Although our calculations do not suffer from the bias caused by the approximate nature of a trial wave function (see Sec. 1.5), an optimized input provided by VMC speeds up the convergence of our results to their exact values. The actual form of the trial function we employ is given in Sec. 2.1.

1.3.1 Wave function optimization

In order to determine the optimal trial wave function $\psi_T(\alpha_{opt}, \mathbf{R})$ by minimizing the VMC energy, we adopt the so-called *correlated sampling* approach [30]. This approach allows one to calculate expectation values of physical quantities over different probability distributions (see Eq. (1.1)), using the same underlying random walk. Suppose that the set of N configurations is sampled from the probability distribution $\psi_T^2(\alpha, \mathbf{R})$. Then, one estimates the VMC energy for a different trial function $\psi_T(\tilde{\alpha}, \mathbf{R})$ as the weighted average

$$E_{\text{VMC}}(\tilde{\alpha}) = \frac{\int d\mathbf{R} \psi_T^2(\alpha, \mathbf{R}) w(\tilde{\alpha}, \mathbf{R}) E_L(\tilde{\alpha}, \mathbf{R})}{\int d\mathbf{R} \psi_T^2(\alpha, \mathbf{R}) w(\tilde{\alpha}, \mathbf{R})} \approx \frac{\sum_{i=1}^N E_L(\tilde{\alpha}, \mathbf{R}_i) w(\tilde{\alpha}, \mathbf{R}_i)}{\sum_{i=1}^N w(\tilde{\alpha}, \mathbf{R}_i)}, \quad (1.14)$$

with weights $w(\tilde{\alpha}, \mathbf{R}) = \psi_T^2(\tilde{\alpha}, \mathbf{R})/\psi_T^2(\alpha, \mathbf{R})$. An immediate advantage of this approach is that in principle no further sampling is required, since the whole parameter space can be probed at once. A further advantage is that the correlation of the energies $E_{\text{VMC}}(\alpha)$ and $E_{\text{VMC}}(\tilde{\alpha})$ reduces the statistical error on their difference and makes it much easier to find a minimum. In order for the procedure to be reliable it is important that the weights $w(\tilde{\alpha}, \mathbf{R})$ in Eq. (1.14) are of the same order of magnitude, otherwise only few configurations with large weight will dominate in the sum, so that the energy estimate

can not be trusted. This happens when $N_{eff} = (\sum_{i=1}^N w_i)^2 / \sum_{i=1}^N w_i^2$, the number of configurations that effectively contribute to the weighted average, becomes much smaller than the total number of configurations N . This occurs when the attempted change $\alpha \rightarrow \tilde{\alpha}$ is taken too large, so that the weights become too scattered, indicating that the overlap between the two trial functions $\psi_T(\alpha, \mathbf{R})$ and $\psi_T(\tilde{\alpha}, \mathbf{R})$ is not sufficient. This makes the process of trial function optimization iterative: before N_{eff} becomes too small, a new set of configurations has to be generated using the current set of parameters $\tilde{\alpha}$, so that the search for the lower variational energy can be carried on. After the energy convergence within some predefined statistical error is achieved, the optimal set of variational parameters α_{opt} is identified.

Our trial wave function contains few tens of variational parameters and its optimization would be intractable without this sampling scheme. In practice, correlated sampling approach becomes particularly useful whenever there are more than a few parameters to be optimized.

1.4 Diffusion Monte Carlo

Diffusion Monte Carlo (DMC) is the most widely used QMC projection method [35] suited for continuous quantum systems [36], as well as for lattice models [37]. One starts from the Schrödinger equation in imaginary time

$$-\frac{\partial \psi(\mathbf{R}, \tau)}{\partial \tau} = -D\nabla_{\mathbf{R}}^2 \psi(\mathbf{R}, \tau) + (V(\mathbf{R}) - E_R)\psi(\mathbf{R}, \tau), \quad (1.15)$$

where E_R is the so-called *reference energy* [36]. Formally, by expanding the wave function $\psi(\mathbf{R}, \tau)$ as $\psi(\mathbf{R}, \tau) = \sum_n c_n e^{-(E_n - E_R)\tau} \Psi_n(\mathbf{R})$, where $\Psi_n(\mathbf{R})$ are Hamiltonian eigenfunctions and $c_n = \langle \psi(0) | \Psi_n \rangle$, one sees that for sufficiently long imaginary times τ the solution is proportional to the Hamiltonian ground state

$$\psi(\mathbf{R}, \tau) \propto e^{-(E_0 - E_R)\tau} \Psi_0(\mathbf{R}), \quad (1.16)$$

provided that the initial guess $\psi(\mathbf{R}, 0) = \psi_T(\mathbf{R})$ is non-orthogonal to the ground state, *i.e.* $\langle \psi_T | \Psi_0 \rangle \neq 0$. The first term in the right-hand side of Eq. (1.15) describes a diffusion process, while the second term represents a birth/death process. Since for bosons $\psi(\mathbf{R}, \tau)$ is non-negative, it can be

interpreted as the probability density of a suitable random walk that mimics simultaneous diffusion and birth/death processes.

The presence of the singularities in the potential energy $V(\mathbf{R})$ in Eq. (1.15), makes the simulation of the birth/death process exponentially unstable and the solution of the Schrödinger equation in the form of Eq. (1.15) impractical. Thus one introduces the function $f(\mathbf{R}, \tau) = \psi(\mathbf{R}, \tau)\psi_T(\mathbf{R})$, in terms of which Eq. (1.15) becomes:

$$\frac{\partial f(\mathbf{R}, \tau)}{\partial \tau} = D\nabla_{\mathbf{R}}^2 f(\mathbf{R}, \tau) - D\nabla_{\mathbf{R}} \left(f(\mathbf{R}, \tau) \mathbf{F}(\mathbf{R}) \right) + (E_R - E_L(\mathbf{R}))f(\mathbf{R}, \tau), \quad (1.17)$$

where the quantum force $\mathbf{F}(\mathbf{R}) = 2\nabla_{\mathbf{R}}(\log \psi_T(\mathbf{R}))$ now guides the so-called *drift-diffusion* process (the first two terms in the right-hand side of Eq. (1.17)), while the birth/death part depends on the local energy, Eq. (1.13), instead of the potential energy. For a good trial function this leads to a substantially smoother birth/death process. The asymptotic solution for $f(\mathbf{R}, \tau)$ is the so-called “mixed” distribution

$$f(\mathbf{R}, \tau \rightarrow \infty) = \Psi_0(\mathbf{R})\psi_T(\mathbf{R}), \quad (1.18)$$

that has the same functional form as the solution of the Fokker-Planck equation, Eq. (1.9). Also, we note that in the continuous limit, $\varepsilon \rightarrow 0$, the drift-diffusion term alone would drive the random walk to the VMC distribution $\psi_T^2(\mathbf{R})$ (see Sec. 1.3), so that the effect of the birth/death process is to correct it for the amount $\Psi_0(\mathbf{R})/\psi_T(\mathbf{R})$.

In the short-time limit the drift-diffusion part of the transition probability has the form

$$G_d(\mathbf{R}', \mathbf{R}, \varepsilon) = \frac{1}{\sqrt{(4\pi D\varepsilon)^{3N}}} \exp \left\{ - \left[\frac{(\mathbf{R}' - \mathbf{R} - D\varepsilon \mathbf{F}(\mathbf{R}))^2}{4D\varepsilon} \right] \right\}, \quad (1.19)$$

while the so-called *branching* term, that appears as a weight in the random walk, is given by:

$$G_b(\mathbf{R}', \mathbf{R}, \varepsilon) = \exp \left\{ - \left[\frac{1}{2} (E_L(\mathbf{R}') + E_L(\mathbf{R})) - E_R \right] \varepsilon \right\}. \quad (1.20)$$

Instead accumulating weights, a more favorable alternative is to create identical copies or delete a single configuration, in the spirit of the branching

process. These copies are then independently diffused, and after some time they eventually decorrelate. This forms the so-called *walker population*.

Although DMC provides an exact value (within statistical error) for the ground state energy E_0 , it gives the *mixed estimators* $\langle \mathcal{O} \rangle_{mix} = \langle \psi_T | \hat{\mathcal{O}} | \Psi_0 \rangle$ for the quantities that do not commute with Hamiltonian. Implementation of the so-called *forward walk* [38] can in principle remove this bias, however at the price of additional fluctuations. The other systematic error present in DMC is the so-called *population control* bias, that originates from the need to provide stable asymptotic population, by adjusting the E_R value in Eq. (1.17) during the simulation. Both systematic biases present in DMC, the mixed-distribution and the population control, along with the apparent absence of completely satisfactory way to cure them out are the consequence of the lack of the integrability of the branching term in Eq. (1.20), and thus inherent of DMC. All these sources of systematic bias can be removed by incorporating the branching term into the Metropolis acceptance probability of an appropriate random walk, as it is done in RQMC method, that we introduce in the next Section.

1.5 Reptation quantum Monte Carlo

RQMC is an alternative projection quantum Monte Carlo method [13, 14], that allows for the exact calculation of the ground state properties for bosonic many-body systems. RQMC exploits the analogy between the classical diffusion and the imaginary-time quantum evolution, but in contrast with DMC, it does not suffer from mixed-distribution nor population-control biases. Moreover, it is ideally suited to exploit imaginary-time dynamics, thus offering the possibility to explore excited states, the topic of high interest.

1.5.1 The original formulation

The quantum-classical analogy we have discussed in Sec. 1.2 (in particular, see Eq. (1.10)), implies that time correlations, that are of a central impor-

tance in this thesis, can be expressed in two “languages”²

$$\begin{aligned} \langle \mathcal{O}(\tau)\mathcal{O}(0) \rangle &= \iint d\mathbf{R}' d\mathbf{R} \mathcal{O}(\mathbf{R}') \mathcal{W}(\mathbf{R}', \mathbf{R}, \tau) \psi_T^2(\mathbf{R}) \mathcal{O}(\mathbf{R}) \\ &\iff (1.21) \\ \langle \psi_T | \hat{\mathcal{O}}(\tau) \hat{\mathcal{O}}(0) | \psi_T \rangle &= \iint d\mathbf{R}' d\mathbf{R} \psi_T(\mathbf{R}') \mathcal{O}(\mathbf{R}') \mathcal{G}(\mathbf{R}', \mathbf{R}, \tau) \mathcal{O}(\mathbf{R}) \psi_T(\mathbf{R}) \end{aligned}$$

where $\hat{\mathcal{O}}$ is a physical observable, $\mathcal{W}(\mathbf{R}', \mathbf{R}, \tau)$ is the Green function of the Fokker-Plank equation and $\mathcal{G}(\mathbf{R}', \mathbf{R}, \tau) = \langle \mathbf{R}' | e^{-\tau \hat{\mathcal{H}}} | \mathbf{R} \rangle$ is the quantum propagator of the fictitious quantum system with Hamiltonian $\hat{\mathcal{H}}$, given by Eq. (1.11). From Eq. (1.21) we see that $\mathcal{W}(\mathbf{R}', \mathbf{R}, \tau)$, defined as the transition probability of the classical random walk, equals the so-called *importance-sampled quantum propagator* $\tilde{\mathcal{G}}$ of the fictitious quantum system:

$$\mathcal{W}(\mathbf{R}', \mathbf{R}, \tau) = \psi_T(\mathbf{R}') \mathcal{G}(\mathbf{R}', \mathbf{R}, \tau) \frac{1}{\psi_T(\mathbf{R})} \equiv \tilde{\mathcal{G}}. \quad (1.22)$$

In the short-time approximation, $\mathcal{W}(\mathbf{R}', \mathbf{R}, \tau)$ has the form of the Langevin transition probability in Eq. (1.5):

$$\mathcal{W}_\varepsilon(\mathbf{R}', \mathbf{R}) = \frac{1}{\sqrt{(4\pi D\varepsilon)^{3N}}} \exp \left\{ - \left(\frac{(\mathbf{R}' - \mathbf{R} - D\varepsilon \mathbf{F}(\mathbf{R}))^2}{4D\varepsilon} \right) \right\}. \quad (1.23)$$

We note that Eq. (1.23) justifies the choice for the transition probability we employ in VMC; also, it corresponds to the drift-diffusion term in DMC, Eq. (1.19).

We introduce the random walk $X = \{\mathbf{R}_0, \mathbf{R}_1, \dots, \mathbf{R}_p\}$, where \mathbf{R}_k is the system configuration at the time $\tau_k = k\varepsilon$, the so-called *time-slice*. The path probability, *i.e.* the probability of a given sequence of configurations in the path X is:

$$\begin{aligned} \mathcal{P}[X] &= \mathcal{W}_\varepsilon(\mathbf{R}_p, \mathbf{R}_{p-1}) \cdots \mathcal{W}_\varepsilon(\mathbf{R}_1, \mathbf{R}_0) \psi_T^2(\mathbf{R}_0) \text{ or} \\ &= \psi_T(\mathbf{R}_p) \mathcal{G}(\mathbf{R}_p, \mathbf{R}_{p-1}, \varepsilon) \cdots \mathcal{G}(\mathbf{R}_1, \mathbf{R}_0, \varepsilon) \psi_T(\mathbf{R}_0). \end{aligned} \quad (1.24)$$

We need the path probability $P[X]$ for the true Hamiltonian \hat{H} , while the one in Eq. (1.24) is the path probability for the fictitious Hamiltonian $\hat{\mathcal{H}}$. Since

²Note that in the quantum case τ has the meaning of imaginary time, *i.e.* $\tau = -it$.

$E_L(\mathbf{R}) = \hat{H}\psi_T(\mathbf{R})/\psi_T(\mathbf{R})$ (see Eq. (1.12)) and $\hat{\mathcal{H}}\psi_T(\mathbf{R}) = 0$ (see Sec. 1.2), the two Hamiltonians are related as $\hat{H} = \hat{\mathcal{H}} + E_L(\mathbf{R})$. By employing the Trotter formula [39], we find the relation between the true and fictitious quantum propagators in the short-time approximation

$$G(\mathbf{R}', \mathbf{R}, \varepsilon) = e^{-\frac{\varepsilon}{2}E_L(\mathbf{R}')} \mathcal{G}(\mathbf{R}', \mathbf{R}, \varepsilon) e^{-\frac{\varepsilon}{2}E_L(\mathbf{R})}, \quad (1.25)$$

and finally, the probability of the true quantum path

$$P[X] = \mathcal{P}[X] e^{-S[X]}, \quad (1.26)$$

where $S[X]$ is the time-discretized integral of the local energy along the path, *i.e.* $S[X] = \varepsilon [E_L(\mathbf{R}_0)/2 + E_L(\mathbf{R}_1) + \dots + E_L(\mathbf{R}_{p-1}) + E_L(\mathbf{R}_p)/2]$.

Using Eqs. (1.24) and (1.26) we arrive at the following expression for the path probability of the true quantum system:

$$P[X] = \frac{\psi_T^2(\mathbf{R}_0) \prod_{i=1}^{2p} \mathcal{W}_\varepsilon(\mathbf{R}_{i+1}, \mathbf{R}_i) e^{-\frac{\varepsilon}{2} [E_L(\mathbf{R}_{i+1}) + E_L(\mathbf{R}_i)]}}{\int d\mathbf{R}'_0 \dots d\mathbf{R}'_{2p+1} \psi_T^2(\mathbf{R}'_0) \prod_{i=1}^{2p} \mathcal{W}_\varepsilon(\mathbf{R}'_{i+1}, \mathbf{R}'_i) e^{-\frac{\varepsilon}{2} [E_L(\mathbf{R}'_{i+1}) + E_L(\mathbf{R}'_i)]}}. \quad (1.27)$$

Dynamical variables in RQMC are quantum paths or *snakes*. A reptation move $X \rightarrow Y$ is accomplished by cutting the configuration \mathbf{R}_0 from the tail of the snake $X = \{\mathbf{R}_0, \mathbf{R}_1 \dots \mathbf{R}_{p-1}, \mathbf{R}_p\}$ and sticking the new configuration \mathbf{R}_{p+1} on its head, keeping the number of time-slices in the path constant. The transition probability $\mathcal{W}_\varepsilon(\mathbf{R}_{p+1}, \mathbf{R}_p)$ employed to sample \mathbf{R}_{p+1} , Eq. (1.23), corresponds to a step in Langevin dynamics, Eq. (1.4). The new path thus generated is $Y = \{\mathbf{R}_1, \mathbf{R}_2 \dots \mathbf{R}_p, \mathbf{R}_{p+1}\}$. The schematic representation of this, the so-called *reptation* or *slithering snake* move is illustrated in Fig. 1.1.

Using the Metropolis formula, Eq. (1.3) and Eqs. (1.23) and (1.27), one finds the acceptance probability of the reptation algorithm [14]

$$a(Y \leftarrow X) = \min \left\{ 1, \frac{\exp \left(-\frac{\varepsilon}{2} [E_L(\mathbf{R}_{p+1}) + E_L(\mathbf{R}_p)] \right)}{\exp \left(-\frac{\varepsilon}{2} [E_L(\mathbf{R}_1) + E_L(\mathbf{R}_0)] \right)} \times \mathcal{Q}(\varepsilon) \right\}, \quad (1.28)$$

with the dominant part depending on the appropriate local energies. The rest of the expression, denoted with $\mathcal{Q}(\varepsilon)$, converges faster to 1 in the zero-time limit $\varepsilon \rightarrow 0$. Finally, we note the way the branching term, Eq. (1.20), is handled in RQMC: it is incorporated in the acceptance probability of the Metropolis random walk, in contrast with the DMC where it appeared as a weight in a branching random walk.

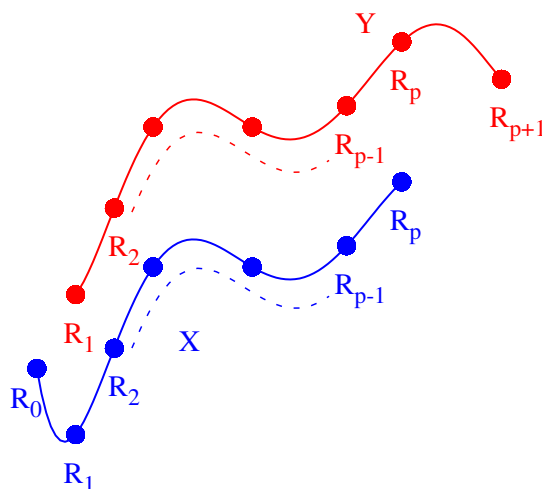


Figure 1.1: Schematic representation of the reptation move: the old path or snake, X, is displayed in the blue solid line, while the red solid line represents the new path Y.

1.5.2 Excited states

We have anticipated in Eq. (1.21), that the quantum expectation value of the autocorrelation function in imaginary time $\tau = -it$ of an observable \hat{O} , $\mathcal{C}_{\hat{O}}(\tau)$, over the ground state of the fictitious Hamiltonian, $|\psi_T\rangle$, maps onto the value calculated along the random walk. In order to compute expectation values over the ground state $|\Psi_0\rangle$ of the true quantum system, one needs to average over the random walk that is re-weighted by the exponential of the action (see Eq. (1.27))

$$\mathcal{C}_{\hat{O}}(\tau) = \langle \Psi_0 | \hat{O}(\tau) \hat{O}(0) | \Psi_0 \rangle = \langle\langle \hat{O}(\tau) \hat{O}(0) \rangle\rangle_{\text{RW}}, \quad (1.29)$$

where the symbol $\langle\langle \cdot \rangle\rangle_{\text{RW}}$ indicates an average over the distribution of quantum paths given by Eq. (1.27).

Employing the imaginary-time Heisenberg picture for quantum operators, $\hat{O}(\tau) = e^{\tau \hat{H}} \hat{O} e^{-\tau \hat{H}}$, one has

$$\mathcal{C}_{\hat{O}}(\tau) = \sum_{n \neq 0} |\langle \Psi_0 | \hat{O} | \Psi_n \rangle|^2 e^{-(E_n - E_0)\tau}, \quad (1.30)$$

where $|\Psi_n\rangle$'s are eigenstates of the Hamiltonian \hat{H} . In this way the dynamical properties of the RQMC random walk allow the analysis of the excitation spectrum of a quantum system.

Eq. (1.30) indicates that only those excited states that have a non-vanishing matrix element with the ground state, *i.e.* $|\langle \Psi_0 | \hat{\mathcal{O}} | \Psi_n \rangle| \neq 0$, contribute to the imaginary-time correlation function (CF) $\mathcal{C}_{\hat{\mathcal{O}}}(\tau)$. Let us suppose, for example, that the system under investigation is rotationally invariant and that its ground state has zero angular momentum, *i.e.* $J'' = 0$. Then the following selection rule holds:

$$\langle J' M' | \hat{\mathcal{O}}_{JM} | J'' = 0 \rangle = 0 \text{ if } J' \neq J \text{ and } M' \neq M. \quad (1.31)$$

We see that the operator $\hat{\mathcal{O}}$, out of all possible system excitations, effectively filters out the states having the particular JM symmetry.

Chapter 2

Implementation: doped He clusters

In this Chapter we introduce the model Hamiltonian, the trial wave function and the present implementation of RQMC algorithm employed to study various models of doped He clusters. Further, practical details such as the extraction of rotational energies from the imaginary-time CFs are discussed. Finally, various convergence issues are illustrated, showing how various physical quantities depend on the parameters of the simulation.

2.1 The model system

The system consists of a linear molecule X embedded in a cluster of N He atoms. We employ a realistic model Hamiltonian in which He atoms are treated as point-like particles and the molecule X as a rigid linear rotor:

$$\hat{H} = -\frac{\hbar^2}{2m_X} \hat{\mathbf{p}}_{\mathbf{X}}^2 - \frac{\hbar^2}{2I_X} \hat{\mathbf{L}}_{\mathbf{X}}^2 - \frac{\hbar^2}{2m} \sum_{i=1}^N \hat{\mathbf{p}}_i + \sum_{i<j}^N V_{He-He}(r_{ij}) + \sum_{i=1}^N V_{X-He}(r_i, \theta_i), \quad (2.1)$$

where m_X , I_X , $\hat{\mathbf{p}}_{\mathbf{X}}$, and $\hat{\mathbf{L}}_X$ are the mass, moment of inertia, linear and angular momentum of the molecule, respectively, while m and $\hat{\mathbf{p}}_i$ are the mass and linear momenta of He atoms; r_{ij} is the relative distance between the i -th and j -th He atom, while (r_i, θ_i) characterizes X-He relative position (see Fig. 2.1). The interparticle interactions are described by pair potentials

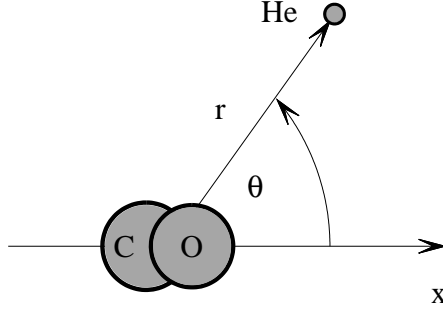


Figure 2.1: Schematic representation of the polar coordinates r and θ , used in the expression for the He-molecule potential; x coincides with the molecular symmetry axis.

and are obtained from *ab initio* quantum chemistry calculations. Particularly, for a $V_{He-He}(r_{ij})$ we adopt the SAPT2 potential of Ref. [40], while for $V_{X-He}(r_i, \theta_i)$ we employ appropriate two-dimensional parametrization of X-He potential averaged over the vibrational ground state.

The functional form of the trial function ψ_T is chosen to be of the Jastrow type:

$$\psi_T = \exp \left\{ - \sum_{i=1}^N \mathcal{U}_1(r_i, \theta_i) - \sum_{i<j}^N \mathcal{U}_2(r_{ij}) \right\}, \quad (2.2)$$

where $\mathcal{U}_1(r_i, \theta_i)$ and $\mathcal{U}_2(r_{ij})$ are the so-called X-He and He-He *pseudopotentials*. In order to describe anisotropic correlations between He atoms and the molecule, the pseudopotential \mathcal{U}_1 is assumed to be a sum of Legendre polynomials times radial functions, such as:

$$\mathcal{U}_1(r, \theta) = \sum_{\ell=1}^{\ell_{max}} R_{\ell}(r) P_{\ell}(\cos \theta). \quad (2.3)$$

Keeping terms up to $\ell_{max} = 5 \div 6$ is enough to represent the anisotropic components of all the X-He correlations in systems considered in this thesis. For the radial functions $R_{\ell}(r)$ we use the parametrization [41]

$$R_{\ell}(r) = \left(\ln 2 \left(\frac{p_1}{r} \right)^5 p_2 r^{p_3} - p_4 \ln r \right), \quad (2.4)$$

while for the pseudopotential $\mathcal{U}_2(r_{ij})$ we adopt the functional form

$$\mathcal{U}_2(r) = \frac{p_5}{r^{p_6}} + p_7 e^{-p_8(r-p_9)^2}, \quad (2.5)$$

used in Ref. [42] for the variational description of bulk ${}^4\text{He}$.

2.2 Algorithm

The availability of a good trial function leads to a smoother local energy and in the ideal limit, when $\psi_T \rightarrow \Psi_0$, the acceptance probability of RQMC move, Eq. (1.28), becomes equal to 1. In practice, however, one has to estimate the net gain between the computational efficiency and the simple implementation. In the present implementation of the RQMC algorithm, we employ the so-called *primitive approximation* for the quantum propagator:

$$G_p(\mathbf{R}', \mathbf{R}, \varepsilon) = \frac{1}{\sqrt{(4\pi D\varepsilon)^{3N}}} \exp\left\{-\frac{(\mathbf{R}' - \mathbf{R})^2}{4D\varepsilon}\right\} \exp\left\{-\frac{\varepsilon}{2}[V(\mathbf{R}) + V(\mathbf{R}')]\right\}. \quad (2.6)$$

With this choice, the implementation is fairly simple, while the loss of efficiency is not very significant. This is the case because the quality of the trial wave functions available for He systems (even for the benchmark system of bulk liquid ^4He) is not good enough¹ to exploit the advantages of the original RQMC algorithm.

By employing Eq. (2.6) the probability density of the quantum path, Eq. (1.27), becomes:

$$\pi[X] = \frac{\psi_T(\mathbf{R}_0) \prod_{i=1}^{2p} G_p(\mathbf{R}_{i+1}, \mathbf{R}_i, \varepsilon) \psi_T(\mathbf{R}_{2p+1})}{\int d\mathbf{R}'_0 \cdots d\mathbf{R}'_{2p+1} \psi_T(\mathbf{R}'_0) \prod_{i=1}^{2p} G_p(\mathbf{R}'_{i+1}, \mathbf{R}'_i, \varepsilon) \psi_T(\mathbf{R}'_{2p+1})}. \quad (2.7)$$

Using Eq. (2.7), the Metropolis acceptance probability, Eq. (1.28), has a slightly different form with respect to the one in the original formulation:

$$a(Y \leftarrow X) = \min \left\{ 1, \frac{\mathcal{W}_\varepsilon(\mathbf{R}_0, \mathbf{R}_1) \exp\left(-\frac{\varepsilon}{2}[V(\mathbf{R}_{p+1}) + V(\mathbf{R}_p)]\right) \psi_T(\mathbf{R}_1) \psi_T(\mathbf{R}_{p+1})}{\mathcal{W}_\varepsilon(\mathbf{R}_{p+1}, \mathbf{R}_p) \exp\left(-\frac{\varepsilon}{2}[V(\mathbf{R}_1) + V(\mathbf{R}_0)]\right) \psi_T(\mathbf{R}_0) \psi_T(\mathbf{R}_p)} \right\}. \quad (2.8)$$

We employ one variant of the reptation move, the so-called *bounce algorithm*: if the move $X \rightarrow Y$, *i.e.* $\mathbf{R}_p \rightarrow \mathbf{R}_{p+1}$ is accepted, the next attempted move is undertaken in the same direction. Otherwise, the direction of the reptation attempt is reversed. The bounce algorithm does not satisfy the

¹As an illustration, see VMC *vs* exact ^4He radial density profile in $\text{CO}@^4\text{He}_{200}$ cluster in Sec. 3.2.

detailed balance condition (Eq. (1.2)), but nevertheless it does sample the correct path probability $\pi[X]$ in Eq. (2.7), as shown in Ref. [43]. The auto-correlation time of this algorithm, that is the number of MC steps needed to refresh all the slices, is $p^2/(ab)$, where p is the length of the snake, a is the acceptance probability and b is the average number of steps realized in the same direction before the bounce occurred.

RQMC systematically improves the VMC trial wave function, so that the ground state wave function is approached as

$$|\psi_\beta\rangle = e^{-\beta\hat{H}}|\psi_T\rangle \propto |\Psi_0\rangle, \quad (2.9)$$

provided that the *projection time* β is sufficiently large. The ground-state expectation value of the observable $\hat{\mathcal{O}}$ is found as

$$\langle\hat{\mathcal{O}}\rangle_\beta = \frac{\langle\psi_T e^{-\beta\hat{H}}|\hat{\mathcal{O}}|e^{-\beta\hat{H}}\psi_T\rangle}{\langle\psi_T|e^{-2\beta\hat{H}}|\psi_T\rangle} = \frac{\int dX \mathcal{O}[X]\pi[X]}{\int dX \pi[X]}, \quad (2.10)$$

or, more explicitly,

$$\langle\hat{\mathcal{O}}\rangle_\beta = \frac{\int d\mathbf{R}_0\dots d\mathbf{R}_{2p+1}\psi_T(\mathbf{R}_0)\prod_{i=1}^{2p}G_p(\mathbf{R}_{i+1},\mathbf{R}_i,\varepsilon)\psi_T(\mathbf{R}_{2p+1})\mathcal{O}(\mathbf{R}_{p+1})}{\int d\mathbf{R}_0\dots d\mathbf{R}_{2p+1}\psi_T(\mathbf{R}_0)\prod_{i=1}^{2p}G_p(\mathbf{R}_{i+1},\mathbf{R}_i,\varepsilon)\psi_T(\mathbf{R}_{2p+1})}, \quad (2.11)$$

where the total imaginary-time length 2β is discretized in $(2p+1)$ time steps ε , and \mathbf{R}_{p+1} is the middle slice configuration of the path, where the value of the local operator $\hat{\mathcal{O}}$ is calculated. Similarly, the imaginary-time correlations of the operators $\hat{\mathcal{A}}$ and $\hat{\mathcal{B}}$ are calculated as

$$\langle\hat{\mathcal{C}}_{\hat{\mathcal{A}},\hat{\mathcal{B}}}(\tau)\rangle_\beta = \langle\hat{\mathcal{A}}(0)\hat{\mathcal{B}}(\tau)\rangle_\beta = \frac{\langle\psi_T e^{-\beta\hat{H}}|\hat{\mathcal{A}}e^{-\tau\hat{H}}\hat{\mathcal{B}}|e^{-\beta\hat{H}}\psi_T\rangle}{\langle\psi_T|e^{-(2\beta+\tau)\hat{H}}|\psi_T\rangle} \quad (2.12)$$

or, in the explicit form:

$$\begin{aligned} \langle\hat{\mathcal{C}}_{\hat{\mathcal{A}},\hat{\mathcal{B}}}(\tau)\rangle_\beta &= \\ &= \frac{\int d\mathbf{R}_0\dots d\mathbf{R}_{2p+1}\psi_T(\mathbf{R}_0)\prod_{i=1}^{2p}G_p(\mathbf{R}_{i+1},\mathbf{R}_i,\varepsilon)\psi_T(\mathbf{R}_{2p+1})\mathcal{A}(\mathbf{R}_{p+1})\mathcal{B}(\mathbf{R}_{p+q+1})}{\int d\mathbf{R}_0\dots d\mathbf{R}_{2p+1}\psi_T(\mathbf{R}_0)\prod_{i=1}^{2p}G_p(\mathbf{R}_{i+1},\mathbf{R}_i,\varepsilon)\psi_T(\mathbf{R}_{2p+1})}. \end{aligned} \quad (2.13)$$

The path now consists of a larger number of time-slices, such that $(2p+1) = (2\beta+\tau)/\varepsilon$ and $q = \tau/\varepsilon$, so that the values of the operators could be calculated at two time slices \mathbf{R}_{p+1} and \mathbf{R}_{p+q+1} , separated by the imaginary time τ . Schematic representation of the imaginary-time path is shown in Fig. 2.2.

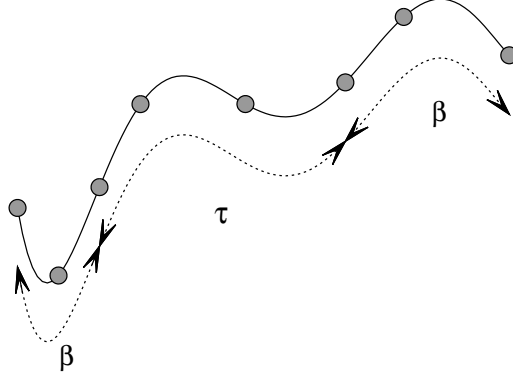


Figure 2.2: Schematic representation of an imaginary-time path: filled circles correspond to time-slices of the snake, the total imaginary time associated with the path has the length $2\beta + \tau$, β indicates the imaginary time interval that projects the trial function onto the ground state within the desired accuracy and τ is the internal portion of the path, that is used to calculate imaginary-time CFs. The path is discretized in imaginary-time steps ε .

2.3 Rotational energies

Spectral intensity in the absorption spectrum of the molecule solvated in the non-polar environment, such as a cluster of He atoms, is given by the Fermi golden rule, or equivalently, the Fourier transform of the molecular dipole-dipole CF

$$\begin{aligned} I(\omega) &= 2\pi \sum_n |\langle \Psi_0 | \hat{\mathbf{d}} | \Psi_n \rangle|^2 \delta(E_n - E_0 - \hbar\omega) \\ &= \int_{-\infty}^{\infty} dt e^{i\omega t} \langle \Psi_0 | \hat{\mathbf{d}}(t) \cdot \hat{\mathbf{d}}(0) | \Psi_0 \rangle, \end{aligned} \quad (2.14)$$

where Ψ_0 and Ψ_n are the ground- and excited-state wave functions of the system and E_0 and E_n are the corresponding energies. Inverting the above equation we find that the real-time correlation function has the form of a sum of oscillating exponentials:

$$\langle \Psi_0 | \hat{\mathbf{d}}(t) \cdot \hat{\mathbf{d}}(0) | \Psi_0 \rangle = \sum_{\omega} I(\omega) e^{-i\omega t}. \quad (2.15)$$

Given that RQMC easily provides imaginary-time CFs (see Eq. (1.29)), continuation to imaginary time transforms the oscillatory behaviour of the real-

time correlation function—which is responsible for the δ -like peaks in its Fourier transform—into a sum of decaying exponentials, whose decay constants are the excitation energies, and whose spectral weights are proportional to the absorption oscillator strengths

$$\mathcal{C}_{\hat{\mathbf{n}}}(\tau) = \langle \Psi_0 | \hat{\mathbf{n}} e^{-\tau \hat{H}} \hat{\mathbf{n}} | \Psi_0 \rangle = \sum_n |\langle \Psi_0 | \hat{\mathbf{n}} | \Psi_n \rangle|^2 e^{-(E_n - E_0)\tau} = \sum_n A_n e^{-\varepsilon_n \tau}, \quad (2.16)$$

where A_n is an oscillator strength, *i.e.* the spectral weight of a particular rotational excitation and ε_n is the energy of that excitation; $\hat{\mathbf{n}}$ is the unit vector along the molecular dipole, that for a linear molecule coincides with its orientation. The dipole selection rule implies that only states with angular momentum $J = 1$ can be optically excited from the spherically symmetric ground state:

$$\langle J' M' | \hat{\mathbf{d}} | J = 0 \rangle = 0 \text{ if } J' \neq 1. \quad (2.17)$$

Transition energies to rotational states with higher angular momenta J can be easily obtained from the multipole correlation functions $\mathcal{C}_J(\tau)$:

$$\mathcal{C}_J(\tau) = \left\langle \Psi_0 \left| \frac{4\pi}{2J+1} \sum_{M=-J}^{M=J} Y_{JM}^*(\hat{\mathbf{n}}(\tau)) Y_{JM}(\hat{\mathbf{n}}(0)) \right| \Psi_0 \right\rangle. \quad (2.18)$$

The rotational excitations contained in their spectral resolution satisfy the following selection rules:

$$\langle J' M' | Y_{JM}(\hat{\mathbf{n}}) | J'' = 0 \rangle = 0 \text{ if } J' \neq J \text{ or } M' \neq M. \quad (2.19)$$

We anticipate here that apart from the dipole operator, there is the wealth of tensor operators with $J = 1$ symmetry that could be constructed and whose imaginary-time correlations can, in principle, reveal different excitation energies and/or different spectral weights. This issue will be addressed in Chapter 4.

Schematic illustration of $\mathcal{C}_{\hat{\mathbf{n}}}(\tau)$ CF that contains three spectral components $E_1 < E_2 < E_3$, is shown in Fig. 2.3. In order to extract rotational excitations from this imaginary-time CF one needs to apply inverse Laplace transform $\hat{\mathcal{L}}^{-1}$, where $\hat{\mathcal{L}}(\cdot) = \int_0^\infty e^{-\tau E}(\cdot) d\tau$:

$$\hat{\mathcal{L}} \mathcal{C}_{\hat{\mathbf{n}}}(\tau) = \int_0^\infty e^{-\tau E} \mathcal{C}_{\hat{\mathbf{n}}}(\tau) d\tau = \sum_n \frac{A_n}{E - \varepsilon_n}. \quad (2.20)$$

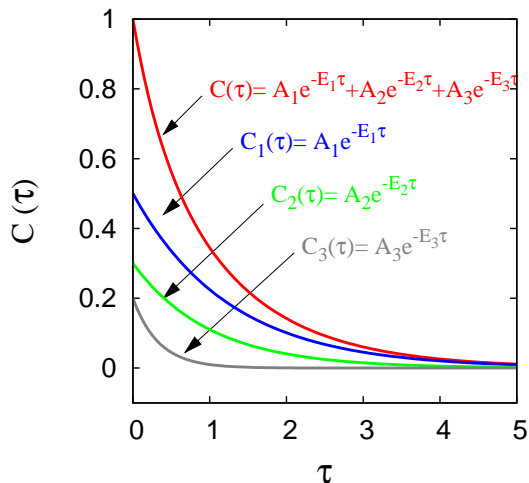


Figure 2.3: Schematic representation of CF in Eq. (2.16) (red line), containing three spectral components $E_1 < E_2 < E_3$ (blue, green and gray line, respectively).

The poles of $\hat{\mathcal{L}}\mathcal{C}_{\hat{n}}(\tau)$ define the excitation energies of the system. By inverting the latter, rotational energies are obtained. In principle, the inverse Laplace transform (ILT) is a difficult and ill-conditioned problem [44]. However, in our particular case, situation is rather favorable because the rotational spectrum of the system is exhausted by a small number of well-separated rotational lines which can be reliably extracted. This is so because of the weak interaction between He atoms and an embedded molecule and the scarcity of the low-lying states in the bosonic solvent available to couple with a molecular rotation. Thus we are able to reliably extract the rotational energies ε_n and the corresponding spectral weights A_n as parameters in the multi-exponential fit, Eq. (2.16).

2.4 Convergence issues

In this Section we demonstrate some of the procedures we routinely perform in order to check the convergence of our results. The first two issues that we will illustrate are the biases present in the RQMC simulation due to the finite imaginary time-step ε employed in the short-time approximation for the quantum propagator (Eq. (2.6)) and the finite projection time β (see

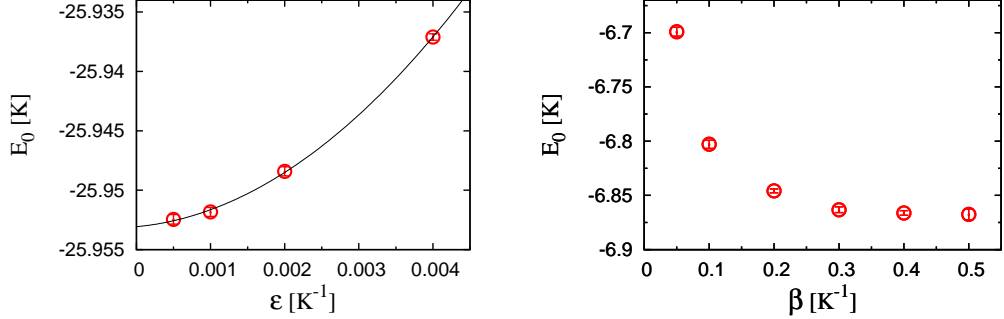


Figure 2.4: Left panel: dependence of the ground state energy of $\text{CO}_2@^4\text{He}_1$ on the time step ϵ . The curve corresponds to a second-order polynomial fit. Right panel: the ground state energy of $\text{CO}@^4\text{He}_{30}$ cluster as a function of the projection time β .

Eq. (2.9)). Their effect could be estimated, by performing simulations for different values of ϵ and β , and eliminated, if needed, by extrapolating the results to $\epsilon \rightarrow 0$ and $\beta \rightarrow \infty$. An illustration of the convergence tests with respect to ϵ and β are displayed in Fig. 2.4. In this thesis, $2\beta + \tau$ is typically between 1K^{-1} and 2K^{-1} , the time-step is $\epsilon=0.001\text{K}^{-1}$ and the projection time $\beta=0.5\text{K}^{-1}$, since the previous studies of similar systems [19, 20, 24] revealed that the residual bias thus obtained is smaller than the desired accuracy.

Further, the accuracy of the estimates can be affected by the range of the imaginary-time τ used to calculate CFs. Since we are interested in the lowest excitations in the spectra, the imaginary-time τ has to be long enough, so that the multi-exponential fit can clearly resolve the presence of the lowest modes in the spectrum. The difficulties to accurately extract the lowest energy ϵ_1 in the spectrum of $\text{CO}_2@^4\text{He}_1$ if τ is too short is demonstrated on the right panel of Fig. 2.5.

Finally, we illustrate the procedure of extracting rotational excitations from imaginary-time CFs by performing the multi-exponential fit in Eq. (2.16). The reliability of our fitting procedure is assessed by checking how our results depend on the number of exponentials, N , entering the fit. Namely, one has to keep trace of the convergence of fitting parameters, rotational energies ϵ_n and corresponding spectral weights A_n , with respect to N . While

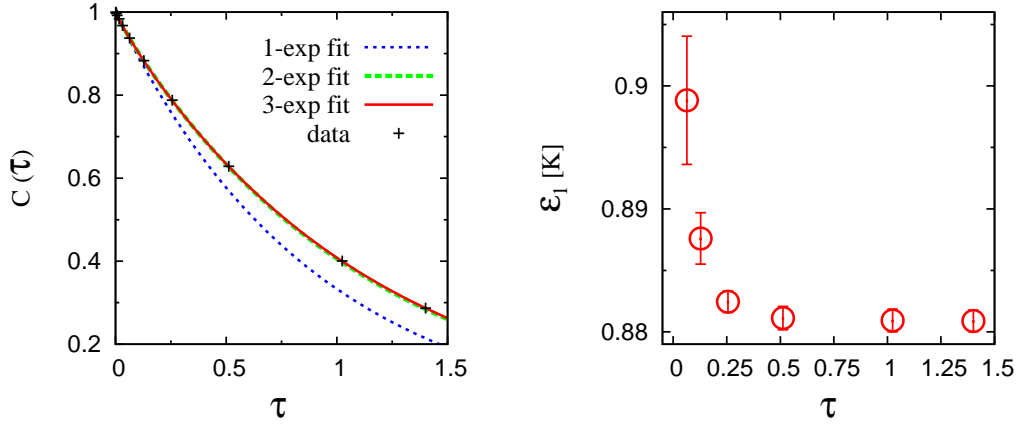


Figure 2.5: Left panel: imaginary-time CF $C_n(\tau)$ for $\text{CO}_2@^4\text{He}_1$ (crosses) shown along with 1-exponential (blue dashed line), 2-exponential (green dashed line) and 3-exponential (red line) fits. Right panel: dependence of ϵ_1 , extracted from the 3-exponential fit, on the imaginary-time range τ used to calculate CF.

a single exponential is never sufficient to fit the data, by increasing N one quickly reaches the situation of over-fitting, when the data are equally well fitted by vastly different spectra, a manifestation of the ill-conditioned ILT. However, we are often able to reliably extract the useful information before the ambiguity of the ILT sets in.

As an example of our fitting procedure, we show the evolution of fitting parameters extracted from $C_n(\tau)$ CF for $\text{CO}_2@^4\text{He}_1$ in Fig. 2.6. Despite the fact that the spectrum is dominated by a single excitation $\epsilon_1 \sim 1\text{K}$ carrying almost the whole spectral weight $A_1 \approx 99\%$, one and two exponentials are not sufficient to fit the data, as indicated by a high values of reduced χ^2 parameters for the fits with $N = 1$ and $N = 2$. Data points of the calculated imaginary-time CF, along with the curves of 1-, 2- and 3-exponential fits, are displayed in the left panel of Fig. 2.5. We note from Fig. 2.6 that the energies ϵ_n vary smoothly with the number of exponentials N and that the convergence to the picture with three relevant excitations in the system does not change upon the addition of the fourth exponential in the fit. This justifies our choice to use $N = 3$ in this case.

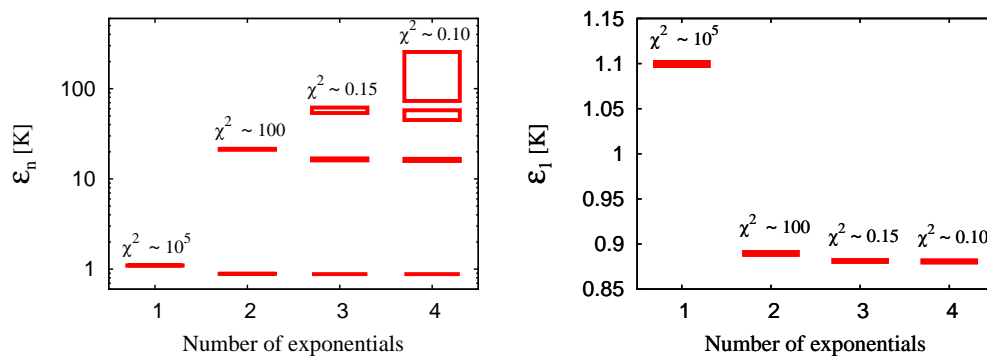


Figure 2.6: Left panel: the rotational excitations ε_n extracted from 1-, 2-, 3- and 4-exponential fits of $\mathcal{C}_{\hat{n}}(\tau)$ CF for $\text{CO}_2@^4\text{He}_1$. Right panel: the enlarged low-energy region showing the convergence of the lowest excitation in the system ε_1 with the number of exponentials. Centers of rectangles correspond to the extracted energies, while their half-heights correspond to the estimated statistical errors.

Chapter 3

CO-doped ^4He clusters

Often there are available experimental data on the roto-vibrational spectra of ^4He -solvated molecules¹, that include $P(J)$ and $R(J)$ branches² in their infrared (IR) spectra, for several values of J . This is the case for OCS molecule solvated in small [6] and medium-sized clusters [9], as well as in large He nanodroplets [45]. An example of a such IR spectra is displayed in Fig. 1. Observing these transitions allows one to estimate the values of the size-dependent effective rotational constants B_N and the shifts in the molecular vibrational transitions $\Delta\nu_N$ in He clusters (with respect to the monomer band origin ν_0), using the energy expression for a linear rotor:

$$E_N(R(0)) = \nu_0 + \Delta\nu_N + B_N J(J + 1). \quad (3.1)$$

However, CO is a light molecule, whose relatively large gas-phase rotational constant $B_0 \sim 2 \text{ cm}^{-1}$ causes its first excited rotational state $J = 1$ to have a negligible probability of being occupied at the typical He cluster temperature $\sim 0.4 \text{ K}$ [46]. Since only the ground rotational level $J = 0$ is significantly populated, the IR spectra of $\text{CO}@^4\text{He}_N$ clusters exhibit a single $R(0)$ roto-vibrational line, due to the simultaneous vibrational $\nu = 1 \leftarrow 0$ and rotational $J = 1 \leftarrow 0$ transition of the molecule [25, 26, 47]. However, the separation of rotational and vibrational contributions in the observed

¹In the following, when we refer to He we mean ^4He .

² $P(J)$ branch includes the excitations that correspond to the simultaneous vibrational $\nu = 1 \leftarrow 0$ and rotational $J \rightarrow J - 1$ transition of the molecule, while $R(J)$ branch consists of $\nu = 1 \leftarrow 0$ and $J \rightarrow J + 1$ transitions.

R(0) transition (*i.e.* determination of B_N and $\Delta\nu_N$) from the single line is not possible. Alternatively, or complementary, microwave (MW) measurements that directly couple to rotational excitations could be used. Very few studies in MW spectral region have been performed, and they are limited to the CO-He dimer and small- N clusters [48, 49]. Therefore, there is no MW measurement that would directly couple CO rotational excitation in large He nanodroplets, so that the CO nanodroplet limit, B_∞ , is unknown.

However, Havenith *et al.* [23] proposed a new method to determine the B_∞ value for CO from the four roto-vibrational R(0) transitions, each for a nanodroplet seeded with a $^{12}\text{C}^{16}\text{O}$, $^{12}\text{C}^{18}\text{O}$, $^{13}\text{C}^{16}\text{O}$ and $^{13}\text{C}^{18}\text{O}$ isotopomer, respectively. Assuming that the vibrational shift in large He nanodroplets is insensitive to the isotopic substitution, the following relation holds for the i -th isotopomer: $E_\infty^{(i)}(R(0)) = \nu_0^{(i)} + \Delta\nu_\infty + 2B_\infty^{(i)}$. The idea of this unconventional experiment was to indirectly estimate both the CO effective rotational constant B_∞ and the shift in its vibrational transition $\Delta\nu_\infty$ from four R(0) transitions, using isotopic effect. To this purpose, they reduced the number of unknown variables by assuming a two-dimensional dependence of the effective rotational constant, *i.e.* $B^{(i)} = B(B_0^{(i)}, \Delta z^{(i)})$, where $B_0^{(i)}$ is the gas-phase value for the i -th isotopomer and $\Delta z^{(i)}$ is the shift of its center of mass (with respect to the normal isotopomer $^{12}\text{C}^{16}\text{O}$) that mostly affects the change of CO-He potential upon isotopic substitution (see Fig. 3.1³), since the equilibrium CO-He distance stays unmodified. This so-called ‘‘reduced mass/center of mass shift’’ model is further specified by a linear expansion of the effective rotational constants:

$$B^{(i)} = \frac{\mu^{(1)}}{\mu^{(i)}} B^{(1)} + \frac{\partial B}{\partial \Delta z} \Delta z^{(i)}, \quad (3.2)$$

where $\mu^{(i)}$ is the reduced mass of the i -th isotopomer. The value of the partial derivative $\frac{\partial B}{\partial \Delta z}$ was calculated by means of correlated sampling DMC

³The effective CO-He potential becomes more or less isotropic depending on the separation between the center of rotation, *i.e.* the center of mass and the so called ‘‘center of interaction’’, the point where the effective potential anisotropy is minimized. It is found both experimentally [25] and theoretically [23], that $^{13}\text{C}^{16}\text{O}$ rotates more freely than $^{12}\text{C}^{18}\text{O}$, although their reduced masses are very similar. Results of our simulations also show this effect (see Appendix A.)

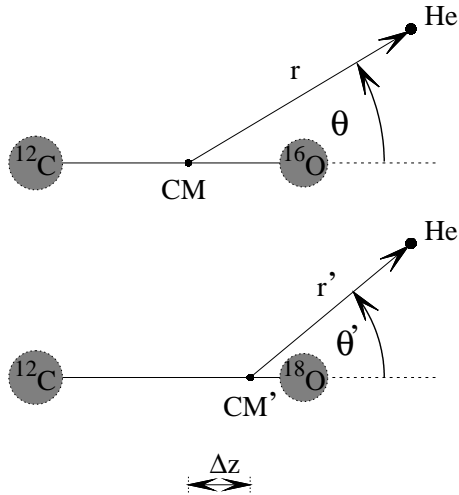


Figure 3.1: Schematic representation of the change in CO-He potential from $V(r, \theta)$ to $V(r', \theta')$ upon the shift Δz of CO center-of-mass when switching from $^{12}\text{C}^{16}\text{O}$ to $^{12}\text{C}^{18}\text{O}$ isotopomer.

and Correlated Basis Function (CBF) theory [23]. Finally, the relations

$$E_{\infty}^{(i)}(R(0)) - \nu_0^{(i)} - 2 \frac{\partial B}{\partial \Delta z} \Delta z^{(i)} = \Delta \nu_{\infty} + 2 \frac{\mu^{(1)}}{\mu^{(i)}} B_{\infty}^{(1)} \quad (3.3)$$

are used to perform a linear fit with respect to the unknown effective rotational constant of the normal isotopomer $B_{\infty}^{(1)}$ and the shift of vibrational transition in He nanodroplets, $\Delta \nu_{\infty}$. This fit is shown in Fig. 3.2. For more details on the quantities appearing in Eq. (3.3) see Tab. (A.3) in Appendix A.

The resulting fitting parameters are $\Delta \nu_{\infty} = (-0.254 \pm 0.07) \text{ cm}^{-1}$ and $B_{\infty} = (63 \pm 2)\% B_0$, that is significantly lower than $\approx 78\% B_0$, the value inferred from the RQMC simulations of CO dynamics in medium-sized He clusters, consisting of up to $N = 30$ atoms [24]. For comparison, the effective rotational constant of HCN, a molecule similar to CO, in the size-range $N = 15 - 50$ [19] already coincides with the experimental MW measurement of B_{∞} in He nanodroplets [50]. Thus the new prediction of Ref. [23] for B_{∞} contradicts the prediction coming from RQMC simulations [24], that is somewhat surprising and deserves further investigation.

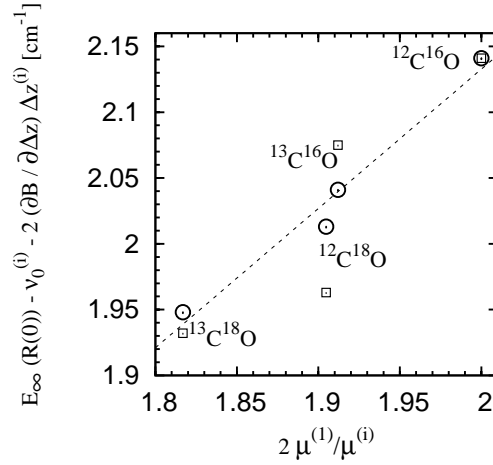


Figure 3.2: Linear fit of the left-hand side of Eq. (3.3) for four isotopic species plotted versus the ratios of reduced masses, according to “reduced mass/center of mass shift” model. The importance of the effect of isotope-induced center-of-mass shift for the quality of the fit is emphasized: open circles (effect included) and open squares (effect neglected).

Havenith *et al.* propose an explanation for the drop of the value of B_∞ for CO, in terms of the coupling of a molecular rotation with bulk-like He modes in large He nanodroplets, that happens for CO, but not for HCN, due to a slightly more anisotropic CO potential, compared to that of HCN. In order to verify the effect of the potential anisotropy on the coupling of molecular rotations with He-modes, we have carried out computational experiments involving fudged CO and HCN molecules that we present in Sec. 3.1.

Motivated by the nanodroplet experiment of Ref. [23], McKellar *et al.* extended their previous size-selective IR study of small CO@He $_N$ clusters in the size-range $N = 2 - 20$ for the normal $^{12}\text{C}^{16}\text{O}$ isotopomer in Ref. [25] (and for $^{12}\text{C}^{18}\text{O}$ and $^{13}\text{C}^{16}\text{O}$ isotopomers in Ref. [47]) to $^{13}\text{C}^{18}\text{O}$, allowing for the detection and assignment of roto-vibrational R(0) transitions for much larger clusters, up to $N \approx 100$ He atoms [26]. However, the situation remained unclear since the isotopic analysis of their IR data for all the four isotopic species, in terms of the proposed “reduced mass/center of mass shift” model, Eq. (3.2), did not work in the expected way. Namely, the scattered values of the fitting parameters for the effective rotational constants B_N and vibra-

tional shifts $\Delta\nu_N$, suggested that a similar isotopic analysis is inappropriate for their data. Further, the MW measurements that are becoming available in small clusters, up to $N \approx 10$, happen to confirm the RQMC rotational energies [49].

The present state of experimental findings motivated us to carry out the study of He-solvated CO by means of RQMC simulations in order to help resolving these issues. With respect to the previous CO study [24], we have extended our calculations to four isotopic species, with the aim to study isotopic effect, and pushed the simulations towards larger cluster sizes. Namely, rotational energies of four CO isotopomers embedded in clusters consisting up to $N = 100$ He atoms are calculated. Further, the vibrational shifts are estimated for selected cluster-sizes up to $N = 200$, thus filling the gap between the medium-sized clusters and nanodroplets. We use recently reported, CBS+corr potential of Peterson and McBane, Ref. [51], that is supposed to be very accurate since it gives the correct value for vibrational shift of CO-He dimer, while the SAPT potential of Heijmen *et al.* [52], employed in the previous RQMC study, overestimates it for a factor of two. On the other side, both potentials reveal similar rotational energies. Thus we were guided by the idea that CO-He potential of high accuracy will allow us to accurately calculate vibrational shift and together with highly accurate rotational spectra available with RQMC, draw the conclusion about the approach of CO effective rotational constant to its nanodroplet limit.

3.1 Effect of the anisotropy: CO vs HCN

The physical mechanism invoked in Ref. [23] to explain the lowering of B_∞ for CO in large He nanodroplets, as well as its disparity with otherwise very similar HCN molecule, is the coupling of molecular rotation with He bulk-like phonons. These collective He excitations can have sufficiently low energies to match molecular rotational excitation only at low enough wave vector, or equivalently, at large enough system size. In order to simulate a somewhat similar physical effect with manageable system sizes, we consider a cluster with $N = 20$ He atoms that corresponds to the size when one full He solvation shell around the molecule has already been formed. Further, we artificially

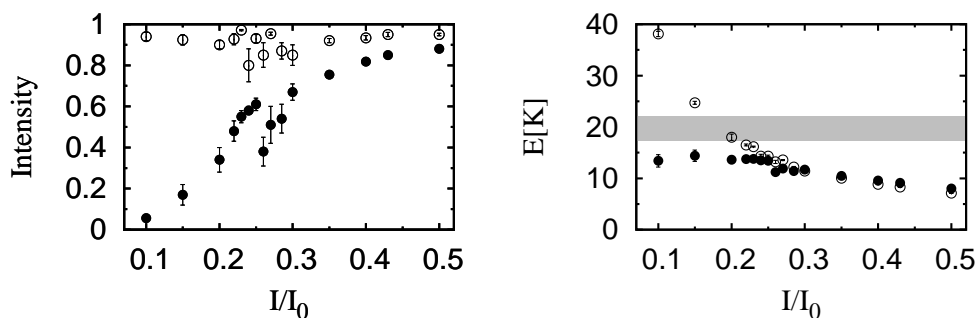


Figure 3.3: The lowest rotational energy (right panel) and its spectral weight (left panel) for fictitious molecular impurities solvated with 20 He atoms. Fudged molecules (CO, filled circles and HCN, open circles) have the same mass and the same interaction with He as the physical molecules. Their moments of inertia, instead, are reduced with respect to the physical value by the factor I/I_0 indicated by the abscissa. The shaded region encompasses the energy values of a He-related excitation that carries angular momentum $J = 1$ (similar for both dopants and almost independent of the ratio I/I_0).

increase the gas-phase rotational constants of CO and HCN molecules. By doing so, the rotational energies of the fudged molecules eventually cross a high-energy cluster excitation that involves mostly He motions and carries angular momentum $J = 1$. This is the so-called *end-over-end* mode [24] and we will inspect it more closely in the next Chapter. Here we just note that due to its He-related character, only a weak dependence of this mode on the molecular rotational constant is expected. The coupling of the molecular rotation with *end-over-end* mode is illustrated in Fig. 3.3 for both CO and HCN molecules. We observe that the lowest rotational excitation of the cluster doped with fudged CO is repelled by a solvent-related excitation, with a concurrent loss of spectral weight. Correspondingly, a second excitation (not shown for clarity), higher in energy than the He-related mode, gains weight and further shifts upward. Interestingly, using HCN instead of CO as a dopant molecule, the molecular rotation is not significantly affected by a nearly degenerate He-related cluster excitation [24] (incidentally this suggests that the splitting of the measured $R(0)$ series close to $N = 15$ for

CO@He_N clusters [25] might not be observed in a similar experiment with HCN). This is consistent with the observation that the almost constant value of B_N predicted in Ref. [19] in the size range $N = 15 - 50$ for HCN@He_N coincides with the measured nanodroplet value [50].

The CBS calculation of Ref. [23] explains this disparity between CO and HCN in terms of the different degree of anisotropy of the respective interaction potentials with He. The present calculation gives support to this mechanism, but it does not have obvious implications on the displacement of the rotational excitation caused by the presence of a “quasi continuum” of states in the nanodroplet (which instead clearly affects the line shape [53]). In particular, appearance of broad phonon-like He modes is expected to set in gradually in the low-lying region, evolving from more localized He modes higher in energy, as the number of He atoms increases, as calculated in Ref. [54]. Our simulations do not resemble such a situation, since the He-related band appearing in our calculations is narrow and fixed in energy, so that it is unclear how low-lying continuum He states in a real droplet will influence the rotational spectra of the molecule. Although indirectly, the latter argument on the different behaviour calculated for CO and HCN goes in favor to the mechanism proposed in Ref. [23] to explain the lowering of CO effective rotational constant in large He nanodroplets.

3.2 Structural properties

The structural properties of doped He clusters such as energetics and the density profiles of the He atoms around the molecule represent nowadays a sort of standard information, available with high accuracy from QMC simulations [8, 55, 56, 57]. Here we review them briefly for CO@He_N clusters, so that we can refer to them in the later discussion.

The atomic He density distribution ρ_N in the ground state for a cluster containing N He atoms is defined as a pair correlation function

$$\rho_N(\mathbf{r}) = \left\langle \sum_{i=1}^N \delta(\mathbf{r}, \mathbf{r}_i - \mathbf{R}) \right\rangle, \quad (3.4)$$

where \mathbf{R} denotes the center of the mass of the molecule and \mathbf{r}_i describe po-

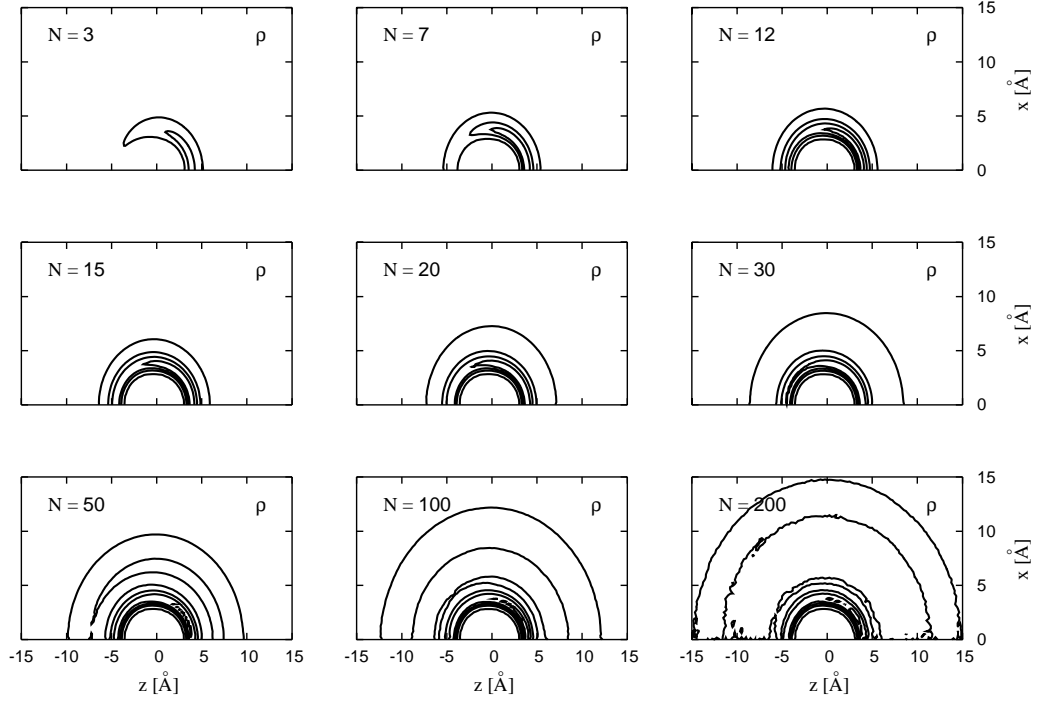


Figure 3.4: Contour plots of He density ρ_N for selected cluster sizes in $\text{CO}@He_N$ cluster. Contour levels start from 0.001 with 0.005 increments in units of Å^{-3} .

sitions of He atoms. Contour plots of He density around CO molecule are displayed in Fig. 3.4 for selected cluster sizes. He atoms start to fill the potential well on the oxygen side (see Fig. 3.9). Already for $N > 3$ the shallow and weak CO-He interaction causes some of the He density to spill out all around the molecule, indicating that CO is rapidly coated by He. As the number of He atom increases, the He solvation structure evolves and its build-up is displayed in Fig. 3.5. We see that the He density is modulated in the presence of the molecule, so that He solvation shells are formed, however in a fairly isotropic manner, as demonstrated in Fig. 3.4. For the largest cluster studied, $\text{CO}@He_{200}$, the radial density profile is shown in Fig. 3.6. We can notice the formation of four solvation shells around CO. The position of the first and the second solvation shell is clearly defined, while the location of the third and the fourth shell is more tentative, indicated with the corresponding shoulders in the density profile. The VMC density profile depicted in the

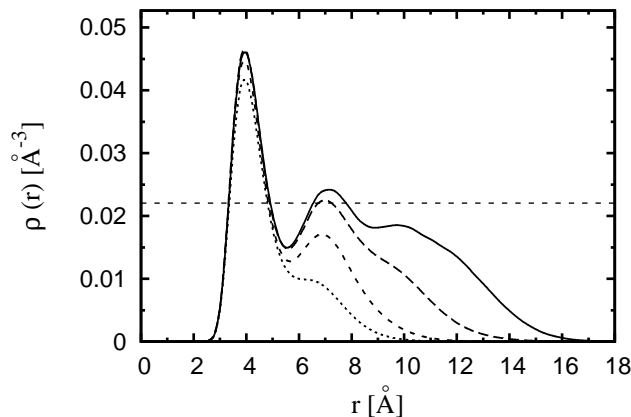


Figure 3.5: Radial density profiles of CO@He_N clusters for $N = 20, 30, 50, 100$ and 200 . The curves are normalized such that $4\pi \int \rho_N(r)r^2 dr = N$. The horizontal line is the equilibrium density in the bulk He.

same figure has significantly less structure, indicating that in this strongly correlated system, improvement upon VMC approximative treatment is essential (see Secs. 1.3 and 2.2). A closer understanding of the solvation process can be obtained from the analysis of the incremental binding energy $\Delta E_N = E_{N-1} - E_N$ (Fig. 3.7). ΔE_N first decreases up to $N = 4 - 5$, indicating increasing binding that is mostly due to CO-He attraction. For larger N the spill-out of He atoms out of the main potential well, causes binding to decrease, first slowly and then starting from $N = 10$ more rapidly, due to reduction of CO-He interaction. This proceeds down to the maximum attained around $N \approx 20$, when the building of the first solvation shell is already completed. Note that the value of weakest binding is significantly lower than the binding in the bulk He. This comes from the increased localization of atoms in the first solvation shell that results in the high value of kinetic energy. From here on, binding slowly increases, tending to the nanodroplet regime, that is attained for much larger sizes than studied here. The attractive CO-He interaction induces the solvent density in the vicinity of the molecule to be more than twice larger than that observed in the bulk He. As a consequence of the increasing density with the increasing number of He atoms (see Fig. 3.8), He-He repulsive interactions lead to the formation of the second and further solvation shells.

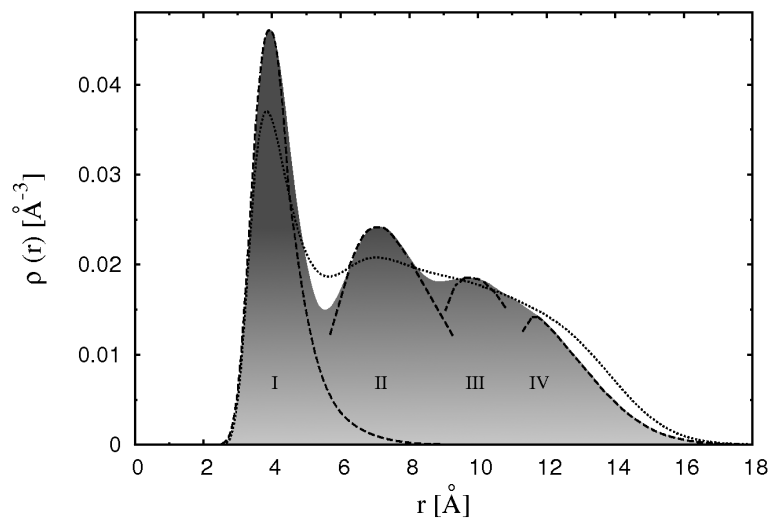


Figure 3.6: Radial density profile of CO@He₂₀₀ cluster obtained with RQMC (shaded region). Long dashed lines serve as a guide for an eye to identify approximate locations of different solvation shells. Short dashed line represents VMC radial density profile.

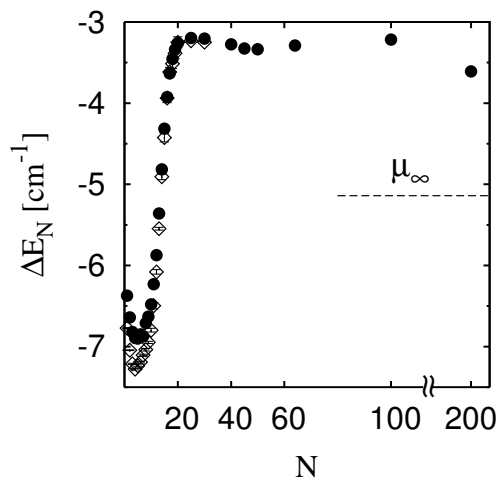


Figure 3.7: Incremental atomic binding energy, the “chemical potential” $\Delta E_N = [E(N) - E(M)] / (N - M)$, with M the largest available cluster size smaller than N , using CBS+corr potential (filled circles) and SAPT potential (open diamonds); the horizontal dashed line is the bulk He chemical potential [13].

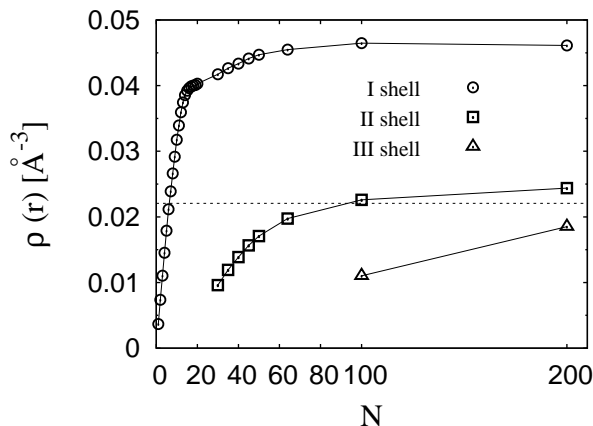


Figure 3.8: Peak densities of different solvation shells in CO@He_N clusters as a function of the number of He atoms N . The horizontal line is the equilibrium density of the bulk He.

3.3 Vibrational shift

The soft He environment does not alter the symmetry of an embedded rotor, so that roto-vibrational spectra of He-solvated molecules is well-fitted with the expression given by Eq. (3.1). Solvent-induced vibrational shifts are quite small and typically do not exceed 0.1% of the vibrational band origin in the gas-phase. They are caused by the change in a He-molecule interaction potential upon a molecular vibrational excitation. Given the separation of time-scales involving the fast vibrational motion of a molecule and slow He motions, adiabatic separation of the two is justified. Thus in RQMC calculations we use CO-He interaction potential $V_{\alpha\alpha}$ averaged over the period of molecular vibration, in either the molecular ground state ($\alpha=0$) or the first excited vibrational state ($\alpha=1$). As mentioned previously, we use the recent so-called CBS+corr potential of Peterson and McBane [51], along with the SAPT potential of Heijmen *et al.* [52] that is employed in previous RQMC studies of CO [24]. The contour plots of the these two potentials are shown in Fig. 3.9 for $\alpha=0$. The vibrational shift is calculated as the difference between the rotational ground-state energies of the cluster, calculated with potentials V_{00} and V_{11} , respectively. As this difference is small with respect to the individual energies, whose statistical uncertainties grow with the cluster size,

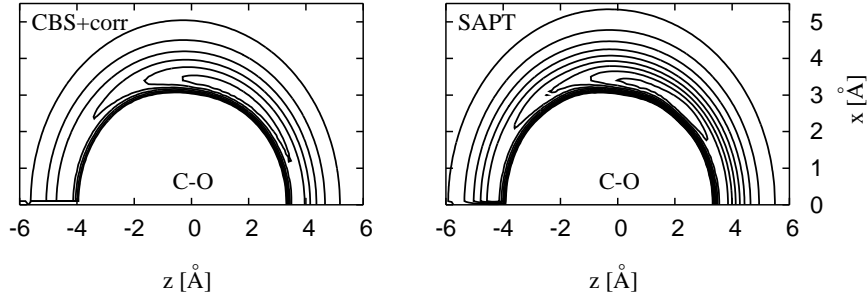


Figure 3.9: Contour plots of the CBS+corr (left panel) and the SAPT (right panel) potentials in the ground vibrational state of the CO molecule. Contour levels start from $V_\infty = 0$ to negative values, with spacing between levels equal to 5 K. Both potentials are characterized by one single shallow well, on the oxygen side. However, SAPT potential has a deeper and narrower main potential well, while the CBS+corr is shallower and broader. SAPT potential well has a minimum value of $V_m^{SAPT} = -34.13\text{K}$, while CBS+corr has $V_m^{CBS+corr} = -32.12\text{K}$, at a distance $r_m = 3.45\text{\AA}$, but with different angular coordinate being $\theta_m^{SAPT} = 48.4^\circ$ and $\theta_m^{CBS+corr} = 70.8^\circ$ with respect to the molecular axis pointing from carbon to oxygen atom.

we resort to a perturbative approach and evaluate the vibrational shift as $\Delta\nu_N = \langle \Psi_0 | V_{11} - V_{00} | \Psi_0 \rangle$. The expectation value of the difference $V_{11} - V_{00}$ in the ground state of a cluster is calculated with either potential as:

$$\Delta\nu_N = \int (V_{11}(\mathbf{r}) - V_{00}(\mathbf{r})) \rho(\mathbf{r}) d^3\mathbf{r}. \quad (3.5)$$

Results for the size-dependent vibrational shift $\Delta\nu_N$ calculated in the range $N = 1 - 200$, together with a few direct, non-perturbative estimates at selected N values, are shown in Fig. 3.10. Comparison with a complete calculations, performed at selected cluster sizes up to $N = 30$, shows that this perturbative approach is accurate enough for our purposes. The difference between the perturbative and the direct estimates is largest around $N = 20$, possibly due to the change in the behaviour of chemical potential at this cluster size (Fig. 3.7). The vibrational shift is red for both potentials used, that corresponds to the stronger binding of the cluster for the molecule in its first excited vibrational state. Using the CBS+corr potential, the initial

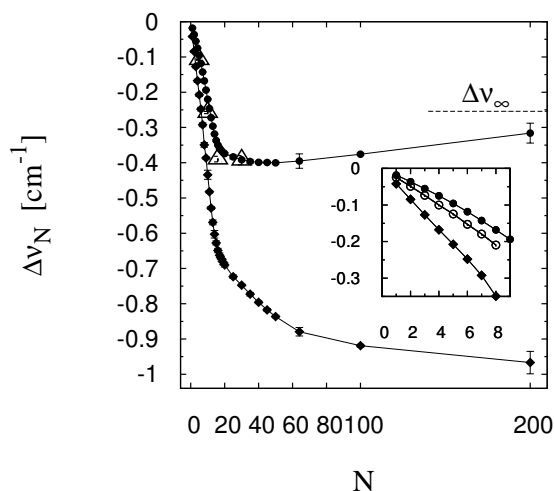


Figure 3.10: Vibrational shift in CO@He_N clusters: perturbative estimates using CBS+corr potential (filled circles) and SAPT potential (filled diamonds) and complete calculations with CBS+corr potential (open triangles). The dashed line is the nanodroplet limit according to Ref. [23]. Inset emphasizes the small-size range, where the experimental values are available (open circles), obtained by combining the IR measurements of Ref. [25] and the MW measurements of Ref. [49].

slope of the vibrational shift closely matches the value measured for the binary complex, and the red shift saturates around $N \approx 50$ with a weak upturn at larger sizes. With the SAPT potential the initial slope is twice as large and the saturation of the red shift drifts to larger sizes and it appears to be monotonously decreasing, at least in the size range studied here. The N dependence of the vibrational shift in the range $N = 1 - 20$ is qualitatively similar for both potentials, with an almost linear behaviour within the first solvation shell, and a significant change in the slope between $N = 15$ and 20 . This size range matches the cluster size when the abrupt change in the slope of the chemical potential indicates the completion of the first solvation shell (Fig. 3.7).

In general, it is known that the vibrational shift results from contributions of both signs, red and blue. The blue shift usually comes from the He density in the vicinity of a molecule, since upon vibrational excitation a

molecular bond length increases and this increase occurs much faster than the corresponding He response, thus pushing towards the repulsive wall of a He-molecule interaction. This effectively increases the elastic force constant of a molecular vibrational mode, causing the increase of a vibrational energy. This usually happens for a bending vibrational modes, that typically exhibit larger amplitudes and smaller frequencies, so that the relative increase of the vibrational frequency in He clusters is more prominent with respect to stretching modes, as it is the case for umbrella-like vibrations of NH_3 [58]. Blue vibrational shifts are, however, observed in the stretching mode of He-solvated OCS [6, 9], CO_2 [22] and N_2O [59], so that this effect dominates the behaviour in the small-size regime for molecules whose interaction with He is stronger and more anisotropic than that of CO. The blue shift contribution is difficult to predict theoretically, and for the light CO that exhibits more isotropic interaction with He it turns out to be weaker than the red contribution.

Red vibrational shifts are more common in doped He clusters. Small red shifts less than $\sim 2 \text{ cm}^{-1}$ is what typically occurs in large He nanodroplets. This is consistent with the fact that, at least at large distances, the predominant contribution to the red vibrational shifts is coming from the attractive dipole-dipole interaction between the molecule and the He solvent, whose asymptotic form is of the type $\sim \frac{C_6}{r^6}$. Namely, the C_6 coefficient usually increases upon vibrational excitation, as the consequence of the average increase of a molecular dipole moment. Thus the difference $\Delta C_6 = C_6^{\nu=1} - C_6^{\nu=0}$ is expected to be positive. Indeed, this is the case for SAPT potential, but CBS+corr potential, on the contrary, reveals negative values, as shown in Fig. 3.12. This rises concerns about its accuracy at large distances. In order to further test the accuracy of the long-range tails of the CBS+corr and SAPT potentials, we define a “semi-empirical” vibrational shift obtained as the difference between the experimental $R(0)$ line positions of Ref. [26] and the monomer band origin of the normal isotopomer ν_0 , from which we have subtracted the mean value of the rotational energies in the size range $N = 16 - 50$, where a nearly constant value is predicted by RQMC simulations. This is motivated by the similarity of RQMC rotational spectra with both SAPT and CBS+corr potentials (see, later) which suggests that

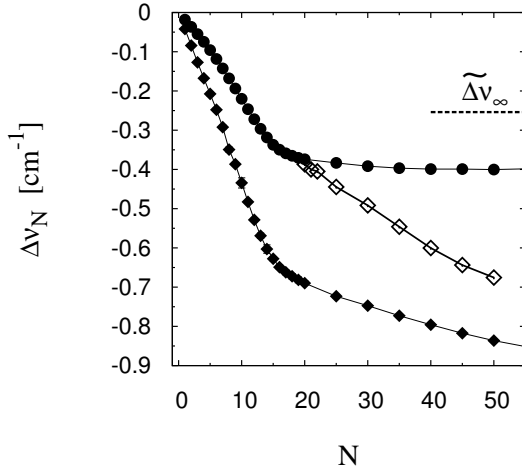


Figure 3.11: Vibrational shift in CO@He_N clusters: perturbative estimates using CBS+corr potential (filled circles), SAPT potential (filled diamonds), experimental values (open circles) [49], and “semi-empirical” estimate (open diamonds). The latter indicates the prediction coming from the combination of accurate RQMC energies and size-resolved experimental $R(0)$ lines [26] (see text). Horizontal dashed line is the nanodroplet limit according to Ref. [23].

they both might be accurate for rotational spectra. This “semi-empirical” vibrational shift, along with the perturbative estimates for CBS+corr and SAPT potentials is shown in Fig. 3.11. It suggests that even stronger slope for the red vibrational shift than the one coming from the SAPT potential, might be expected.

The reason for the unexpected blue upturn for the CBS+corr vibrational shift is presumably in the fact that the analytic expression of CBS+corr potential is fitted to a potential calculated for distances up to 7.9 \AA . From the extension of radial density profiles (Fig. 3.5), we see that already for $N = 30$ the calculation relies on extrapolation. In particular, the CBS+corr difference $V_{11}(R, \theta) - V_{00}(R, \theta)$ is positive for most values of θ at $R \geq 7 \text{ \AA}$, with an unphysical persistence of a significant angular dependence at large distances.

This explains the blue upturn of the CBS+corr vibrational shift, but it casts doubts on its accuracy at large sizes. In particular, the tendency seen in Fig. 3.10 to approach the estimated nanodroplet limit is possibly due to a deficiency of the potential at large distances. The SAPT method, in contrast to CBS+corr, directly determines the dispersion coefficients, thus

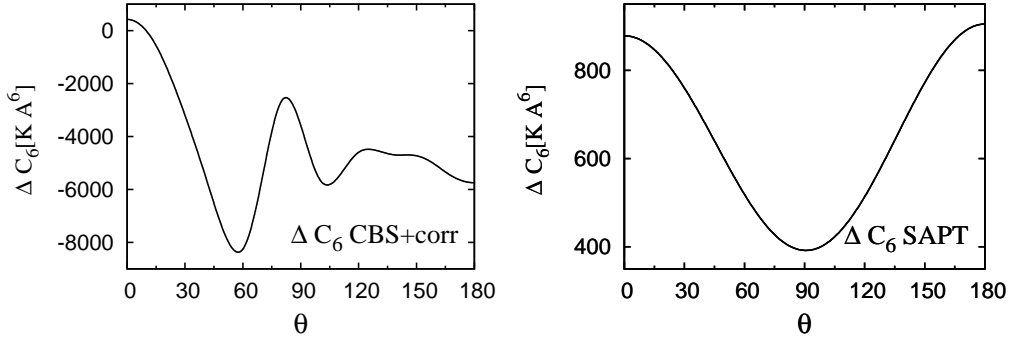


Figure 3.12: Variation of the C_6 long-range coefficient upon vibrational excitation of CO molecule for the CBS+corr (left panel) and SAPT (right panel) potentials, as a function of the angular coordinate θ . Note that the values of $\Delta C_6(\theta)$ for CBS+corr potential are negative, while for SAPT potential values are positive and closely follow $\sim P_2(\cos \theta)$, as it is expected theoretically [60].

affording a better accuracy at large distances [52]. It yields a negative value for $V_{11}(R, \theta) - V_{00}(R, \theta)$, with a weak nearly quadrupolar angular dependence (except, of course, close to the molecule).

Finally, we show that the behaviour of the C_6 coefficient upon vibrational excitation of CO is indeed consistent with the vibrational shifts calculated with the two potentials. The upper bound on the absolute value of the red vibrational shift can be estimated as

$$\Delta\nu_N(C_6) \propto \int d^3\mathbf{r} \rho_N(\mathbf{r}) \frac{\Delta C_6(\mathbf{r})}{r^6}, \quad (3.6)$$

where $C_6(\mathbf{r})$ in both vibrational states of the molecule depends only on the angular coordinate θ :

$$C_6(\theta) = - \lim_{r \rightarrow \infty} (V(r, \theta) r^6). \quad (3.7)$$

Values of $\Delta C_6(\theta)$ for both potential energy surfaces are shown on Fig. 3.12. We have calculated the contributions to these upper bounds for CO@He $_N$ clusters and the SAPT potential. The results are summarized in Tab. 3.1. All this values are obviously much larger than the values of the vibrational shift reported on Fig. 3.10 for the SAPT potential. But this is consistent with the fact that these values are just upper bounds, since any blue shift contribution and the effects of higher order polarizabilities (C_8, C_{10}, \dots) have been

N	20	50	100	200
$\Delta\nu_{C_6}(N)[\text{cm}^{-1}]$	-2.00	-2.33	-2.48	-2.50

Table 3.1: Upper bounds of the red vibrational shift $\Delta\nu_{C_6}$ for the SAPT potential, due to the increased C_6 value upon molecular vibrational excitation and different cluster sizes, calculated by means of Eq. (3.6).

N	50	100	200
$\Delta\nu_N^I[\text{cm}^{-1}]$	-0.388(3)	-0.413(3)	-0.42(2)

Table 3.2: Vibrational shift coming from the first solvation shell calculated with CBS+corr potential (see text).

neglected. Therefore, instead looking at the absolute values of the shifts, we rather look at their differences $\Delta\nu_{C_6}(N=20) - \Delta\nu_{C_6}(N=200) \approx -0.5\text{cm}^{-1}$, and $\Delta\nu_{C_6}(N=50) - \Delta\nu_{C_6}(N=200) \approx -0.17\text{cm}^{-1}$. From vibrational shifts reported on Fig. 3.10 it follows that the corresponding change when switching from $N=20$ to $N=200$, is -0.27cm^{-1} , and -0.12cm^{-1} when going from $N=50$ to $N=200$. Thus we can conclude that red vibrational shift calculated with the SAPT potential is mostly due to the change of C_6 coefficient upon molecular vibration.

Concerning the blue upturn of $\Delta\nu_N$ with CBS+corr potential in the size range $N=50-200$, we can speculate if it is predominantly coming from the positiveness of ΔC_6 upon vibrational excitation of the molecule predicted with this potential, or it can be the consequence of a slight increase of the density in the first solvation shell (see Fig. 3.8), that in principle could increase the vibrational frequency due to repulsive-like effects in the vicinity of the molecule, as previously discussed. In Tab. 3.2 we report the contributions to the vibrational shift calculated using CBS+corr potential that comes from the first He solvation shell. This contribution is calculated performing the integral in Eq. 3.5, with the upper bound of the radial coordinate $\approx 5.5\text{\AA}$, that corresponds to the spatial extension of the first He solvation shell around the molecule (see Fig. 3.5). We can conclude that the differ-

ence in the vibrational shift $\Delta\nu_N$ in the range $N = 50 - 200$ (being equal to $\approx 0.1\text{cm}^{-1}$, as seen from Fig. 3.10) is coming entirely from the tail of the He density distribution, and thus from the positive value of ΔC_6 coming from CBS+corr potential. The analysis of the vibrational shift presented in this Chapter we will use as the argument in the discussion of the approach of CO to its nanodroplet limit in Sec. 3.5.

3.4 Rotational excitations

The main feature in the cluster-size evolution of the IR spectra of $\text{CO}@He_N$ clusters is the presence of two series of R(0) transitions in the small size range, named *a*-type and *b*-type after the similar transitions observed in the spectra of CO-He dimer [25]. The higher energy *b*-type branch starts seven times stronger, but with increasing cluster size rapidly loses its weight and finally disappears around $N \approx 10$. On the contrary, the *a*-type branch gets stronger and after this size becomes almost independent on the cluster size and remains as a single prominent line in the spectra, describing nearly free molecular rotational mode characteristic for molecules embedded in large He nanodroplets. This spectral pattern is now understood [24] to stem from the dynamical asymmetry of the He density around CO molecule which leads to more than one important rotational line in small systems and vanishes for larger clusters.

Fig. 3.13 displays the comparison between available experimental data in both IR and MW spectral range and RQMC calculations. There is a remarkable agreement between the theory and experiment, as well as a great similarity in the rotational spectra calculated with both potentials, CBS+corr and SAPT. Detailed values of the calculated rotational excitations using both potentials and including all four CO isotopic species, are listed in tables Tab. A.1 and Tab. A.2 in Appendix A. Here we note that the close matching between the RQMC rotational energies obtained with CBS+corr and SAPT, supports the accuracy of the so-called “semi-empirical” vibrational shift displayed in Fig. 3.11. A small discrepancy between the theory and experiment is only seen towards the end of the higher energy *b*-type branch, where the theory has a slight tendency to overestimate it. Theoretical anal-

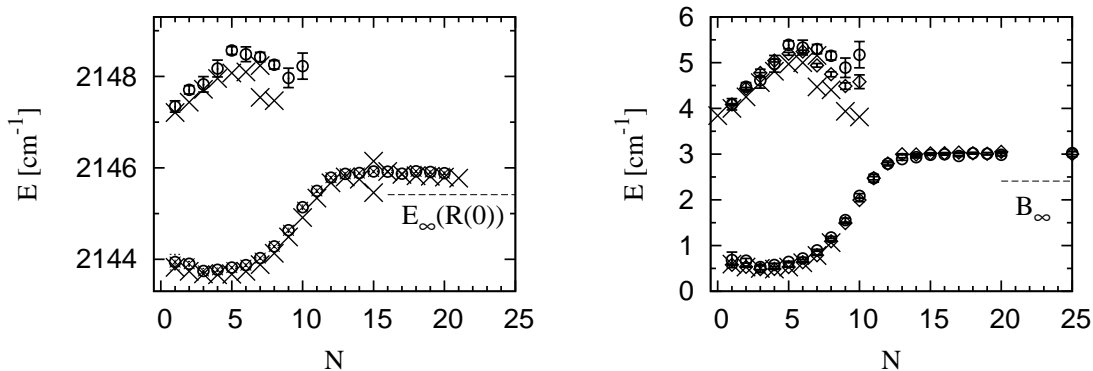


Figure 3.13: Left panel: energies of R(0) transitions in CO@He_N clusters (and normal ¹²C¹⁶O isotopomer); experimental line positions of Ref. [26] (crosses) and RQMC data obtained by summing up vibrational and rotational contributions in roto-vibrational lines, Eq. (3.1), using CBS+corr potential (open circles). The horizontal dashed line is energy of the R(0) transition measured in He nanodroplet [23]. Right panel: pure rotational energies of CO@He_N clusters: recent MW experiment (crosses) and RQMC calculations with CBS+corr potential (open circles) and SAPT potential (open diamonds). The horizontal dashed line is estimated CO effective rotational constant in He nanodroplet [23].

ysis is here complicated by the difficulty of the ILT to detect the weakening *b*-type excitation in the presence of the strengthening *a*-type excitation at lower energy [24]. The important fact to note here is that the situation is much more favorable for larger cluster sizes, where the *b*-type series has already disappeared and our spectral analysis is more robust. In particular, we stress that the *a*-type transitions describing nearly free molecular rotation in He are calculated with high accuracy for all cluster sizes and that we are exactly interested in this mode, since it is the only one present in large He nanodroplets. The only exception is seen at $N = 15$: this discrepancy has been related to symmetry arguments in Ref. [24] and we will further address this issue in the next Chapter, also in the relation to possible alternative assignments of experimental lines proposed in Ref. [26].

While the R(0) transition measured in the nanodroplet regime [23] is consistent with the calculated rotational excitations, under a reasonable assumption of a further red vibrational shift (see Fig. 3.11 and the left panel of Fig. 3.13), the value of the effective rotational constant in He nanodroplet

B_∞ , estimated in Ref. [23] is puzzling. Namely, it lays significantly lower than the value indicated by the plateau resulting from RQMC calculations in the size range $N = 15 - 30$ in the previous work [24] and in a wider range $N \leq 100$ in this study (see the right panel of Fig. 3.13 and also Fig. 3.14). This was surprising also because a similar saturation of B_N value calculated for a very similar HCN molecule in the cluster size $N = 15 - 50$ [19], already laid atop of its experimental nanodroplet value [50].

In order to test the isotopic analysis invoked in Ref. [23] to disentangle rotational and vibrational contributions in the observed $R(0)$ transitions, we have calculated rotational energies of four CO isotopic species in He clusters up to $N = 20$. Details on the different isotopomers, as well as on the applicability of the model proposed in Ref. [23] on RQMC simulation data can be found in Appendix A. We just note here that our data seem to indicate that the fitting analysis proposed in Ref. [23] is not working well with our data, however, the statistical errors are not small enough to draw definite conclusions. In the same cluster size-range, a similar conclusion is drawn by McKellar *et al.*, in Ref. [26]; namely, the isotopic analysis was not applicable with their IR data that whatsoever have no statistical errors.

3.5 Combining experimental and simulation data

Motivated with the nanodroplet experiment of Ref. [23], McKellar *et al.* [26] observed IR spectra of $\text{CO}@He_N$ taken under conditions of maximum clustering that allowed them to resolve individual $R(0)$ transitions up to $N \approx 50$, so that provisional assignments are reported up to this size. The resulting $R(0)$ a -type series is compared to simulation results calculated with CBS+corr in the size range $N = 16 - 100$ and with SAPT for $N = 16 - 30$ in Fig. 3.14⁴. Overall, the comparison between the calculated positions of roto-vibrational lines and provisional assignments [26] in the range $N = 20 - 50$ show that SAPT and CBS+corr data lay significantly lower and higher,

⁴The value at $N = 100$ has a somewhat uncertain statistical error, since it is obtained from simulations not much longer than the autocorrelation time of the random walk.

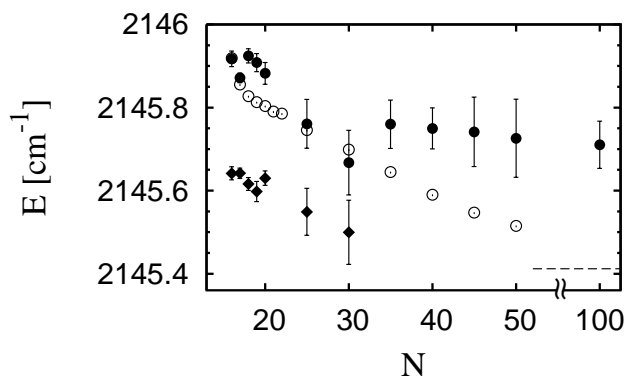


Figure 3.14: Detail of the a -type $R(0)$ transitions in $^{12}\text{C}^{16}\text{O}@\text{He}_N$ clusters for $N > 15$: RQMC results with the CBS+corr (filled circles) and the SAPT (filled diamonds) potential, and experiment (open circles) [26]; the horizontal line is the nanodroplet value [23]. To the pure rotational excitations coming from RQMC simulations we have added calculated vibrational shift.

respectively, than the experimental measurements. However, we have already observed a high similarity of RQMC rotational excitations calculated with both CBS+corr and SAPT potentials (see the right panel of Fig. 3.13 and Tab. A.1) and we thus conclude that the difference between roto-vibrational line positions calculated with two potentials comes almost entirely from the vibrational shift. Moreover, employing the “semi-empirical” vibrational shift discussed in Sec. 3.3 brings both RQMC series much closer to each other, as well as to the experimental data, which further supports its accuracy and consequently suggests that the estimated value for B_∞ of Ref. [23] is too small.

We conclude this Chapter with summarizing the arguments on the approach of CO to its nanodroplet limit, we have obtained by combining experimental and simulation data. Namely, although indirectly, our calculations on the fudged CO and HCN molecules go in favor of the mechanism proposed in Ref. [23] to explain that the lowering of CO effective rotational constant in large He nanodroplets is due to the coupling of the molecular rotation with bulk-like He modes. On the other hand, we have demonstrated that the value $\Delta\nu_\infty$ inferred from the fitting analysis of Ref. [23] corresponds to the improbable strong blue upturn of vibrational shift in large clusters. In the same time, accurate RQMC rotational energies accompanied by a

physically plausible further red vibrational shift would bring to matching calculated and measured roto-vibrational energies in small-to-medium sized clusters. We think that the latter is a much stronger argument against the proposed B_∞ value than the former one that is in favor. In summary, we overall conclude that the value B_∞ reported in Ref. [23] is too low and that CO should attain the limiting value of its effective rotational constant soon after completion of the first He solvation shell.

Chapter 4

Fine features in the spectra of doped ^4He clusters

While considerable understanding of systems containing a molecule embedded in ^4He droplet¹ has been gained with help of RQMC simulations (*e.g.* their structure, their NCRI and the relation between them), many subtle features of the observed spectra still remain to be understood. For instance, the residual interaction between the effective rotor (constituted by the molecule and the part of the He density that is dragged around by it) and the rest of the host gives rise to such phenomena as line broadening and splitting, and satellite bands (faint spectral features that would be absent in the spectrum of a rigid rotor), which often escape a complete theoretical understanding. We have already encountered such phenomena in the previous Chapter where we have seen that a limited number of split R(0) lines is experimentally observed in IR spectra of small CO@He_N clusters (see the left panel of Fig. 3.13 and experimental data indicated by crosses). A further example is the satellite band that is observed to accompany the strong R(0) roto-vibrational line in the IR spectra of He solvated CO₂ [27].

The main theoretical tool that have been employed so far to study rotational spectra of He solvated molecules is the dipole-dipole imaginary-time CF $\mathcal{C}_{\hat{n}}(\tau)$, Eq. (2.16), (as well as CFs of higher multipoles, Eq. (2.18)), whose ILT displays peaks in correspondence to dipole-allowed electromagnetic tran-

¹Throughout this Chapter, whenever we refer to He we mean ^4He .

sitions $J = 1 \leftarrow 0$ and whose strengths are proportional to the transition matrix elements between the ground and the excited states (see Sec. 2.3). Imaginary-time CFs are easily accessible to RQMC simulations without any other systematic biases than those due to the use of a finite time step and propagation time (see Sec. 2.4). The effect of the residual interactions between the effective rotor and the rest of the host is that the spectrum extracted from $\mathcal{C}_{\hat{n}}(\tau)$ CF is not entirely exhausted by the renormalized $J = 1$ molecular rotation, indicating in this way the presence of additional, weaker spectral features, higher in energy. The strength of these additional features, however, may be so weak as to make them hardly detectable through the numerically unstable ILT operation.

Our objective in this Chapter is to show how the use of generalized, symmetry-adapted, imaginary-time CFs allows us to selectively enhance the weight of faint spectral features, thus making them accessible to the ILT analysis. These CFs have the additional advantage of providing qualitative insight into the nature of different lines. As a demonstration of the usefulness of this approach, we employ it to study CO-He binary complex, a benchmark case for which exact-diagonalization results are available. Then, we use our generalized CFs to dwell upon the causes that lead to the line splittings experimentally observed in the spectra of $\text{CO}@He_N$, at cluster sizes $N \approx 7$ and $N = 15$ (see the left panel of Fig. 3.13). Our results, when compared with size-selective IR spectra of different CO isotopomers [26], that we have discussed in the previous Chapter, help to discriminate between alternative assignments of experimental lines proposed for cluster sizes around $N \approx 15$. Finally, we study the satellite band recently observed in the IR spectrum of CO_2 molecule solvated in He nanodroplets and discuss its proposed assignment to a coupled rotational state of the molecule and a ring of exchanging He atoms [27].

4.1 Theory

The optical spectrum of doped He clusters is obtained (Sec. 2.3) from the ILT of molecular dipole-dipole imaginary-time CF, that in the case of a linear

molecule coincides with autocorrelations of the unit vector $\hat{\mathbf{n}}$ along its axis:

$$\mathcal{C}_{\hat{\mathbf{n}}}(\tau) = \langle \hat{\mathbf{n}}(\tau) \cdot \hat{\mathbf{n}}(0) \rangle_0 = \sum_i |\langle \Psi_i | \hat{\mathbf{n}} | \Psi_0 \rangle|^2 e^{-(E_i - E_0)\tau}. \quad (4.1)$$

This procedure yields reliable results when the spectrum is exhausted by a few, well separated lines, that is often the case in rotational spectra of He solvated molecules.

Previous studies [24] have shown the usefulness of generalizing such CFs to gain insight into particular spectral lines. In the specific case of the *a*-type and *b*-type series of lines in CO@He_N clusters (see Fig. 3.13), the analysis of the imaginary-time CF of the unit vector $\hat{\mathbf{u}}$, pointing from the molecular to the He center of mass, $\mathcal{C}_{\hat{\mathbf{u}}}(\tau) = \langle \hat{\mathbf{u}}(\tau) \cdot \hat{\mathbf{u}}(0) \rangle$, has revealed that the *a*-type mode starts with a strong *end-over-end character*—a result that is well known in the case of the binary complex [61, 62]—and then gradually acquires both relative intensity and *free-rotor character*, heading toward the nanodroplet limit [24]. The *oscillator strengths* extracted from the spectral decomposition of $\mathcal{C}_{\hat{\mathbf{u}}}(\tau)$ CF can be taken as a measure of the *end-over-end character* of the excited states with total angular momentum $J = 1$, whereas a similar analysis of $\mathcal{C}_{\hat{\mathbf{n}}}(\tau)$ CF gives information about the *free-rotor character* of the $J = 1$ states. For instance, the *a*-type mode of the binary complex is a mixed end-over-end and free-rotor state, because its oscillator strength is sizable in both $\mathcal{C}_{\hat{\mathbf{n}}}(\tau)$ and $\mathcal{C}_{\hat{\mathbf{u}}}(\tau)$ CFs [24]. Furthermore, we can deduce that the character of this excitation is mainly end-over-end, because this state carries nearly all of the spectral weight in $\mathcal{C}_{\hat{\mathbf{u}}}(\tau)$, but only $\approx 10\%$ in $\mathcal{C}_{\hat{\mathbf{n}}}(\tau)$. Thus we see that the energy of this state can be located from the analysis of either CF. The above example shows the potential richness of suitably defined CFs for a deeper understanding and/or (as we will see in the following) a more efficient calculation of specific spectral properties. This motivates us to define a larger set of probe operators, that is to develop the methodology of extracting rotational excitations from unconventional imaginary-time CFs.

We restrict ourselves to the $J = 1$ portion of the spectrum and omit the index J whenever this does not lead to ambiguity. The total angular momentum of a doped He cluster can be decomposed as $\hat{\mathbf{J}} = \hat{\mathbf{j}} + \hat{\mathbf{\ell}}$, where $\hat{\mathbf{j}}$ is the molecular angular momentum and $\hat{\mathbf{\ell}}$ is the angular momentum of the atomic He shell. We note that only the total angular momentum is con-

served, whereas the angular momentum of the molecule and the sum of the atomic angular momenta are not, due to the anisotropic interaction between molecule and He. Thus the eigenstates of the Hamiltonian, which can be chosen as eigenstates of the total angular momentum, can be formally expanded into sums of products of eigenstates of the molecular angular momentum, $\phi_{jm_j}^X$, and of the atomic angular momentum, $\phi_{\ell m_\ell}^{\text{He}}$:

$$\Psi_{JM} = \sum_{j,m_j,\ell,m_\ell} \phi_{jm_j}^X \otimes \phi_{\ell m_\ell}^{\text{He}} \langle jm_j, \ell m_\ell | JM \rangle, \quad (4.2)$$

where $\langle \ell m_\ell, jm_j | JM \rangle$ are Clebsch-Gordan coefficients (CGCs). Since the total angular momentum of the cluster in the ground state is $J = 0$, the only CGCs giving a non-vanishing contribution are those with $j = \ell$ and $m_j = -m_\ell$, namely $\langle \ell m_\ell, \ell - m_\ell | 00 \rangle$. Likewise, states with $J = 1$, that are the only ones allowed to be optically excited from $J = 0$ (see Eq. (2.17)), will contain only the terms with $|\ell - 1| \leq j \leq \ell + 1$, since otherwise CGCs in Eq. (4.2) are equal to zero. The optically excited states can be coupled to the cluster ground state through an irreducible tensor operator of rank $J = 1$. Irreducible tensor operators can be decomposed into sums of tensor products of operators acting on the molecular and atomic components of the Hilbert space of cluster states, analogously to the decomposition of states themselves, Eq. (4.2):

$$\mathcal{T}_{JM} = \sum_{j,m_j,\ell,m_\ell} t_{jm_j}^X \otimes t_{\ell m_\ell}^{\text{He}} \langle jm_j, \ell m_\ell | JM \rangle, \quad (4.3)$$

where $t^{X(\text{He})}$ are irreducible tensor operators acting on the molecular (atomic) components of the cluster Hilbert space. Among many different possibilities for the $t^{X(\text{He})}$ operators, we choose diagonal operators in the coordinate representation², such as: $t_{jm_j}^X(\hat{\mathbf{n}}) = Y_{jm_j}(\hat{\mathbf{n}})$ and $t_{\ell m_\ell}^{\text{He}}(\hat{\mathbf{r}}_i) = \frac{1}{N} \sum_i Y_{\ell m_\ell}(\hat{\mathbf{r}}_i)$, where $\hat{\mathbf{r}}_i$ are the unit vectors along the relative X-He position³ and Y 's are spherical harmonics. Note that the $\phi_{00}^{\text{He}} \otimes \phi_{00}^X$ component of the ground state is coupled to the $\phi_{\ell m_\ell}^{\text{He}} \otimes \phi_{jm_j}^X$ component of an optically allowed excited state by the

²This choice is convenient, since RQMC method is formulated in the coordinate representation.

³The sharp shell structure of He atoms around a molecule justifies our choice.

$\mathcal{T}_{1M}^{j\ell}$ component in the expansion of Eq. (4.3), defined as:

$$\mathcal{T}_{1M}^{j\ell} = \sum_{m_j, m_\ell} Y_{jm_j}^X(\hat{\mathbf{n}}) t_{\ell m_\ell}^{He}(\mathbf{r}_i) \langle jm_j, \ell m_\ell | 1M \rangle. \quad (4.4)$$

Finally, we define symmetry-adapted, imaginary-time correlation functions (SAITCFs) as:

$$\mathcal{C}_{j\ell}(\tau) = \left\langle \sum_{M=-1}^1 \mathcal{T}_{1M}^{j\ell*}(\tau) \mathcal{T}_{1M}^{j\ell}(0) \right\rangle_0. \quad (4.5)$$

The idea of using different coupling operators to probe different excited states is not new. In the Projector Operator Imaginary Time Spectral Evolution (POITSE) approach [63], for instance, it has been used to separate rotations and vibrations of a model X-He binary complex; presumably due to technical limitations, however, this idea has not been pursued in a systematic way for larger systems. We believe that application of these ideas to the much more powerful and numerically stable RQMC framework will open the way to a much better understanding of weak spectral features in doped He clusters and nanodroplets. An alternative strategy would be the explicit construction of accurate wave functions for excited states. This exceedingly difficult task can yield good results in particular cases, but it is unlikely to be a viable approach in general. For example, remarkable results have been recently obtained [64] for the nodal structure of rotational states in very small clusters, but the extension to large systems is not straightforward and seemingly requires some *ad hoc* processing.

4.2 CO-He dimer

Our first application is a test against known results, namely the rotational spectrum of the CO-He dimer, as described by the SAPT potential energy surface in Refs. [40, 65], where the full spectrum was calculated exactly by a converged variational calculation. The CO-He potential energy surface supports four bound states with $J = 1$, which can be classified with the molecule and He angular momenta quantum numbers, j and ℓ , respectively. Although separately they are not good quantum numbers in general, in this particular case weak van der Waals interaction that holds the dimer results

in that the dominant (j, ℓ) contribution in each of these bound states is about 90%.

The CO-He dimer ground state together with its four bound rotational states having $J = 1$ are illustrated in Fig. 4.1. At the low cluster temperature ~ 0.4 K, only the lowest rotational level with $J = 0$ and positive parity is significantly populated. Upon the absorption of a MW (or IR) photon⁴, the dimer is in principle allowed to undergo one of the three rotational (or roto-vibrational) transitions indicated by arrows in Fig. 4.1. Namely, the negative parity of the photon of electromagnetic radiation imposes the restriction that only transitions to negative parity levels are allowed. The two transitions indicated in by solid line arrows in Fig. 4.1 are the b -type $(0, 0) \rightarrow (1, 0)$ and a -type $(0, 0) \rightarrow (0, 1)$ transitions whose relative intensities are standing in the proportion 7 : 1, while the third transition corresponding to $(0, 0) \rightarrow (1, 2)$, although in principle allowed, happens to be too weak to be observed, and it is thus indicated with the dashed line arrow in Fig. 4.1. Its intensity is estimated to be five times weaker than the a -type line [25]. The fact that the strongest of all these three dipole-allowed transitions corresponds to the b -type mode, that is $(j, \ell) = (1, 0)$, is due to the fact that it corresponds to the excitation of a molecular dipole in otherwise non-polar He environment. The exact calculation and the RQMC results are listed in Tab. 4.1. The simulation should also give unbiased results, and indeed we observe only one small discrepancy in the energy of the $(1, 0)$ state, presumably due to the ILT. In particular, the $(1, 0)$ state is the second lowest in the $\mathcal{C}_{10}(\tau)$ CF, that further contains higher excitations; this is a rather complex situation, and we consider the agreement quite gratifying. We stress that the “standard” dipole-dipole CF $\mathcal{C}_{\mathbf{n}}(\tau)$, that coincides with $\mathcal{C}_{10}(\tau)$, would only give the energies of the $(1, 0)$ and $(0, 1)$ bound states [24]. Using more CFs, instead, we can resolve all four bound states. Of course, spectral features that are weak or even missing in a particular CF are not necessarily so in a different one. As we already know from Ref. [24], the energy of the a -type $(0, 1)$ state can be extracted not only from \mathcal{C}_{10} (which gives in the

⁴In both MW and IR experiments the energies of the effective rotational constants are basically identical, since their dependence on the molecular vibrational quantum number ν is negligible.

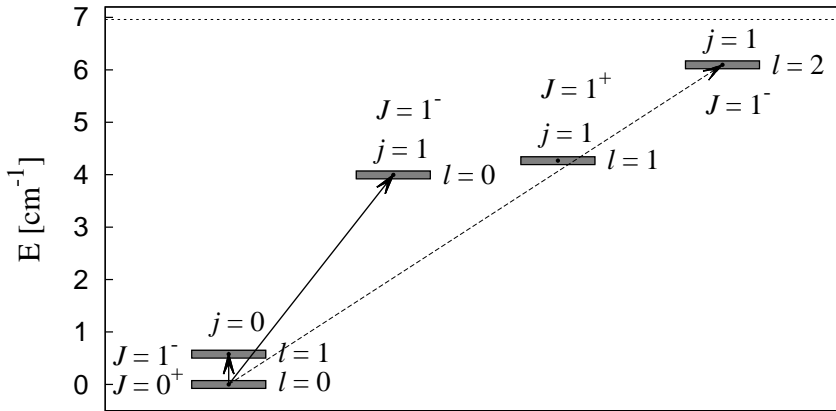


Figure 4.1: An illustration of the CO-He ground state along with its four bound $J = 1$ rotational states. The states are labeled with the corresponding j and ℓ values; their parities are also indicated. Arrows mark the only three rotational transitions that can originate from the ground state of the dimer; the horizontal dashed line is the CO-He dissociation limit.

present simulation $0.58 \pm 0.02 \text{ cm}^{-1}$), but also—with much higher precision—from \mathcal{C}_{01} (see Tab. 4.1). Using our new SAITCFs, we further see that the end-over-end mode $(0, 1)$ is present also in \mathcal{C}_{12} , with an estimated energy of $0.612 \pm 0.014 \text{ cm}^{-1}$. The \mathcal{C}_{11} CF, instead, remains on its own, despite the closeness of the energy of its dominant contribution, $(1, 1)$, with the free-rotor mode. This is due to the even parity of the $(1, 1)$ state, different from all the other bound states. This is an explicit example of increased efficiency in calculating particular states. In the following, we apply the formalism to the less academic cases.

4.3 Line splittings and assignments in $\text{CO}@^4\text{He}_N$ clusters

As we have anticipated, the doubling of the rotational lines at $N \approx 7$ in the b -type series⁵ and at $N = 15$ in the a -type series, is observed in the spectra

⁵For the normal CO isotopomer, the doubling of the b -type line occurs exactly at $N = 7$, however, for other isotopomers the splitting are observed in the range $N = 4 - 7$,

	(0,1)		(1,0)		(1,1)		(1,2)	
	E	A	E	A	E	A	E	A
\mathcal{C}_{01}	0.5810(8)	0.969(2)					8.0(6)	0.0171(7)
\mathcal{C}_{10}	0.58(2)	0.119(4)	4.09(3)	0.861(4)				
\mathcal{C}_{11}					4.322(13)	0.974(3)		
\mathcal{C}_{12}	0.612(14)	0.113(2)					6.07(6)	0.810(8)
exact	0.5817	0.9126	4.0175	0.9002	4.3079	0.9807	6.1049	0.8308

Table 4.1: The RQMC energies, E , (in cm^{-1}) and spectral weights, A , of each of the four bound states of the CO-He dimer, labeled (j, ℓ) as obtained from the $\mathcal{C}_{j\ell}$ CF. For the empty entries, the spectral weight is either zero or too small to be detected. The last row lists the exact results of Refs. [40] and [65]. Note that A has a different meaning for the exact calculation and for RQMC: in the former case it is the contribution of the dominant (j, ℓ) component in the exact eigenstate; in the latter, it is the weight of that particular (j, ℓ) eigenstate in the spectral decomposition of $\mathcal{C}_{j\ell}$ CF.

of small CO@He $_N$ clusters [25] (see the left panel of Fig. 3.13 and the experimental data indicated by crosses). RQMC calculations of Ref. [24] suggested that the feature at $N = 15$ is the consequence of the resonant coupling between the a -type excitation that at this cluster size fully regains its free-rotor character and the He-related mode coming from the analysis of $\mathcal{C}_{\hat{u}}(\tau)$ CF. In this way a resonant interaction between the two modes is proposed to lead to the observed line splitting, invoking the mixing of the “dark” He states otherwise invisible in IR experiments with the “free” molecular mode. These results are also reproduced with our SAITCFs approach and we see from the left panel of Fig. 4.2 that the He related excitation extracted from end-over-end \mathcal{C}_{01} CF (indicated by stars) coincides with a -type line (open circles) for $N = 15$. The right panel of the same Figure indicates that a -type line acquires its free-rotor character for $N > 10$. On the other side, the end-over-end mode keeps its character over the whole size range studied, while the drops in its strength at $N = 10$ and 15 reflect its mixing with the molecular mode.

see Fig. A.1 in Appendix A.

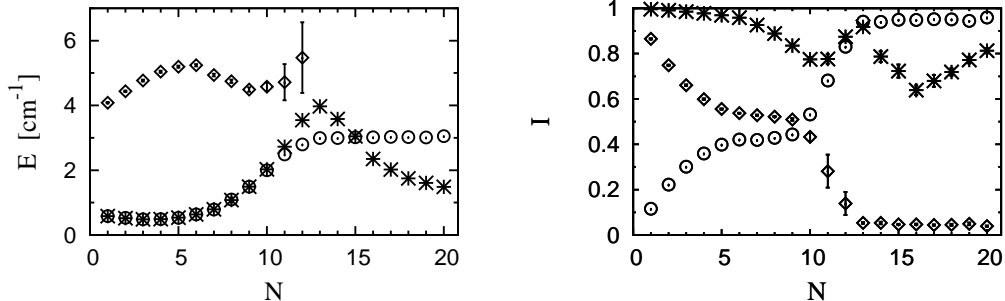


Figure 4.2: Left panel: Rotational excitations in $\text{CO}@^4\text{He}_N$ clusters extracted from \mathcal{C}_{10} CF, a -type transitions (open circles) and b -type transitions (open diamonds), and from \mathcal{C}_{01} CF (stars). Right panel: spectral weights of the corresponding excitations.

It is tempting to assume that a similar explanation could be offered for the R(0) line splitting at $N \approx 7$ for the b -type mode. To this end we have studied the evolution of all four bound rotational states of CO-He dimer with the number of He atoms, up to $N = 20$. Our results are displayed in Fig. 4.3. We see that the difference between the energies of (1, 0), (1, 1) and (1, 2) states is smallest for $N \approx 5 - 6$, close to the cluster size where the splitting is observed. There is an intriguing possibility that the mixing of these states could explain the b -type line doubling at $N \approx 7$ [25], although more precise statements are not warranted by the data.

A more quantitative conclusion comes, instead, from a deeper analysis of the splitting at $N = 15$. In this case, RQMC calculations help to distinguish among the different experimental assignments of R(0) lines of $\text{CO}@^4\text{He}_N$ clusters suggested in Ref. [26]. Namely, apart from the “conventional numbering” (the assignment as consistent as possible with that of Ref. [25]), alternative numberings of the experimental lines named A, B, C, and D in the size range around $N = 15$ are proposed in Ref. [26], after the measurements of other isotopomers, since none of them could be excluded on purely experimental grounds.

Fig. 4.4 shows our results for the isotopic dependence of the a -type series for the $^{13}\text{C}^{18}\text{O}$ isotopomer⁶. The convenient representation of the isotopic

⁶For the complete list of rotational energies for all CO isotopomers see Tab. A.1 in

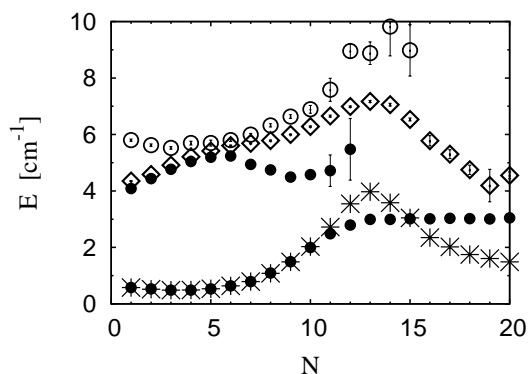


Figure 4.3: Evolution of the four bound rotational states of the CO-He dimer with the number of He atoms N : size dependent (1,0) state-filled circles, (0,1)-stars, (1,1)-open diamonds and (1,2)-open circles.

effect on the rotational excitations in $\text{CO}@He_N$ clusters is obtained by subtracting from the energy of $R(0)$ transition of given isotopomer the value measured for the normal $^{12}\text{C}^{16}\text{O}$ isotopomer. In this way, negative values are generally obtained, due to increased reduced masses of $^{13}\text{C}^{16}\text{O}$, $^{12}\text{C}^{18}\text{O}$ and $^{13}\text{C}^{18}\text{O}$, with respect to $^{12}\text{C}^{16}\text{O}$.

We see that the isotopic differences of the a -type lines start with negligible discrepancy among the isotopomers, corresponding to the initial end-over-end character of the series. Around the cluster size of about a dozen of He atoms, where the b -type series disappears and a -type lines acquire a free-rotor character, the difference increases, getting very close to its nanodroplet value already at $N = 20$. However, the magnitude of the difference shows a pronounced dip precisely at $N = 15$ in the conventional numbering. If one accepts the view that the line splitting at $N = 15$ is due to a near degeneracy with the He related excitation [24] (see as well Figs. 4.2 and 4.3), this dip would merely reflect the increased mixing of solvent states in the cluster rotational state. With any of the alternative numberings, either member of the former $N = 15$ doublet of the conventional numbering is paired to a different line with a stronger spectral weight and stronger isotopic dependence. In the weighted average⁷ such a strong isotopic dependence

Appendix A.

⁷After Fig. 2 in Ref. [26] (top trace) we have used weights in the ratios 87:125:17:36:50

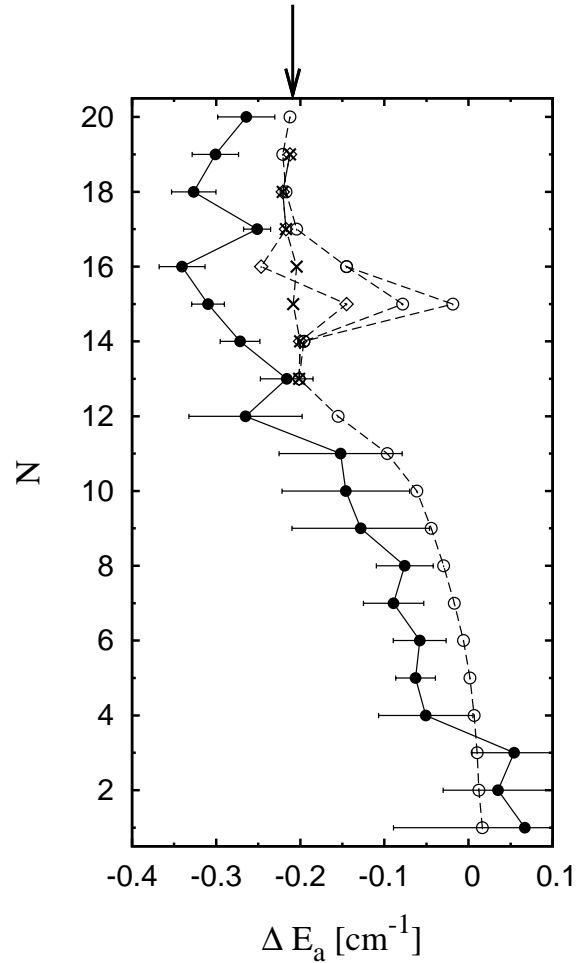


Figure 4.4: Difference between the energies of a -type mode of $R(0)$ transitions in $^{13}C^{18}O@He_N$ and $^{12}C^{16}O@He_N$ clusters: RQMC using CBS+corr potential (filled circles) and experiment [26] with the conventional (open circles), B (open diamonds), and D (crosses) numberings. For B and D numbering we have used weighted average of split lines (see in the text). Experimental energy difference is obtained after subtracting respective monomer band origin in the gas-phase. The arrow indicates isotopic effect in He nanodroplets [23].

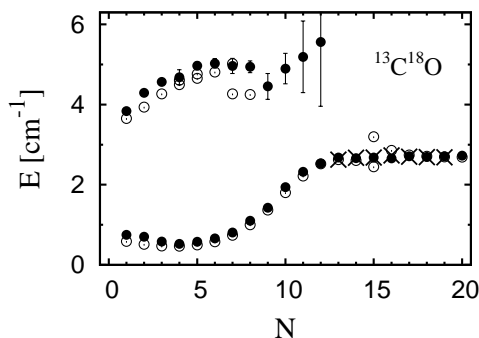


Figure 4.5: Rotational energies of $^{13}\text{C}^{18}\text{O}@\text{He}_N$ clusters: RQMC calculations (filled circles) and experiment [26] (open circles, conventional numbering; crosses, weighted average of the line positions with the D numbering). The experimental values are obtained from the measured R(0) line by subtracting the origin of the band in the gas-phase and the calculated vibrational shift.

prevails and the dip in the difference weakens (for numberings A and B) or disappears (C and D). Our calculations of the isotopic effect are in a good agreement with the experiment, although we generally find a slight overestimate of this effect presumably due to the simplified treatment of the change in the CO-He potential⁸, mentioned in Sec. 3.3. We note in particular the absence of the dip at $N = 15$ or $N = 16$. If one considers weighted averages for the line doublets at given cluster size, this is consistent with numberings C, D but not with A, B or conventional⁹. The simulation results with CBS+corr potential (Fig. 4.4) show instead a possible dip at $N = 17$ for $^{13}\text{C}^{18}\text{O}$. However, this feature, not seen in the experimental data with any of the proposed numberings, is rather weak and gets lost into the statistical error for other isotopomers (see Tab. A.1 in Appendix A). Finally, our simulations support D assignment of experimental lines, for which both

for the lines assigned to 13, 14, 15a, 15b and 16, respectively, in the conventional numbering.

⁸In our calculations we employ adiabatic approximation, *i.e.* we use CO-He potential averaged over the period of molecular vibration. This implies that a small effect on the potential coming from the change in the vibrational ground state of the molecule upon isotopic substitution is neglected.

⁹The C and D experimental assignments differ only at $N = 13$, where D numbering better fits our data.

the absence of the dip in Fig. 4.4 and an excellent agreement between the calculated and experimental a -type rotational energies is obtained around $N \approx 15$ for $^{13}\text{C}^{18}\text{O}$ isotopomer (see Fig. 4.5), under the assumption that other sources of bias (such as imperfections of the potential energy surface, or the possible uncertainty related to the number of terms used to fit the imaginary-time CFs [24]) have a sufficiently smooth dependence on N .

4.4 Satellite band in $\text{CO}_2@^4\text{He}_N$ clusters

We now address the problem of the characterization of a weak spectral feature recently observed in the IR spectrum of CO_2 solvated in He nanodroplets [27] by applying the methodology of SAITCFs. Experimentally, a weak satellite band (SB) found to accompany the $\text{R}(0)$ roto-vibrational line carries $\approx 4\%$ of the spectral weight and it has an energy $E \approx 20$ K. Theoretically, the presence of such a weak satellite band, higher in energy, in the spectra of He-solvated molecules is not a surprise. The high precision afforded by RQMC [8], allows one to clearly detect more $J = 1$ rotational states on top of the dominant free-rotor-like excitation which originates the $\text{R}(0)$ transition.

Analysis of the $\mathcal{C}_{\hat{n}}$ CF [10] indeed shows that the second lowest excitation energy is about 20K with a spectral weight of a few percent, in agreement with the experiment. The study of the nature of the SB, on the other hand, is intriguing. Because its energy is above the bulk He roton gap, the effective rotor is expected to couple to localized states, rather than to the collective bulk-like excitations [66]. Helium related vibrational modes in the first solvation shell arise as the first natural candidates for this coupling. However, it has been suggested [27] that a key role in explaining the nature of the satellite band could be played by the coupled rotational excitations of the molecule and an azimuthal ring of He atoms in the first solvation shell.

4.4.1 The ring model

The ring model is a highly simplified model of two coupled planar rotors, representing a molecule and an azimuthal ring of N He atoms. It is exactly numerically solvable and it was shown in Refs. [45, 67] to reproduce the

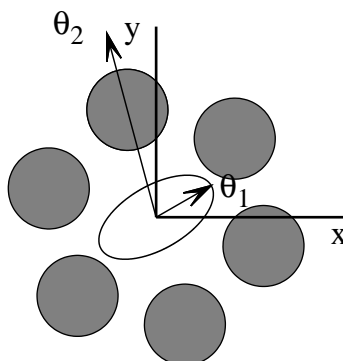


Figure 4.6: Illustration of the basic elements in the ring model: gray circles represent ^4He atoms, while the ellipse represents the linear molecule. Rotations occur in the $x - y$ plane, and the angular coordinates of the molecule and the He ring are θ_1 and θ_2 , respectively.

order of magnitude of the experimentally observed effective rotational and centrifugal distortion constants of He-solvated molecules.

A linear molecule is treated as a rigid planar rotor with a moment of inertia I_1 . Its orientation is given by a rotational coordinate θ_1 , while the portion of the relevant He environment is represented by a ring of N He atoms, that forms a rigid planar rotor characterized by a moment of inertia I_2 and a rotational coordinate θ_2 . The ring model is illustrated in Fig. 4.6. The Hamiltonian of the system is given by $\hat{H} = \hat{j}^2/2I_1 + \hat{\ell}^2/2I_2 + V \cos(N(\theta_1 - \theta_2))$. Due to indistinguishability of He atoms the wave function $\psi_{\text{ring}} \sim \exp(iL_2\theta_2/\hbar)$ must stay unchanged upon rotation of the ring as a whole by an angle $\Delta\theta_2 = 2\pi/N$, that constrains the allowed values of the angular momentum of the ring to be:

$$\ell = m \times N\hbar \quad m = 0, \pm 1, \pm 2, \dots \quad (4.6)$$

In this way the Bose symmetry requires that the ring can only have rotational excitations with angular momentum ℓ in multiples of $N\hbar$. The removal of states in the spectrum of the ring leads to the restriction on the values of the angular momentum j of the molecule, in order to form a coupled rotational state with the total angular momentum $J = j + \ell$. In this way the wave function of the lowest energy state with total angular momentum J has a

predominant contribution from the basis state $|j = J\rangle \times |\ell = 0\rangle$, while for the first excited state the largest contribution comes from the state of the type $|j = J \pm N\rangle \times |\ell = \mp N\rangle$, corresponding to the first excited state of the He ring and high rotational excitation of the molecule. According to the ring model, the main feature in the spectra of a He-solvated molecule has the rotational characteristics of a bare molecule, since it is a transition from the ground state $J = 0$ to the lowest state with $J = 1$. The SB corresponds to the transition from the ground state $J = 0$ to the first excited state having $J = 1$, and it is symmetry-constrained to have a relatively high energy. We thus see that the ring model suggests the interpretation that the renormalization of the molecular rotational constant and occurrence of the side bands are a closely related phenomena. With a value of N of about 6 or 7 adequate to the spatial extent of the first solvation shell of CO_2 , the model yields excitation energies comparable to the measured SB [27].

4.4.2 Results and discussion

We will now apply the SAITCF approach in order to test this ring model in $\text{CO}_2@^4\text{He}_N$ clusters. We have already mentioned that we do find a $(1, 0)$ state with an energy of $\sim 20\text{K}$ and a spectral weight of a few percent. If the ring model is indeed relevant to the SB, we would expect at least one state, with He angular momentum ℓ in the range 5 to 8 [27] and significant spectral weight, degenerate with the SB. Furthermore, we would not expect many such states outside this j range; this is not strictly necessary (see the caption of Tab. 4.1 for the meaning of the spectral weight in the SAITCF approach), but it would be strongly suggestive. Finally, we would expect all the above to be significantly size-dependent in the small cluster regime, because there have to be enough He atoms to build the azimuthal ring. The excitation energies of $\text{CO}_2@^4\text{He}_N$ clusters with total angular momentum $J = 1$, extracted from $\mathcal{C}_{j\ell}$ are shown in Fig. 4.7 for $N = 20$ and in Fig. 4.9 for $N = 5$. The first five He atoms form a highly localized equatorial “donut” in the minimum of the CO_2 -He potential, whereas $N = 20$ corresponds to one full solvation shell around the molecule [10]. Let us consider the $N = 20$ case first. The value $(j = 1, \ell = 0)$ corresponds to the standard correlation

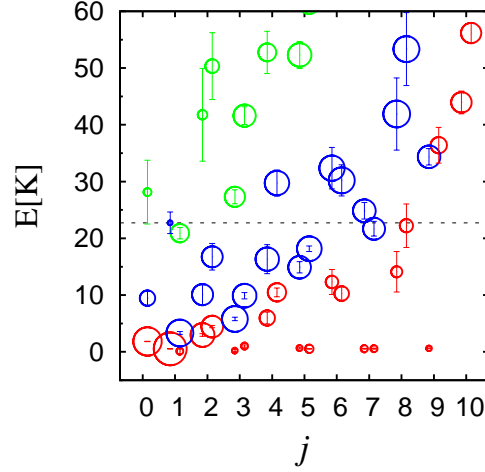


Figure 4.7: Excitation energies of $\text{CO}_2@\text{He}_{20}$ cluster extracted from the CFs $\mathcal{C}_{j\ell}$ as a function of j . The total angular momentum is $J = 1$, and $\ell = j \pm 1$. For clarity, the $\ell = j \pm 1$ data have been slightly right/left shifted. Each energy is represented by a circle whose area is proportional to its spectral weight. For each (j, ℓ) , the spectral weights of the vertically stacked energies (red, blue and green from lowest to highest) add to one. A horizontal dashed line is drawn at the energy of the satellite band evaluated from the dipole-dipole correlation function.

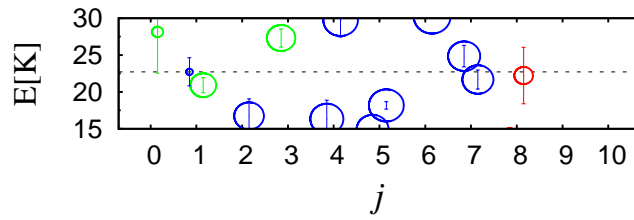


Figure 4.8: Excitation energies of $\text{CO}_2@\text{He}_{20}$ cluster, same as in Fig. 4.7 but in the energy region in the vicinity of the satellite band.

function used in previous work [10] (the data reported here, however, all come from a new simulation, in which all the CFs were obtained at once). The big circle (down to the x axis on the scale of the figure) is the familiar free-rotor state, and the little circle at $E \approx 20K$ with a much larger error bar is the satellite band. Now we sweep the j range looking for more states at a nearby value of E . Generally speaking, there are vestiges of the $E \sim j^2$ behaviour which in the ring model places the right energy at the right j value, *i.e.* only few states of the type $|j = 1 \pm N, \ell = \mp N\rangle$ are contributing to the first excited state of this rotationally coupled system. This means that we expect really few (at most one or two) rotational excitations in the vicinity of SB if the ring model is relevant. Indeed, the Fig. 4.8 contains few excitations having the energy of the SB (see also Fig. 4.8 that emphasizes this energy region). More in detail, there are two “good” states with significant weight at $j = 7$, a value supportive of the ring model, and a further state at $j = 8$, but with smaller weight and larger uncertainty. There is also a contribution from $(1, 2)$, but overall the picture is at least consistent with the presence of high- j rotational excitations in the satellite band. The rest of the figure encodes much interesting information. For instance, there is plenty of $J = 1$ rotational excitations, but most of them do not contribute to the experimentally observed spectrum.

For $N = 5$, there is definitely not enough He atoms to build up azimuthal ring around the molecule, because all the He atoms are rather tightly bound to the equatorial donut [10]. The Bose symmetry argument at the basis of the ring model, applied to the equatorial donut, can affect a Q-branch [55], but not the SB. Therefore, we simulated the $\text{CO}_2@^4\text{He}_5$ cluster to verify the size dependence of those aspects of the SB which are presumably related to high- j states (we do expect a SB anyway, since in general we never see a one-exponential decay in the CFs). Fig. 4.10, indeed, shows that the $N = 5$ SB is degenerate (within the rather large statistical uncertainty) with several states with different j , those at $j = 2$ having a particularly strong spectral weight (see also the lower panel of Fig. 4.10 for enlarged energy region around the SB); this would match the behaviour expected by the ring model. However, the SB is surprisingly still close to 20K. If it is not a coincidence (but calculations for $N = 10$ seem to exclude this possibility—there is a 20K

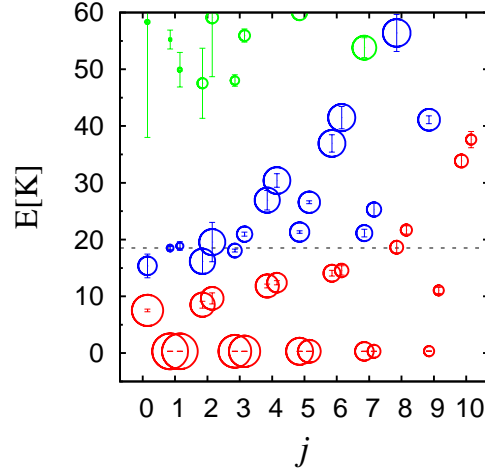


Figure 4.9: Same as in Fig. 4.7, but for $\text{CO}_2@\text{He}_5$ cluster.

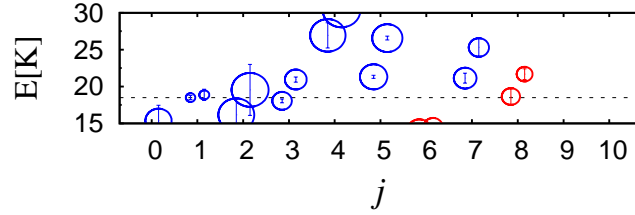


Figure 4.10: Same as in Fig. 4.8, but for $\text{CO}_2@\text{He}_5$ cluster.

SB there as well), it means that the value of the SB energy is not due to the $\sim j^2$ behaviour combined with restrictions from Bose symmetry, which is the cornerstone for its interpretation in terms of the ring model.

In summary, we find one result in favor of the ring model (namely, a clear high- j characterization of the SB only at cluster sizes when the He ring is fully established) and one result which could be seen as being against it (the independence of the SB energy on the cluster size, across a range where the ring itself disappears). A more systematic study of the N -dependence of the SB and a calculation of its variation with the moment of inertia of the dopant molecule will fully clarify this issue. However, the present results indicate that SAITCFs will be instrumental to such a clarification and that they hold indeed the promise of being powerful tools in the simulation of the spectra of systems of interacting bosons and in their physical interpretation.

Chapter 5

^3He clusters

The most prominent features of the NCRI of molecules solvated in bosonic ^4He clusters are the sharpness of the rotational lines and the turnaround of the effective rotational constants observed for the molecules such as OCS [5, 8, 9], CO_2 [10], N_2O [11] and HCCCN [12], that takes place in very small clusters consisting of less than 10 He atoms (see also Fig. 2). This turnaround is seen to be the consequence of enhanced particle exchanges that effectively lead to decoupling of ^4He atoms from the molecular rotation [8]. It would be interesting to explore in more detail the way the particle statistics influences the spectra of He-solvated molecules.

There has been a work that compares the results of ground state RQMC calculations for N_2O molecule solvated with ^4He atoms with finite temperature path-integral simulations obtained ignoring the effects of Bose statistics [11]. It appeared that in contrast to the Bose case (in which the turnaround of the effective rotational constant is observed), the effective rotational constant of the molecule solvated with distinguishable particles exhibits an almost monotonic decrease with the system size. Moreover, an accuracy of the fit of the system's energy spectrum to an effective rotor Hamiltonian is found to decrease with increasing the cluster size. This confirmed that the indistinguishability of particles and the scarcity of the spectrum of bosonic solvent at low temperature are crucial in leading to only a slightly perturbed free-rotor picture as well as to a NCRI.

The effect of particle exchanges on the spectrum of a molecule embedded in a quantum solvent is further addressed in a remarkable experiment of Grebenev *et al.* [28, 29]. In that experiment, the IR spectra of OCS solvated with para-hydrogen (p-H₂) and ortho-deuterium (o-D₂) molecules and coated inside mixed ³He/⁴He nanodroplets were observed. It was found that with $N = 5$ and 6 p-H₂ molecules around OCS, Q-branch—that contains the rotational excitations whose angular momenta lay along the axis of a linear molecule—disappears from the spectra. This was in contrast with the case when p-H₂ molecules were substituted with their o-D₂ counterparts, that resulted in the reappearing of an intense Q-branch. In the first case, the permutational symmetry of indistinguishable spinless p-H₂ bosons constrains the lowest rotational level of a doughnut ring around the molecular symmetry axis to have energy too high to be excited at a low cluster temperature. On the other side, o-D₂ molecules represent a distinguishable mixture of bosons with nuclear spin 0 and 2, so that there is no symmetry constraint in this case. This experiment illustrated the striking effect that particle exchanges impose on the spectra of solvated molecules.

We would like to extend the investigation of this interesting physical issue and to study the effect of Fermi statistics on the rotational spectra of molecules solvated in small fermionic ³He clusters, for which both theory and experiment do not exist to date. The difficulty is that current QMC methods for fermions are either approximate (if the so-called *fixed node* (FN) algorithm is used), otherwise, although in principle exact (when FN is not implemented), they are numerically unstable [35]. This situation is usually referred to under the term “fermion sign problem”. In this Chapter we present a new exact QMC approach for fermions and we name it antisymmetric SAITCF (A-SAITCF) method, which is valuable when the ground-state energy of a fermionic system is not too far from its bosonic ground state. Our method is based on a generalization of the SAITCF approach presented in Chapter 4, adapted to incorporate antisymmetry requirement inherent for fermionic systems. It is capable to access fermionic ground state, as well as fermionic excited states. Our method is stable, in a sense that the statistical error on the CFs scales as the inverse square root of the computer time (however, this does not imply that the same holds also for extracted energies).

The method is suitable for small systems, since it relies on the ILT procedure in order to extract fermionic excitations from imaginary-time correlations of suitably defined antisymmetric operators. Namely, we need the fermionic gap, that is the energy difference between the fermionic ground and the first excited state consistent with a given symmetry, to be large enough to be resolved by the ILT of a given imaginary-time CF and this is expected to hold for not too large systems.

We apply this approach on the rotational spectrum of CO_2 molecule embedded in small fermionic ^3He clusters. Our objective is to study the amount of NCRI present in these fermionic systems. We choose CO_2 because it exhibits a strikingly sharp manifestation of NCRI that arises at a very small cluster size (see Fig. 2 and note that the minimum of B_N is observed already at $N = 5$). As the first step towards exploring the effect of particle exchanges on the spectra of small doped ^3He clusters, we study the rotational dynamics of OCS molecule solvated in ^4He and in mixed $^3\text{He}/^4\text{He}$ clusters in the presence of a single or double ^3He impurity.

5.1 Small doped mixed $^3\text{He}/^4\text{He}$ clusters

It is qualitatively clear that substituting one ^4He atom with its fermionic ^3He counterpart in otherwise bosonic He cluster has as the effect to hinder bosonic particle exchanges. However, its quantitative effect on the molecular spectra is less obvious, especially in small clusters. In the large size limit, the effect of ^3He impurity is trivial, since lighter ^3He atoms tend to float on a droplet surface, having no influence whatsoever on the bosonic exchanges of ^4He atoms in the vicinity of the molecule. In the case of mixed clusters containing a single or double ^3He impurity, there is no need to impose fermionic antisymmetry into the computational scheme, since the two atoms can be chosen to have antiparallel spins and so, to be distinguishable. Thus we proceed with the calculation as in the bosonic case.

We investigate the rotational spectrum of OCS molecule solvated in pure ^4He , as well as in small mixed clusters in which one or two ^4He atoms are substituted with their fermionic analog ^3He , in the size range $N = 1 - 15$, N being the total number of He atoms. We choose this specific molecule be-

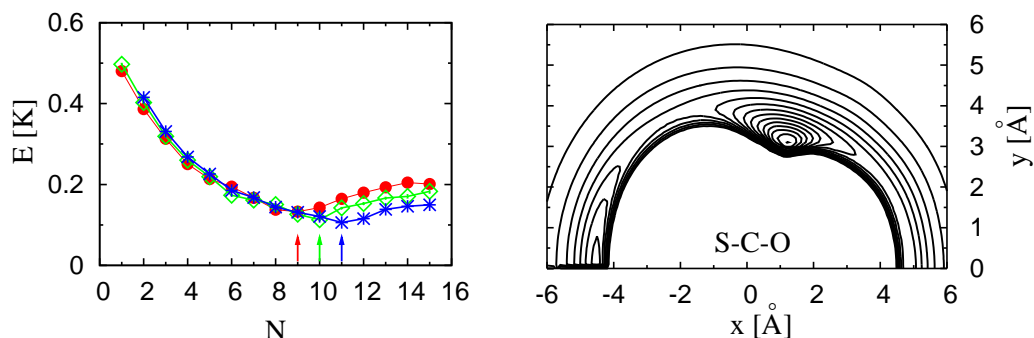


Figure 5.1: Left panel: dependence of the rotational energies on the total number of He atoms $N = N({}^3\text{He}) + N({}^4\text{He})$ in pure $\text{OCS}@{}^4\text{He}_N$ cluster (filled red circles), and in mixed $\text{OCS}@{}^4\text{He}_{N-1}{}^3\text{He}_1$ (open green diamonds) and $\text{OCS}@{}^4\text{He}_{N-2}{}^3\text{He}_2$ (blue stars) clusters. Right panel: OCS-He potential with contour levels that start from $V_\infty = 0$ to negative values and spacing between levels equal to 5 K.

cause of the particularly clear relationship that exists between the rotational spectrum and the structural properties induced by its strongly anisotropic interaction with He [8] (see the right panel of Fig. 5.1). The resulting rotational spectrum is displayed in the left panel of Fig. 5.1. We see that the turnaround is present also in the mixed clusters, although it sets in earliest and it is the most prominent in a pure ${}^4\text{He}$. Namely, the effect of hindering bosonic permutations in mixed clusters is to round-off the minimum of the rotational energy and to shift it towards larger cluster sizes. In order to rationalize the observed shift upon the addition of ${}^3\text{He}$ atoms, we will first analyze pure $\text{OCS}@{}^4\text{He}_N$ clusters.

The main potential well of OCS-He potential accommodates up to 5 ${}^4\text{He}$ atoms and leads to the formation of the doughnut ring of ${}^4\text{He}$ density in the plane perpendicular to the molecular axis (the position of the doughnut is indicated by the main peaks of He density in Fig. 5.2). For $N \leq 5$ the doughnut is constrained to rotate rather rigidly with the molecule [8] and each atom in the doughnut gives the same contribution to the cluster moment of inertia, that results in the nearly constant slope of the rotational excitations in the left panel of Fig. 5.1 for $N \leq 5$. When $N({}^4\text{He})$ is further increased, the ${}^4\text{He}$ - ${}^4\text{He}$ repulsion causes that the added atoms are moving towards secondary

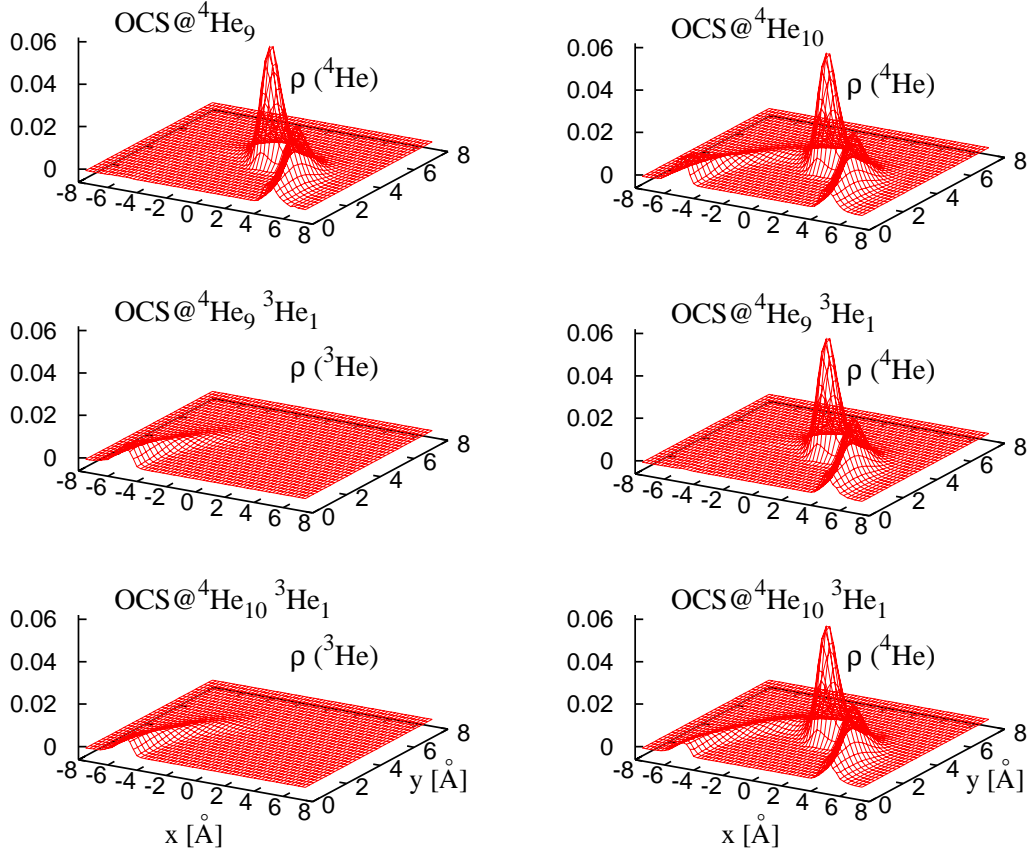


Figure 5.2: The ^4He and ^3He components of the total He density in the pure ^4He and in the mixed $^3\text{He}/^4\text{He}$ clusters doped with OCS. The molecule lays along x-axis, with oxygen atom pointing in its positive direction. The molecular center of mass coincides with the origin. Density profiles are expressed in units \AA^{-3} .

minima of the OCS-He potential that exist near the two molecular poles, the one in the vicinity of the sulphur atom being deeper (see the right panel of Fig. 5.1). However, we see from the right panel in the first row of Fig. 5.2 that ^4He density is larger near oxygen pole. This is because a smaller energy barrier and a smaller distance favor quantum tunneling [8]. Finally, for $N = 10$ also the potential well near the sulphur atom starts to fill. However, at this cluster size, we see that sizable ^4He density is found not only near molecular poles, but also in the angular region between the poles and the doughnut. This means that the sagittal ring of ^4He density in the plane

containing the molecule is being formed, as displayed in the right panel of the first row of Fig. 5.2. As it was revealed in Ref. [8], the closure of the ⁴He density makes particle exchanges along this ring possible (involving even atoms in the doughnut), leading to the effective decoupling of ⁴He atoms from the molecular rotation and the subsequent turnaround of the molecular effective rotational constant, after its minimum at $N = 9$ is reached (see the left panel of Fig. 5.1).

When in OCS@⁴He₁₀ we substitute one ⁴He atom with its lighter isotope ³He, the latter is the one that becomes expelled to the secondary minimum near the sulphur atom, due its lighter mass (see the second row of the Fig. 5.2). In this way the ³He atom hinders ⁴He exchanges by suppressing the formation of the bosonic ring in the sagittal plane and postponing its closure to cluster size with $N = 11$ total number of He atoms, as seen from the third row in Fig. 5.1. This explains the fact that the minima of the rotational energy of OCS@⁴He _{N} , OCS@⁴He _{$N-1$} ³He₁ and OCS@⁴He _{$N-2$} ³He₂ clusters are found at $N = 9$, $N = 10$ and $N = 11$, respectively.

What happens when the number of ³He atoms further increases is the question we would like to address. However, to do that we need fully fermionic calculation. Therefore we proceed by introducing a new QMC approach that will allow us to access fermionic rotational excitations in doped ³He clusters for $N \geq 3$.

5.2 Fermionic excitations

Let us first observe that the Hamiltonian $\hat{H} = -\frac{\hbar^2}{2m}\nabla_{\mathbf{R}}^2 + V(\mathbf{R})$ is symmetric with respect to particle exchanges and that it has the same form for Bose and Fermi systems, as well as for systems with mixed symmetry. However, the absolute ground state of the Hamiltonian \hat{H} is nodeless, *i.e.* the bosonic one. In this way the fermionic ground state can be seen as an excited state of a many-body Hamiltonian. Schematic illustration of Hamiltonian energy levels corresponding to states of different symmetries is shown in Fig. 5.3.

In order to filter out of all these excited states only those that have fermionic symmetry, we use the ideas presented in Subsec. 1.5.2. Since we are interested in the eigenstates having the total angular momentum J , we

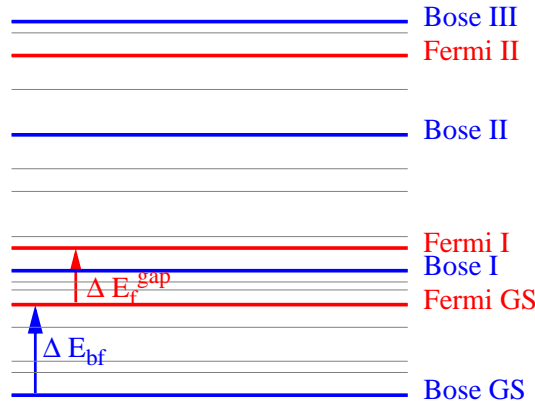


Figure 5.3: Schematic representation of the eigenstates of the Hamiltonian $\hat{H} = -\frac{\hbar^2}{2m}\nabla_{\mathbf{R}}^2 + V(\mathbf{R})$, that can be of any symmetry: Bose (blue lines), Fermi (red lines) or mixed (gray lines). Note that the absolute ground state is the bosonic one. Bose-Fermi ground state separation ΔE_{bf} and the fermionic gap ΔE_f^{gap} are indicated.

need to construct appropriate antisymmetric operators $\hat{\mathcal{A}}_J$, which have the same symmetry properties under rotations as the fermionic states we want to couple to. Then, the corresponding fermionic excitations are extracted by means of the imaginary-time autocorrelations of the operator $\hat{\mathcal{A}}_J$

$$\mathcal{C}_{\hat{\mathcal{A}}_J}(\tau) = \sum_{n'} |\langle \Psi_0 | \hat{\mathcal{A}}_J | \Psi_{n'} \rangle|^2 e^{-(E_{n'} - E_0^b)\tau} = \sum_n |\langle \Psi_0 | \hat{\mathcal{A}}_J | \Psi_{n,J}^f \rangle|^2 e^{-(E_{n,J}^f - E_0^b)\tau}, \quad (5.1)$$

where the first sum over n' is meant to contain contributions from all the excited states of \hat{H} . However, the operator $\hat{\mathcal{A}}_J$ projects out only fermionic states with angular momentum J , so that the second sum over n emphasizes that all non-vanishing terms are having this particular symmetry. More specifically, since $|\Psi_0\rangle$ is the bosonic ground state, it is symmetric with respect to permutation of identical particles and it is constrained to have $J = 0$. Thus the following selection rule holds

$$\langle \Psi_0 | \hat{\mathcal{A}}_J | \Psi_{n,J'}^f \rangle \neq 0 \quad \text{if} \quad \hat{\mathcal{P}} | \Psi_{n,J'}^f \rangle = (-1)^p | \Psi_{n,J'}^f \rangle \quad \text{and} \quad J' = J, \quad (5.2)$$

where $\hat{\mathcal{P}}$ is a permutation operator and p is the parity of a particle permutation.

We see from Eq. (5.1) that the imaginary-time CF $\mathcal{C}_{\hat{\mathcal{A}}_J}(\tau)$ has the contribution from different fermionic excited states of a given symmetry, namely, $\Psi_{0,J}^f, \Psi_{1,J}^f, \dots$, that correspond to the energies $E_{0,J}^f, E_{1,J}^f, \dots$. In order to resolve lowest between them using the ILT procedure, we need the first excited fermionic state $E_{1,J}^f$ to be well-separated from the fermionic ground state $E_{0,J}^f$ of the same symmetry. In other words, we need the fermionic gap $\Delta E_f^{gap} = E_{1,J}^f - E_{0,J}^f$ to be of at least the same order of magnitude as the Bose-Fermi ground state separation $\Delta E_{bf} = E_{0,J}^f - E_0^b$. The situation becomes more favorable in this respect if $\Delta E_f^{gap} > \Delta E_{bf}$ is fulfilled.

Since a characteristic gap in fermionic systems behaves typically as $\Delta E_f^{gap} \propto 1/N$ and the Bose-Fermi ground state separation ΔE_{bf} (as an extensive quantity) grows with the system size, we expect that the required criterion will hold for not too large systems. In the following we will apply our approach to the system of five ideal fermions in $2d$, in order to illustrate the method on a simple and analytically solvable model.

5.2.1 A toy problem

A toy problem consists of $N = 5$ non-interacting fermions of mass m confined in a square of side L , that are subjected to periodic boundary conditions. The eigenstates are plane waves whose wave vectors components are integer multiples of $2\pi/L$. The k -values corresponding to the ground and the two selected excited states are displayed in the left panel of Fig. 5.4. The energies of the eigenstates are of the form $E = \sum_{i=1}^N \frac{\hbar^2 k_i^2}{2m}$; the ground state and the two selected excited states are readily seen to have the energies $E_0^f = 2$, $E_1^f = 2.5$ and $E_2^f = 3.5$ (in the units $\hbar = m = 1$ and $2\pi/L = 1$), respectively.

In this ideal case the coordinate representation of the antisymmetric operator taken as the Slater determinant of plane waves $\hat{\mathcal{A}}_0 = \mathcal{D}_0(e^{-i\mathbf{k}\mathbf{r}})_{5 \times 5}$, with the set of k -vectors marked with red circles in the left panel of Fig. 5.4, coincides with exact ground state $|\Psi_0^f\rangle$ of the system. Noting that in this case the Bose ground state is zero, *i.e.* $E_0^b = 0$, the fermionic imaginary-time autocorrelation function given by Eq. (5.1) now has the form of the single exponential

$$\mathcal{C}_0(\tau) = |\langle \Psi_0^b | \mathcal{D}_0(e^{-i\mathbf{k}(\tau)\mathbf{r}(\tau)}) \mathcal{D}_0^*(e^{-i\mathbf{k}(0)\mathbf{r}(0)}) | \Psi_0^f \rangle|^2 e^{-E_0^f \tau}. \quad (5.3)$$

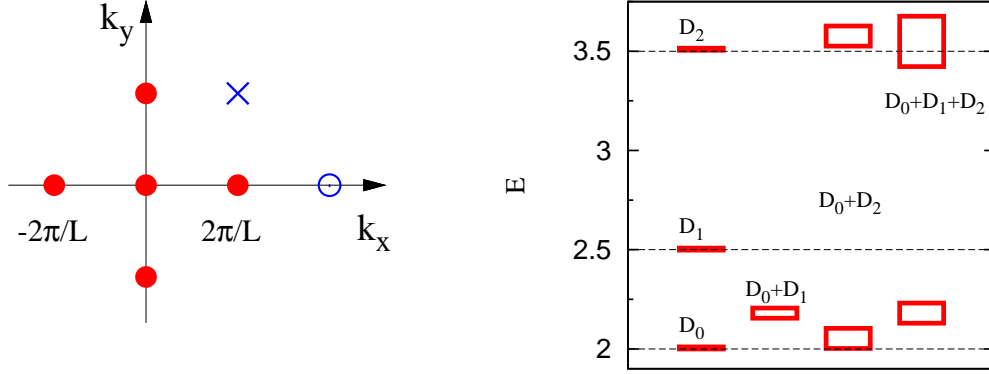


Figure 5.4: Left panel: the set of k -values corresponding to the ground state of the toy model $|\Psi_0^f\rangle$ (red circles); k -sets that describe two selected excited states $|\Psi_1^f\rangle$ and $|\Psi_2^f\rangle$ are obtained by replacing one of $k \neq 0$ values with the blue cross, or the empty circle, respectively. Right panel: fermionic energies coming from the imaginary-time correlations for different choices of $\hat{\mathcal{A}}$. Centers of the rectangles correspond to the energy values, while the half heights are statistical uncertainties with which they are determined. Horizontal dotted lines are the energy values E_0^f , E_1^f and E_2^f of the ground and two selected excited states.

From the first stack of the energy levels in the right panel of Fig. 5.4 we see that the single determinants (\mathcal{D}_0 , \mathcal{D}_1 and \mathcal{D}_2) are giving exact energies, since they coincide with the eigenstates $|\Psi_0^f\rangle$, $|\Psi_1^f\rangle$ and $|\Psi_2^f\rangle$, respectively.

The rest of the figure displays fermionic excitations extracted when some linear combinations of these determinants are employed. They happen to break translational symmetry of the system and the very fact that antisymmetric operators $\hat{\mathcal{A}}$ formed in this way do not coincide with any fermionic eigenstate $|\Psi_k^f\rangle$, mimics realistic situation when exact eigenstates are unknown. The resolution of the ILT procedure depends on the energy separation between the relevant energy levels and we note from the second stack that for the particular choice $\mathcal{A} = \mathcal{D}_0 + \mathcal{D}_1$ and a given amount of computer time, reconstructed spectrum does not seem to resolve between the E_0^f and E_1^f , since fermionic gap $\Delta E_f^{gap} = 0.5$ is in this case considerably smaller than the Bose-Fermi ground state separation $\Delta E_{bf} = 2$. The third stack, corresponding to the choice $\mathcal{A} = \mathcal{D}_0 + \mathcal{D}_2$ illustrates a more favorable situ-

ation, because the separation of fermionic excitations is significantly larger, so that the exact energies are reproduced within one statistical error. The reconstructed spectrum for the final choice $\mathcal{A} = \mathcal{D}_0 + \mathcal{D}_1 + \mathcal{D}_2$, displayed in the fourth stack of energy levels, embodies the features of the previous two cases: it does not seem to resolve between the two lowest excitations, however the highest one is well-reproduced. We see that for a given amount of the computer time, we are not guaranteed to resolve between relatively close fermionic states.

In the next Section we will apply our A-SAITCF approach to the realistic problem of rotational spectra in small doped fermionic clusters. We are aware that we will employ antisymmetric operators that are not the eigenstates of Hamiltonian. However, our goal is to distinguish only the lowest fermionic energy and we will do this with the further bonus of exploiting the symmetry.

5.3 Small doped ³He clusters

Before we introduce our methodology to access rotational excitations in small doped fermionic ³He clusters, we illustrate the viability of our approach by anticipating the results for the ground state energy per particle in the fermionic CO₂@³He_N clusters and their bosonic counterparts (*i.e.* the clusters made of bosonic atoms having the mass of ³He) that are displayed in Fig. 5.5.

The first thing we note is that Bose and Fermi energies are very similar, that justifies the bosonic sampling employed in RQMC for calculating fermionic properties. In addition, the small value of Bose-Fermi ground state separation indicates that in these systems the favorable conditions to employ the ILT to extract fermionic excitations are indeed met. Further, the similarity between bosonic and fermionic ground state energies, that is their apparent insensitivity to the change in the particle statistics—due to the hard-core repulsion that dominates the energy on this scale—reflects that structural similarities between Bose and Fermi doped CO₂ clusters can be expected. In particular, the shell structure of He density around the molecule, as well as the characteristic doughnut ring found for bosonic clusters [10], are expected to hold also in the fermionic case.

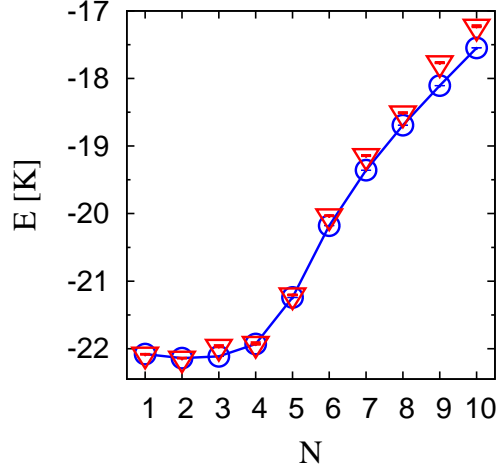


Figure 5.5: Ground state energies per particle in the fermionic (red open triangles) and fictitious bosonic (blue open circles) $\text{CO}_2@^3\text{He}_N$ clusters, as a function of the number of He atoms N .

We can argue that some amount of NCRI and in particular, the turnaround of an effective rotational constant, might be present also for Fermi statistics, as the consequence of the indistinguishability of ^3He atoms and expected sparse energy spectrum for small enough cluster sizes. Our preliminary results for $\text{CO}_2@^3\text{He}_N$ indeed suggest the presence of some amount of NCRI and they are not inconsistent with the turnaround of CO_2 effective rotational constant, as well.

5.3.1 Theory

We have anticipated in Sec. 5.2 that the fermionic states $|\Psi_{n,J}^f\rangle$ of a given angular momentum J and the corresponding energies $E_{n,J}^f$ are accessed by means of imaginary-time CF of a suitably defined antisymmetric operator $\hat{\mathcal{A}}_J$

$$\mathcal{C}_{\hat{\mathcal{A}}_J}(\tau) = \sum_n |\langle \Psi_0 | \hat{\mathcal{A}}_J | \Psi_{n,J}^f \rangle|^2 e^{-(E_{n,J}^f - E_0^b)\tau},$$

where $|\Psi_0\rangle$ and E_0^b are the bosonic ground state wave function and energy. The total angular momentum $\hat{\mathbf{J}}$ of a doped fermionic $\text{X}@^3\text{He}_N$ cluster can be decomposed as $\hat{\mathbf{J}} = \hat{\mathbf{j}} + \hat{\mathbf{\ell}}$, where $\hat{\mathbf{j}}$ and $\hat{\mathbf{\ell}} = \sum_{i=1}^N \hat{\mathbf{\ell}}_i$ are the molecular angular

momentum operator and the operator of the total angular momentum of ³He atoms, respectively. Of course, only J is a good quantum number due to the anisotropy of X-He interaction.

We can formally represent a rotational eigenstate $|\Psi_{JM}^f\rangle$ of the fermionic cluster as a sum of products of eigenstates $\phi_{jm_j}^X$ of the molecular angular momentum and eigenstates $\phi_{\ell m_\ell}^{f,He}$ of the angular momentum of the atomic ³He shell

$$|\Psi_{JM}^f\rangle = \sum_{j,\ell} |\Psi_{JM}^{f,j\ell}\rangle = \sum_{j,m_j,\ell,m_\ell} \phi_{jm_j}^X \otimes \phi_{\ell m_\ell}^{f,He} \langle jm_j, \ell m_\ell | JM \rangle, \quad (5.4)$$

where by $|\Psi_{JM}^{f,j\ell}\rangle$ we denote a fermionic state that has well-defined j and ℓ , that is the quantum numbers of molecular and atomic ³He angular momentum, along with the total angular momentum J . In other words, it is the state $|Jj\ell\rangle$ consistent with fermionic symmetry and $\langle jm_j, \ell m_\ell | JM \rangle$ are CGCs.

Similarly to the above decomposition, we expand a component \mathcal{A}_{JM} of the antisymmetric irreducible operator \mathcal{A}_J as a sum of operator products that act on the molecular (atomic) components of the cluster Hilbert space

$$\mathcal{A}_{JM} = \sum_{j,\ell} \mathcal{A}_{JM}^{j\ell} = \sum_{j,m_j,\ell,m_\ell} o_{jm_j}^X \otimes d_{\ell m_\ell}^{He} \langle jm_j, \ell m_\ell | JM \rangle, \quad (5.5)$$

where the operator $\mathcal{A}_{JM}^{j\ell}$ acts on $|Jj\ell\rangle$ cluster subspace. Operator $o_{jm_j}^X$ acts upon molecular degrees of freedom and $d_{\ell m_\ell}^{He}$ is an antisymmetric operator that accounts for ³He fermionic symmetry and thus the overall antisymmetry of \mathcal{A}_{JM} and its components $\mathcal{A}_{JM}^{j\ell}$.

The rotational eigenstate of an isolated molecule is a spherical harmonics, so that we make a choice $o_{jm_j}^X(\hat{\mathbf{n}}) = Y_{jm_j}(\hat{\mathbf{n}})$, where $\hat{\mathbf{n}}$ is a unit vector along the molecular axis. Now we have to make a choice for the fermionic many-body operator $d_{\ell m_\ell}^{He}$ in Eq. (5.5). Here we recall that we expect structural similarities between bosonic and fermionic doped He clusters, in particular a single solvation shell with well peaked radial density of ³He atoms around the molecule. Therefore it is likely that the nodes of the fermionic ground state in these small systems are angular, rather than radial¹. We proceed

¹The other support for this assumption comes from the Density Functional calculation of Ref. [68] that suggests that a single particle spectrum for SF₆@³He_N clusters exhibits several angular momentum quantum numbers for each of the principal quantum numbers.

with a choice for $d_{\ell m_\ell}^{He}(\hat{\mathbf{n}}^{He})$, where $\hat{\mathbf{n}}^{He}$ stands for a set of N unit vectors that lay along the lines that join the molecular center of mass and the position of each of N ${}^3\text{He}$ atoms, that fulfills two basic criteria

- to be antisymmetric with respect to an interchange of two ${}^3\text{He}$ atoms with like spins
- to be an eigenstate of the angular momentum operator $\hat{\ell} = \sum_{i=1}^N \hat{\ell}_i$ of N ${}^3\text{He}$ atoms, corresponding to quantum numbers ℓ and m_ℓ

Concerning the spin degrees of freedom, we choose that the projection of the total spin carried by N ${}^3\text{He}$ atoms is $S_z = 0$ for N even and $S_z = 1/2$ for N odd. All the above is accomplished by a linear combination of products of “up” and “down” Slater determinants, constructed to have well-defined angular momentum properties²

$$d_{\ell m_\ell}^{He}(\hat{\mathbf{n}}^{He}) = \sum_i \alpha_i \mathcal{D}_{\uparrow i}(Y_{\ell_1 m_{\ell_1}}(\hat{n}_1^{He}), \dots, Y_{\ell_{N_{up}} m_{\ell_{N_{up}}}}(\hat{n}_{N_{up}}^{He})) \\ \times \mathcal{D}_{\downarrow i}(Y_{\ell_{N_{up}+1} m_{\ell_{N_{up}+1}}}(\hat{n}_{N_{up}+1}^{He}), \dots, Y_{\ell_N m_{\ell_N}}(\hat{n}_N^{He})) \quad (5.6)$$

where α_i 's are real coefficients that could be traced to a ladder operators formalism (see Appendix B). We note that the above choice does not uniquely specify the operator component $\mathcal{A}_{JM}^{j\ell}$, Eq. (5.5), that we employ to define CF $\mathcal{C}_{Jj\ell}(\tau)$ in Eq. (5.7). Namely, different sets of single particle orbitals $Y_{\ell_i m_{\ell_i}}$ for $i = 1, \dots, N$, figuring in Eq. (5.6) can be found in a way that a suitable linear combination can be constructed to obey a desired symmetry. We have exploited this freedom and constructed various representations $d_{\ell m_\ell}^{He}(\hat{\mathbf{n}}^{He})$ employing $\ell_i = 0, 1$ and 2 , that correspond to s, p and d angular single particle orbitals. More details on the construction of linear combinations in Eq. (5.6) may be found in Appendix B.

Finally, we define our A-SAITCF

$$\mathcal{C}_{Jj\ell}(\tau) = \left\langle \sum_{M=-J}^J \mathcal{A}_{JM}^{j\ell*}(\tau) \mathcal{A}_{JM}^{j\ell}(0) \right\rangle_0 = \sum_n |\langle \Psi_0 | \hat{\mathcal{A}}_J^{j\ell} | \Psi_{n,J}^{f,j\ell} \rangle|^2 e^{-(E_{n,J}^{f,j\ell} - E_0^b)\tau}, \quad (5.7)$$

²As a support for the choice we make to represent the many-body operator $d_{\ell m_\ell}^{He}$, comes a VMC calculation of Ref. [69] that employs trial wave functions constructed as linear combinations of Slater determinants with well defined angular momentum properties to study pure ${}^3\text{He}_N$ clusters.

that allows us to extract fermionic energies $E_{n,J}^{f,j\ell}$ corresponding to the wave functions $|\Psi_{n,J}^{f,j\ell}\rangle$, or, in other words, the set of quantum numbers $|Jj\ell\rangle$.

We restrict our search on $J = 0$ and $J = 1$ total angular momentum of the cluster and we calculate the fermionic rotational transition in $X@^3\text{He}_N$ that corresponds to $\Delta J = 1$, as:

$$E_{rot}^f = |E_{0,J=1}^{f,j_1\ell_1} - E_{0,J=0}^{f,j_0\ell_0}|, \quad (5.8)$$

where $E_{0,J=1}^{f,j_1\ell_1}$ and $E_{0,J=0}^{f,j_0\ell_0}$ are the lowest fermionic energies that we have identified to have $J = 1$ and $J = 0$ total angular momentum. The indices $j_1\ell_1$ and $j_0\ell_0$ mean that these lowest energies are found for these particular choices of the molecular and atomic angular momenta. The absolute value of the energy difference in Eq. (5.8) is employed because there is no *a priori* constraint on the value of J the absolute fermionic ground state should have, in contrast to the Bose case in which the absolute ground state has $J = 0$ total angular momentum.

The energy $E_{0,J=0}^{f,j_0\ell_0}$ in Eq. (5.8) is found as the lowest energy in the spectral resolution of the CF

$$\mathcal{C}_{0j_0\ell_0}(\tau) = \sum_n |\langle \Psi_0 | \hat{\mathcal{A}}_{J=0}^{j_0\ell_0} | \Psi_{n,J=0}^{f,j_0\ell_0} \rangle|^2 e^{-(E_{n,J=0}^{f,j_0\ell_0} - E_0^b)\tau}, \quad (5.9)$$

that was identified to give the lowest energy among different $\mathcal{C}_{0jl}(\tau)$ CFs with $J = 0$ angular symmetry that we have explored. Only non-zero terms in the above sum are those with $\ell_0 = -j_0$, since otherwise CGSs in Eq. (5.5) are equal to zero. Similarly, $E_{0,J=1}^{f,j_1\ell_1}$ is the lowest energy in the spectral decomposition of the CF

$$\mathcal{C}_{1j_1\ell_1}(\tau) = \sum_n |\langle \Psi_0 | \hat{\mathcal{A}}_{J=1}^{j_1\ell_1} | \Psi_{n,J=1}^{f,j_1\ell_1} \rangle|^2 e^{-(E_{n,J=1}^{f,j_1\ell_1} - E_0^b)\tau}, \quad (5.10)$$

that gives rise to the lowest energy among different $\mathcal{C}_{1jl}(\tau)$ CFs with $J = 1$ angular symmetry that have been explored. It contains only the terms that obey $|j_1 - \ell_1| \leq 1$, in accordance with CGSs rules.

Our procedure of extracting fermionic rotational excitations using operators $\mathcal{A}_{JM}^{j\ell}$ with specified values of j and ℓ angular momenta is advantageous if the exact fermionic ground state wave function $|\Psi_{JM}^f\rangle$ of angular momentum J in Eq. (5.4) has a dominant contribution from the wave function $|\Psi_{JM}^{f,j\ell}\rangle$,

i.e. $|Jj\ell\rangle$. We have already seen such a situation in Sec. 4.2 where we have discussed four bound rotational states of a CO-He dimer (see Tab. 4.1). The signal that this favorable case is met also in the present case would be suggestive of high values of the spectral weights (close to 1) of extracted energies. This would lead in turn to a facilitated ILT procedure to extract energies from $\mathcal{C}_{Jj\ell}(\tau)$ CFs.

In the next Section we apply our A-SAITCF approach to calculate fermionic rotational excitations in small $\text{CO}_2@{}^3\text{He}_N$ clusters. The reason why we choose CO_2 molecule is that the minimum of its effective rotational constant in ${}^4\text{He}$ clusters happens already at $N = 5$, that is the smallest size of all known doped He clusters at which the turnaround is observed.

5.3.2 Results and discussion

Let us denote with E_0 and E_1 the energies $E_{J=0}^{f,j_0\ell_0} - E_0^b$ and $E_{J=1}^{f,j_1\ell_1} - E_0^b$ extracted from CFs $\mathcal{C}_{0j_0\ell_0}(\tau)$ and $\mathcal{C}_{1j_1\ell_1}(\tau)$ in Eqs. (5.9) and (5.10). With the purpose of the illustration of the way the energies E_0 and E_1 are identified, as well as how the fermionic rotational excitations corresponding to $\Delta J = 1$ are calculated, we display in Fig. 5.6 the energy level pattern calculated with A-SAITCF approach for $\text{CO}_2@{}^3\text{He}_2$ cluster.

The first thing we note is a remarkable richness of possible rotational levels the A-SAITCF method reveals. This is traced down to the freedom we have in choosing different sets of single particle states $s^n p^m d^{N-n-m}$ for N ${}^3\text{He}$ atoms, that give rise to a given angular momentum ℓ of the atomic ${}^3\text{He}$ shell (see Eq. (5.6) and the comment below the equation). The lowest rotational levels of a given angular momentum J , that are emphasized by being enclosed in the gray dashed boxes in Fig. 5.6, are the only energy levels that are found by means of standard dipole-dipole $\mathcal{C}_{\hat{n}}(\tau)$ CF.

Our preliminary results for fermionic rotational excitations in $\text{CO}_2@{}^3\text{He}_N$ for cluster sizes up to $N = 10$ are summarized in Tab. 5.1. The table reports the energies E_0 and E_1 , that are identified in a manner analogous to the one illustrated in Fig. 5.6, along with the corresponding spectral weights A_0 and A_1 . Also, the sets of single particle orbitals (configurations), as well as the sets of quantum numbers $|Jj\ell\rangle$ that characterize the CF employed to extract

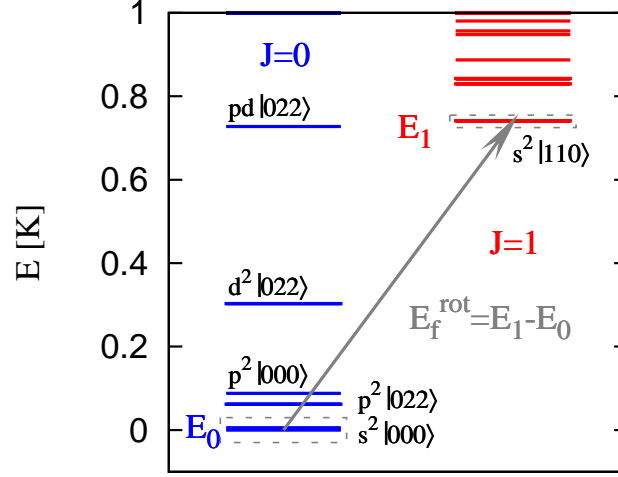


Figure 5.6: Two stacks of rotational energy levels corresponding to angular momentum $J = 0$ (left stack, blue color) and $J = 1$ (right stack, red color) calculated with A-SAITCF method for $\text{CO}_2@{}^3\text{He}_2$ cluster. We note that in this case all energies correspond to rotational excitations of distinguishable particles. $|Jj\ell\rangle$ denotes the sets of quantum numbers that corresponds to A-SAITCF $C_{Jj\ell}(\tau)$ from which a given excitation is extracted; set of single particle orbitals employed to construct a given CF is indicated. The lowest identified rotational level of a given symmetry is emphasized by being enclosed in a dashed gray box. The resulting $J = 0 \rightarrow 1$ rotational transition is denoted by the gray arrow.

tabulated energies, are indicated. The rest of the table reports rotational transitions E_{rot}^b in the fictitious bosonic $\text{CO}_2@{}^3\text{He}_N$ clusters for $J = 0 \rightarrow 1$, as well as our final result, the fermionic rotational transition E_{rot}^f corresponding to $\Delta J = 1$, found by means of Eq. (5.8). Here we also mention that the fermionic ground state energies per particle reported in Fig. 5.5 are calculated for a given cluster size N as $e_0^f = e_0^b + \frac{\min(E_{0,J}^f - E_0^b)}{N}$. The tabulated results for the rotational excitations in bosonic and fermionic $\text{CO}_2@{}^3\text{He}_N$ clusters are displayed in Fig. 5.7. We note that our preliminary results reveal certain amount of NCRI in these fermionic systems; also they are not inconsistent with the presence of the turnaround of the effective CO_2 rotational constant in this fermionic cluster. However, we also note the presence of nonphysically low rotational transitions we have identified in clusters with $N = 3$ and

N	A_0	E_0 [K]	Conf. $ J = 0 j_0 \ell_0\rangle$	A_1	E_1 [K]	Conf. $ J = 1 j_1 \ell_1\rangle$	E_{rot}^b [K]	E_{rot}^f [K]
2	1	0	$s^2 000\rangle$	0.976(18)	0.740(16)	$s^2 110\rangle$	0.740(16)	0.740(16)
3	0.45(4)	0.45(5)	$sp^2 011\rangle$	0.95(3)	0.521(9)	$s^2 p 101\rangle$	0.5612(13)	0.07(4)*
4	0.93(4)	0.0378(9)	$s^2 p^2 011\rangle$	0.87(4)	0.476(6)	$s^2 p^2 101\rangle$	0.4505(12)	0.438(5)
5	0.800(10)	0.189(5)	$sp^4 000\rangle$	0.92(2)	0.428(6)	$s^2 p^3 111\rangle$	0.3904(17)	0.239(8)
6	0.289(4)	1.089(15)	$p^3 d^3 011\rangle$	0.684(5)	0.873(7)	$sp^3 d^2 133\rangle$	0.4718(16)	0.216(16)
7	0.603(16)	1.51(3)	$sp^6 000\rangle$	0.81(2)	1.56(3)	$s^2 p^5 101\rangle$	0.549(2)	0.05(4)*
				0.56(3)	1.91(5)	$s^6 110\rangle$		0.40(6)
8	0.65(3)	1.47(5)	$s^2 p^6 000\rangle$	0.56(5)	1.85(8)	$s^2 p^6 110\rangle$	0.579(2)	0.38(9)
9	0.892(6)	3.05(2)	$sp^3 d^5 000\rangle$	0.67(5)	3.56(19)	$sp^6 d^2 101\rangle$	0.642(4)	0.51(15)
10	0.78(6)	3.6(2)	$s^2 p^6 d^2 011\rangle$	0.78(5)	3.20(15)	$s^2 p^6 d^2 101\rangle$	0.667(5)	0.40(25)

Table 5.1: Energies $E_0 = E_{j=0}^{j_0 \ell_0} - E_0^b$ and $E_1 = E_{j=1}^{j_1 \ell_1} - E_0^b$ and the corresponding spectral weights A_0 and A_1 extracted from the CFs in Eqs. (5.9) and (5.10) of $J = 0$ and $J = 1$ total angular momentum for $\text{CO}_2@{}^3\text{He}_N$ clusters. The particular choices for single particle orbitals (configurations), as well as for sets of quantum numbers $|J = 0 j_0 \ell_0\rangle$ and $|J = 1 j_1 \ell_1\rangle$ are indicated. The last two columns display the energies of rotational transition $J = 0 \rightarrow 1$ in the fictitious bosonic clusters E_{rot}^b and the fermionic rotational transitions corresponding to $\Delta J = 1$, E_{rot}^f , calculated by means of Eq. (5.8).

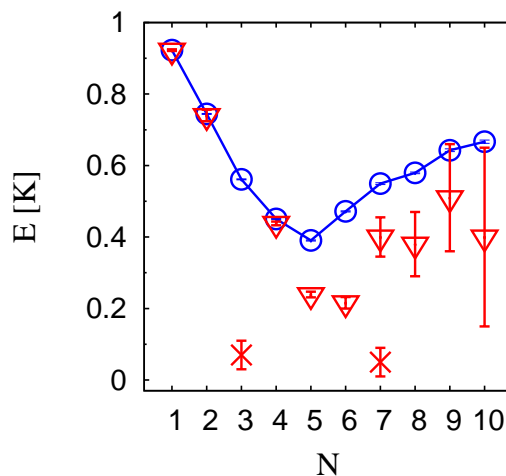


Figure 5.7: Rotational excitations in fermionic (open red triangles) and fictitious bosonic (open blue circles) $\text{CO}_2@{}^3\text{He}_N$ clusters, as a function of the number of He atoms N . Red crosses indicate nonphysically low rotational transitions that have been marked with asterisks in Tab. 5.1, see in the text.

$N = 7$ ${}^3\text{He}$ atoms that are indicated with the crosses in Fig. 5.7 and with the asterisks in Tab. 5.1. This means that we have failed to identify the true ground states with a given angular momentum J in these cases. The possible causes could be the restrictions on the values of quantum numbers $|Jj\ell\rangle$ that we have explored³ or/and that the unfavorable case is met when the ground rotational levels of a given total angular momentum J do not have a dominant contribution from any of the sets $|Jj\ell\rangle$ we have explored⁴. For $N = 7$ we find that the second-lowest rotational transition actually lays in the physical region (open red triangle in Fig. 5.7, also shown in Tab. 5.1). Concerning the spectral weights, we indeed observe from Tab. 5.1 that some of them are uncomfortably small, signaling that unfavorable situations are indeed met. This prompts the need for a further work that would fully clarify this issue and make one capable to draw the final conclusions.

³This would correspond to the identification of some transition between rotational levels—other than the ground states of $J = 0$ and $J = 1$ —so that thus obtained energies could be nonphysically low, as it is the case for the rotational transition $pd|022\rangle \rightarrow s^2|110\rangle$ in Fig. 5.6.

⁴In these cases there is also the problem of extracting reliably a fairly faint spectral features due to difficulties related to the ILT.

A possible direction to achieve this goal could be the following. Suppose we calculate the imaginary-time autocorrelation functions of two operators \hat{A} and \hat{B} , *i.e.* $\mathcal{C}_{\hat{A}}(\tau)$ and $\mathcal{C}_{\hat{B}}(\tau)$. We can obtain, at no extra cost, also the autocorrelation function $\mathcal{C}_{\alpha\beta}(\tau)$ of any linear combination of them, $\alpha\hat{A} + \beta\hat{B}$. It is sufficient to accumulate also the values of the “mixed” imaginary-time correlation $\langle \hat{A}(0)\hat{B}(\tau) \rangle$, which simply requires products of already calculated quantities. After the simulation, the desired quantity

$$\mathcal{C}_{\alpha\beta}(\tau) = \alpha^2 \langle \hat{A}(0)\hat{A}(\tau) \rangle + \beta^2 \langle \hat{B}(0)\hat{B}(\tau) \rangle + 2\alpha\beta \langle \hat{A}(0)\hat{B}(\tau) \rangle$$

can be readily obtained for any choice of the coefficients. One can then proceed and optimize the coefficients α and β by maximizing the spectral weight of a particular excitation. The generalization to linear combinations of more than two operators is straightforward.

Apart from exploring a larger range of quantum numbers $|Jj\ell\rangle$, and the above discussed “mixed” CFs indicated as a possible extension of this work, further direction could be to study also the fully polarized fermionic clusters. Namely, in the light of the experiment of Grebenev *et al.* [28, 29] the fully polarized He cluster would correspond to the situation when the quantum exchanges would be enhanced, since all the fermions could in principle participate in the same exchange cycle (in contrast with the case investigated here, where just half of the atoms were indistinguishable, since half of them had the same spin). In this sense, systems with maximum polarization are expected to be more favorable.

In summary, we have introduced A-SAITCFs approach in order to study rotational spectra of small doped fermionic ^3He clusters within RQMC computational scheme. We have applied this method to study small $\text{CO}_2@^3\text{He}_N$ clusters. Our preliminary results indicate that a certain amount of NCRI is found also in these fermionic systems. Also, our results are not inconsistent with the presence of the turnaround of the effective rotational constant of CO_2 solvated with fermions.

Conclusions

Although main features in the spectra of ^4He solvated molecules are now well understood, namely the non-classical rotational inertia and its most remarkable consequence, the turnaround of the effective rotational constant observed for some dopant molecules, many subtle spectral features still escape a complete theoretical understanding. A growing body of experimental information becoming available in small to medium, as well as in large ^4He nanodroplets, bring to the view many new phenomena that go beyond the free-rotor-like picture. This motivated us to develop the methodology of calculating rotational excitations from the unconventional imaginary-time correlation functions, in the computational framework of reptation quantum Monte Carlo method. These correlation functions are specifically devised for an explicit theoretical characterization of individual excitations, as well as for an enhanced computational efficiency in the calculation of weak spectral features.

Applying newly developed approach we dwelled upon the causes that lead to line splittings observed in the spectra of small $\text{CO}@^4\text{He}_N$ clusters. Also, we have discussed the proposed assignment of the weak satellite band, observed in the infrared spectra of ^4He solvated CO_2 , to a coupled rotational state of the molecule and the ring of ^4He atoms. Further, our simulations help discriminating between different experimental assignments of spectral lines proposed for $\text{CO}@^4\text{He}_N$ around the cluster size where one of the line splittings is observed. In addition, we have contributed to the open debate about the approach of the CO effective rotational constant to its limiting value in large ^4He nanodroplets, concluding that CO should attain its size-independent rotational behaviour soon after the completion of the first ^4He solvation shell around the molecule.

Finally, we have addressed an exciting physical issue on the influence the particle statistics of a quantum solvent exhibits on the spectra of embedded molecules. Namely, we have generalized our symmetry-adapted imaginary-time correlation functions approach to access ground state and excited rotational states of small doped fermionic clusters. We have applied this approach to $\text{CO}_2@^3\text{He}_N$ clusters and our preliminary results indicate that a certain amount of non-classical rotational inertia is found also in these fermionic systems. Also, the results are not inconsistent with the presence of the turnaround of the effective rotational constant of CO_2 molecule solvated with fermions.

In general, coping with the problem of excited states of strongly interacting systems is a difficult task. Most of the problems studied in this thesis moved beyond a particularly favorable situation of dominant features of bosonic spectra, which led to the spectacular progress in the previous work on doped ^4He clusters. Therefore it could be expected—and was indeed found—to be extremely challenging.

Appendix A

More details on the spectra of CO isotopomers

In this section we will address with more details the rotational excitations of different CO isotopomers. Also, we will explore how the isotopic analysis, *i.e.* the so-called “reduced mass/center of mass shift” model proposed in Ref. [23] to disentangle rotational and vibrational contributions to $R(0)$ experimental lines, applies to RQMC data.

A.1 Rotational energies of CO isotopomers

We have calculated rotational energies of four CO isotopic species in He up to $N = 20$. Different isotopomers were treated by using appropriate values of mass and gas-phase rotational constants, as well as by shifting CO-He potential along the molecular axis for the amount $\Delta z^{(i)}$ for the i -th isotopomer (see Tab. A.3), opposite to the shift in the center of mass with respect to the reference $^{12}\text{C}^{16}\text{O}$ isotope (see Fig. 3.1). In principle, the implementation of the correlated sampling technique to infer the properties of all the isotopomers from the configurations sampled for one of them, is straightforward in RQMC. In practice, this requires fairly large number of time slices to be used in the path, so that we have found very large fluctuations of the corresponding weights. This made the usage of correlated sampling impractical, so that rotational excitations for different CO isotopomers have been obtained

from the independent runs. Tab. A.1 and Tab. A.2 are listing *a*-type and *b*-type rotational excitations for four CO isotopic species, respectively, calculated with both CBS+corr and SAPT potentials¹. Fig. A.1 displays theoretical and experimental values of R(0) roto-vibrational lines for ¹²C¹⁸O, ¹³C¹⁶O and ¹³C¹⁸O isotopomer. This is a complementary information with respect to the results for the normal isotopomer that we have already seen in the left panel of Fig. 3.13. There is remarkable agreement between theory and experiment. Experimentally, a limited number of split lines in the *b*-series is observed in the size range $N = 4 - 8$ [26] for all the isotopomers and they show subtle differences among different isotopomers in the size range $N = 4 - 8$ [26]. In the presence of such a small energy difference between the split lines, the procedure of extracting rotational energies from ILT is not accurate enough (see Sec. 2.3 and 2.4) and presumably gives at best the weighted average of the split lines. We note that the rotational energies calculated with SAPT and CBS+corr potentials are very similar, as it has been already seen in Fig 3.13, with the SAPT energies being only slightly higher than the ones calculated with CBS+corr potential. However, the stronger red and blue vibrational shifts resulting from SAPT and CBS+corr potentials, respectively, prevail in the calculated R(0) transitions, making the SAPT R(0) energies being too low and CBS+corr R(0) energies too high, when compared to the experimental values in Fig. 3.14.

In our calculations we employ adiabatic approximation, *i.e.* we use CO-He potential averaged over the period of molecular vibration. This implies that a small effect on the potential coming from the change in the vibrational ground state of the molecule upon isotopic substitution is neglected. We have already mentioned that the quality of the linear fit proposed in Ref. [23] (see Fig. 3.2) is significantly improved when correction due to isotope-induced shift in the intermolecular potential is taken into account². The effective

¹Results pertaining to the CBS+corr are obtained with $\beta = 0.5$, $\epsilon = 10^{-3}$, and $\tau_{\max} = 0.5$ inverse Kelvin, which implies sampling paths with 1500 time slices. With this choice of τ_{\max} the rotational energies for small N are slightly overestimated. The SAPT results, obtained with $\tau_{\max} = 0.7$ and $\epsilon = 5 \times 10^{-4}$, are better converged for small sizes.

²In our calculations we employ adiabatic approximation, *i.e.* we use CO-He potential averaged over the period of molecular vibration. This implies that a small effect on the

N	CBS+corr						SAPT			
	$^{12}\text{C}^{16}\text{O}$		$^{12}\text{C}^{18}\text{O}$		$^{13}\text{C}^{18}\text{O}$		$^{12}\text{C}^{16}\text{O}$			
	E_{rot}	A	E_{rot}	A	E_{rot}	A	E_{rot}	A		
1	0.99(18)	0.113(16)	0.9(3)	0.11(3)	0.68(19)	0.096(15)	1.09(8)	0.143(9)	0.79(4)	0.112(4)
2	0.96(7)	0.223(12)	0.94(8)	0.231(14)	0.73(16)	0.21(2)	0.93(4)	0.251(8)	0.67(6)	0.196(11)
3	0.84(5)	0.281(13)	0.87(3)	0.316(6)	0.81(4)	0.313(8)	0.85(2)	0.337(6)	0.768(18)	0.292(4)
4	0.83(6)	0.352(13)	0.75(11)	0.35(3)	0.79(6)	0.376(16)	0.75(6)	0.378(15)	0.874(12)	0.367(3)
5	0.92(2)	0.410(6)	0.87(3)	0.414(9)	0.89(3)	0.429(8)	0.83(2)	0.431(6)	0.991(12)	0.411(4)
6	1.03(4)	0.431(10)	1.02(3)	0.446(9)	1.00(4)	0.452(12)	0.95(3)	0.458(8)	1.149(11)	0.448(4)
7	1.29(3)	0.452(8)	1.24(3)	0.467(8)	1.20(3)	0.466(9)	1.16(4)	0.478(14)	1.408(19)	0.463(7)
8	1.69(3)	0.473(9)	1.67(2)	0.494(7)	1.62(4)	0.489(13)	1.58(4)	0.511(13)	1.87(3)	0.482(10)
9	2.24(7)	0.50(2)	2.14(8)	0.50(3)	2.11(8)	0.51(3)	2.05(9)	0.52(4)	2.47(5)	0.536(19)
10	3.00(7)	0.62(3)	2.85(6)	0.61(3)	2.87(7)	0.64(3)	2.79(8)	0.66(4)	3.49(15)	0.57(4)
11	3.56(5)	0.74(3)	3.53(6)	0.78(4)	3.45(5)	0.78(3)	3.34(9)	0.79(6)	3.84(3)	0.60(5)
12	4.01(3)	0.880(9)	3.85(9)	0.849(5)	3.86(2)	0.913(9)	3.64(10)	0.86(7)	4.07(9)	0.87(5)
13	4.16(4)	0.911(16)	4.05(3)	0.925(9)	3.991(14)	0.941(4)	3.85(2)	0.942(7)	4.26(5)	0.931(11)
14	4.23(2)	0.935(4)	4.08(3)	0.936(8)	4.00(2)	0.943(4)	3.83(2)	0.939(6)	4.37(3)	0.87(5)
15	4.299(10)	0.949(2)	4.13(2)	0.937(15)	4.01(2)	0.943(5)	3.85(3)	0.923(12)	4.26(4)	0.931(7)
16	4.307(13)	0.950(3)	4.19(2)	0.957(4)	4.00(3)	0.941(9)	3.83(3)	0.938(8)	4.33(3)	0.947(5)
17	4.281(14)	0.946(3)	4.13(2)	0.946(5)	4.03(2)	0.952(3)	3.900(16)	0.953(3)	4.38(4)	0.950(8)
18	4.34(3)	0.958(5)	4.14(3)	0.948(6)	4.068(16)	0.954(3)	3.88(3)	0.947(7)	4.38(4)	0.951(8)
19	4.33(2)	0.955(3)	4.15(3)	0.951(4)	4.02(6)	0.947(11)	3.90(2)	0.954(4)	4.37(4)	0.953(7)
20	4.30(4)	0.950(7)	4.20(2)	0.957(4)	3.98(3)	0.940(6)	3.92(3)	0.956(5)	4.34(4)	0.949(7)
25	4.35(5)	0.963(6)							4.31(12)	0.956(12)
30	4.05(11)	0.89(4)							4.33(11)	0.961(8)
35	4.12(7)	0.92(2)								
40	4.14(7)	0.938(15)								
45	4.14(9)	0.94(2)								
50	4.15(10)	0.945(18)								
100	4.05(9)	0.943(11)								

Table A.1: The a -type rotational energies E_{rot} (in K) and their spectral weights A of CO@He_N computed with RQMC using the CBS+corr potential for four CO isotopomers, as well as with the SAPT potential for the normal isotopomer. The SAPT data at $N = 25$ and 30 are from Ref. [24].

		CBS+corr						SAPT	
		$^{12}\text{C}^{16}\text{O}$		$^{13}\text{C}^{16}\text{O}$		$^{12}\text{C}^{18}\text{O}$		$^{13}\text{C}^{18}\text{O}$	
N	E_{rot}	A	E_{rot}	A	E_{rot}	A	E_{rot}	A	E_{rot}
1	5.88(20)	0.873(6)	5.58(23)	0.871(8)	5.37(14)	0.855(7)	5.52(5)	0.850(7)	5.85(4)
2	6.44(13)	0.759(6)	6.22(16)	0.746(13)	5.8(3)	0.746(13)	6.05(8)	0.736(4)	5.9(3)
3	6.88(17)	0.683(3)	6.80(8)	0.666(3)	6.65(12)	0.662(3)	6.64(8)	0.647(4)	6.67(10)
4	7.2(3)	0.611(3)	6.7(5)	0.594(20)	7.1(3)	0.595(5)	6.7(3)	0.587(3)	7.41(10)
5	7.75(12)	0.565(3)	7.41(18)	0.556(4)	7.51(18)	0.541(2)	7.15(14)	0.536(3)	7.70(9)
6	7.7(3)	0.536(3)	7.54(20)	0.524(3)	7.5(2)	0.515(3)	7.23(17)	0.510(4)	7.99(11)
7	7.62(15)	0.515(4)	7.54(17)	0.505(4)	7.33(17)	0.499(5)	7.1(3)	0.486(5)	7.86(13)
8	7.41(13)	0.496(7)	7.38(12)	0.478(5)	7.12(20)	0.477(8)	7.11(20)	0.458(8)	7.50(17)
9	7.0(3)	0.465(18)	6.8(4)	0.46(2)	6.7(3)	0.45(2)	6.4(5)	0.44(3)	7.4(2)
10	7.4(4)	0.35(3)	7.1(3)	0.37(3)	7.2(4)	0.33(3)	7.0(5)	0.32(4)	9.1(3)
11	8.0(5)	0.23(2)	8.1(8)	0.20(3)	8.3(6)	0.19(2)	7.5(12)	0.18(5)	11.4(7)
									0.148(12)

Table A.2: The b -type rotational energies E_{rot} (in K) and their spectral weights A of CO@He ν computed with ROMC using the CBS+corr potential for four CO isotopomers, as well as with the SAPT potential for the normal isotopomer.

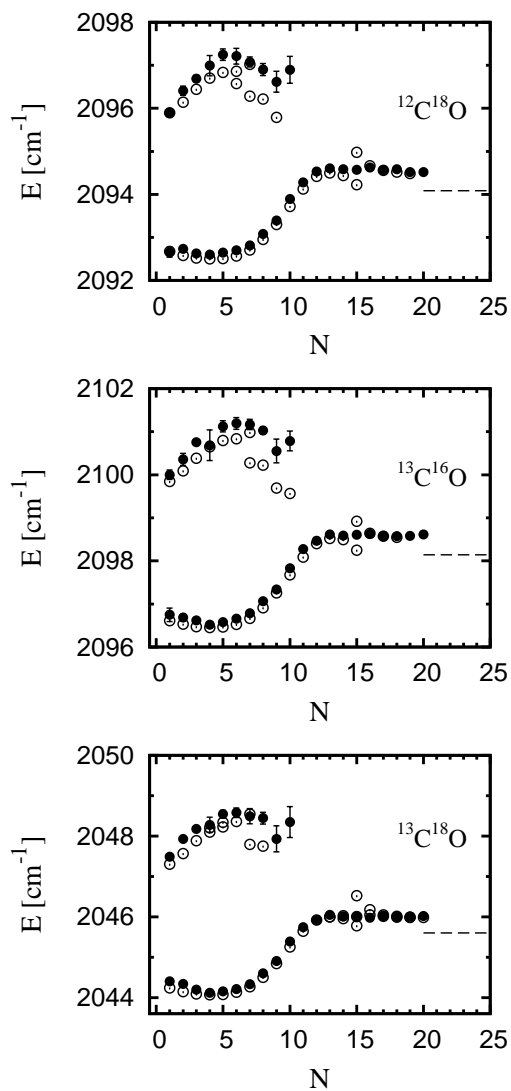


Figure A.1: Energies of R(0) transitions in CO@He $_N$ clusters for $^{12}\text{C}^{18}\text{O}$, $^{13}\text{C}^{16}\text{O}$ and $^{13}\text{C}^{18}\text{O}$ isotopomer: experimental line positions of Ref. [26] (open circles) and RQMC data obtained by summing up vibrational and rotational contributions in roto-vibrational lines, Eq. (3.1), using CBS+corr potential (filled circles). Horizontal dashed line is energy of the R(0) transition for a given isotopomer measured in He nanodroplet [23].

	$^{12}\text{C}^{16}\text{O}$	$^{12}\text{C}^{18}\text{O}$	$^{13}\text{C}^{16}\text{O}$	$^{13}\text{C}^{18}\text{O}$
$\omega_i[\text{\AA}]$	2145.412	2094.085	2098.142	2045.602
$\nu_i[\text{\AA}]$	2143.271	2092.122	2096.067	2043.67
$\Delta z^{(i)}[\text{\AA}]$	0.0	0.032237	-0.022233	0.010399
$\frac{\partial B}{\partial \Delta z} \Delta z^{(i)}[\text{cm}^{-1}]$	0.0	0.025	0.017	0.008

Table A.3: Experimental values ω_i of R(0) transitions in He nanodroplets [23], experimental values of the monomer band origins ν_i in the gas-phase [25, 47], center of mass shifts $\Delta z^{(i)}$ and the values of $\frac{\partial B}{\partial \Delta z} \Delta z^{(i)}$ (see Eq. (3.2)) calculated in Ref. [23] for the four isotopomers.

CO-He potential becomes more or less isotropic depending on the separation between the center of rotation, *i.e.* the center of mass and the so called “center of interaction”, that could be defined as a point where the effective potential anisotropy is minimized. It is found both experimentally and theoretically [23], that $^{13}\text{C}^{16}\text{O}$ rotates more freely than $^{12}\text{C}^{18}\text{O}$, thus having larger effective rotational constant than the later, although their reduced masses are very similar. Results of our simulations show this effect, since the rotational excitations for $^{13}\text{C}^{16}\text{O}$ lay consistently above the ones for $^{12}\text{C}^{18}\text{O}$. This is so because in the case of $^{13}\text{C}^{16}\text{O}$ the center of mass is shifted to the carbon end, while for $^{12}\text{C}^{18}\text{O}$ is shifted oppositely, to the oxygen atom, in the direction of the main potential well, thus inducing more rotational anisotropy in the CO-He interaction.

A.2 Separation of rotational and vibrational effects

In order to see how the isotopic analysis applies on our data, we have performed a two-dimensional fit in the range $N = 12 - 20$, of the form

potential coming from the change in the vibrational ground state of the molecule upon isotopic substitution is neglected.

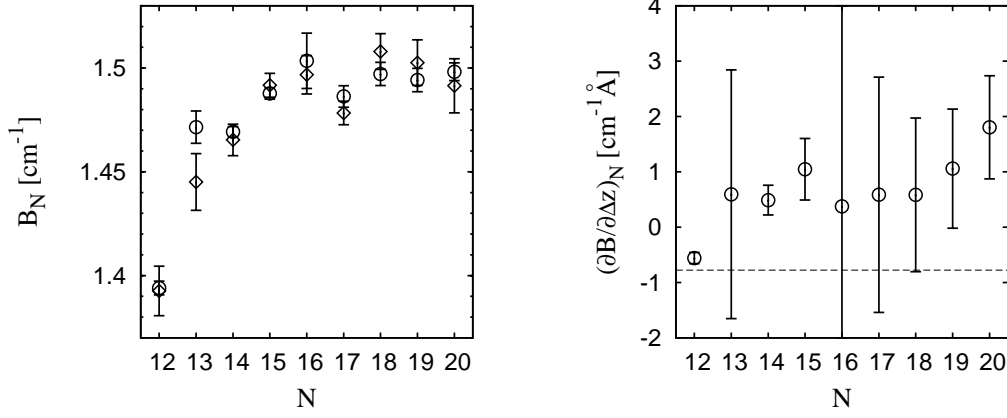


Figure A.2: Left panel: cluster size evolution of $B_N^{(1)}$ as a parameter in the fit, Eq. (A.1), (open circles) and RQMC effective rotational constants obtained with CBS+corr potential in the size range (open diamonds). Right panel: cluster size evolution of $(\partial B/\partial \Delta z)_N$ as a parameter in the fit, Eq. (A.1). The horizontal dashed line is the value calculated in Ref. [23].

$f_N(x, y) = B_N^{(1)}x + (\partial B/\partial \Delta z)_N \Delta z^{(i)}$, namely

$$2E_{rot}^{(i)} = 2\frac{\mu^{(1)}}{\mu^{(i)}}B^{(1)} + 2\frac{\partial B}{\partial \Delta z}\Delta z^{(i)} \quad (\text{A.1})$$

with $B_N^{(1)}$ and $(\partial B/\partial \Delta z)_N$ as fitting parameters. Cluster size evolution of these parameters is shown on Fig. A.2. The values of the effective rotational constant coming from the fit are matching the calculated values, while the fitting parameters $(\partial B/\partial \Delta z)_N$ are showing tendency of being positive (although with large errors), while by definition they have to be strictly negative. We conclude that although the statistical accuracy of our results is not sufficient to perform the convincing fit, similar to the one proposed by “reduced mass/center of mass shift” model, our results still indicate that unphysical tendency of $(\partial B/\partial \Delta z)_N$ of having the wrong sign, suggests that the same model is not applicable in this size range. In addition, we observe linear dependence of the vibrational shift on the small parameter Δz . Namely, we fit the vibrational shifts $\Delta \nu^{(i)}(N)$ of CO isotopomers on the form

$$\Delta \nu^{(i)}(N) = k(N)\Delta z^{(i)} + \Delta \nu^{(1)}(N) \quad (\text{A.2})$$

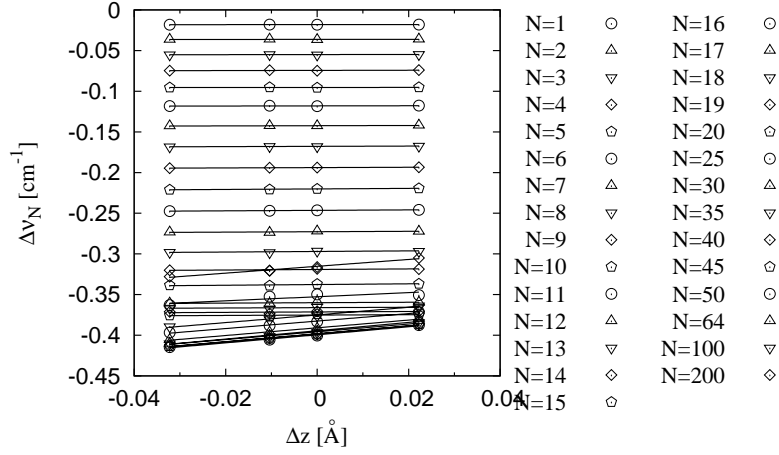


Figure A.3: Linear fits of CO isotopomers vibrational shifts versus Δz , small parameter characterizing center of mass shift of a given isotopomer with respect to the normal isotopomer $^{12}\text{C}^{16}\text{O}$, for cluster sizes in the range $N = 1 - 200$.

where $\Delta\nu^{(1)}(N)$ is the vibrational shift of the normal isotopomer. Our fits are shown on Fig. A.3 for all simulated cluster sizes in the range $N = 1 - 200$. Fig. A.4 shows the same fits but for selected cluster sizes $N = 30, 40, 50, 100$ and 200. Fig. A.5 displays the cluster size evolution of the coefficient k in the linear fit of Eq. (A.2). Although we see that this coefficient is different from zero for $N > 20$, its small value leads to negligible effect of the order $\sim 0.005\text{cm}^{-1}$ on the vibrational shifts in the cluster size range studied here, so that omitting isotopic dependence of the vibrational shift in the linear fit of Eq. (A.1) is justified.

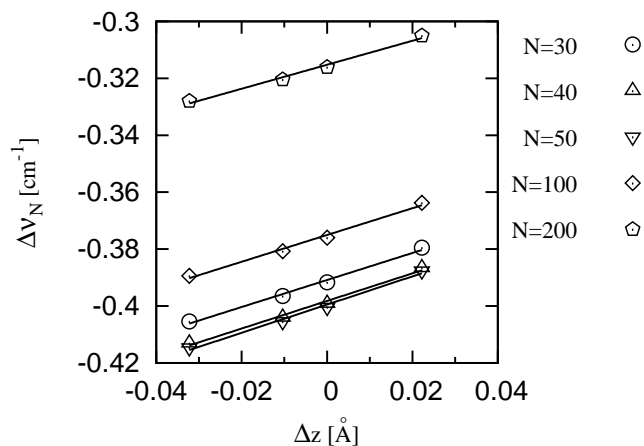


Figure A.4: Linear fits of CO isotopomers vibrational shifts versus Δz , small parameter characterizing center of mass shift of a given isotopomer with respect to the normal isotopomer $^{12}\text{C}^{16}\text{O}$, for cluster sizes $N = 30, 40, 50, 100$ and 200 .

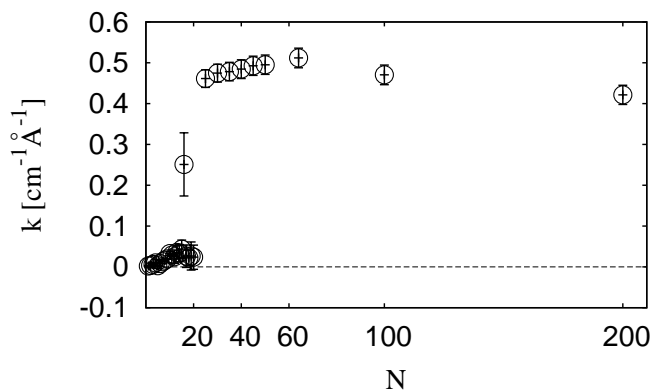


Figure A.5: Cluster size evolution of of the coefficient $k(N)$ figuring in Eq. (A.2).

Appendix B

Coupling of antisymmetrized single particle orbitals

We will discuss now in more detail the procedure we use to construct a representation for the fermionic many-body operator $d_{\ell m_\ell}^{He}$ in Eq. (5.5), that is $d_{\ell m_\ell}(\hat{\mathbf{n}}^{He})$. The goal is to determine a suitable linear combination of Slater determinants (whose general form is given by Eq. (5.6)) that has a well-defined angular momentum properties, that is ℓ and m_ℓ quantum numbers. However, as we have anticipated in Subsec. 5.3.1, this representation is not unique and we proceed by exploiting the freedom to construct various representations by employing different sets of single particle orbitals $Y_{\ell_i m_{\ell_i}}$ for $i = 1, \dots, N$, in Eq. (5.5). In the following, we will describe general procedure we use, and subsequently we will illustrate it on a specific example of $N = 6$ ${}^3\text{He}$ atoms in $s^2 p^4$ configuration.

B.1 General procedure

One starts by choosing the set of N single particle orbitals, or quantum numbers ℓ_i for $i = 1, \dots, N$, that is $\ell_1^{n_1} \ell_2^{n_2} \dots \ell_q^{n_q}$, where $\sum_{i=1}^q n_i = N$. Then, the configuration that corresponds to the maximum values of ℓ and m_ℓ , that is $\ell = \ell_{max}$ and $m_\ell = \ell_{max}$, as well as to a given projection of the total spin, that fulfills Pauli exclusion principle has to be identified. We denote

appropriate state with $({}^{2S+1}L, \ell = \ell_{max}, m_\ell = \ell_{max})$, where S is the total spin of the configuration and ${}^{2S+1}L$ plays the role similar to an atomic term. This configuration always has the form of a single determinant. In order to obtain linear combination of determinants that correspond to lower values of the quantum number m_ℓ , one has to employ formalism of ladder operators [70]:

$$\hat{L}_-(\ell = \ell_{max}, m_\ell = \ell_{max}) = \sqrt{(\ell + m_\ell)(\ell - m_\ell + 1)} \quad (\ell = \ell_{max}, m_\ell = \ell_{max} - 1) \quad (\text{B.1})$$

On the other side, the same effect would be obtained by applying $\hat{L}_- = \sum_{i=1}^N \hat{\mathcal{L}}_{i-}$ directly on the set of single particle orbitals. Finally, in this way the configuration $(\ell = \ell_{max}, m_\ell = \ell_{max} - 1)$ is identified. Further, linear combinations that correspond to $\ell < \ell_{max}$ have to be found. To this end, we have to take care that the state $(\ell = \ell_{max} - 1, m_\ell = \ell_{max} - 1)$ is orthogonal to the state $(\ell = \ell_{max}, m_\ell = \ell_{max} - 1)$. Applying recursively this argument, we arrive to the whole set of linear combinations of determinants we need in order to calculate a given A-SAITCF.

B.2 An example

Now we will give a concrete example for $N = 6$ and s^2p^4 as the set of single particle. The number of atoms is now even, so that in accordance with our choice the projection of the total spin is $S_z = 0$. Consequently, we have 3 “up” and 3 “down” ${}^3\text{He}$ atoms

$$\begin{array}{cccccc} s & p & p & s & p & p \\ \uparrow & \uparrow & \uparrow & \downarrow & \downarrow & \downarrow \\ 1 & 2 & 3 & 4 & 5 & 6 \end{array}$$

Now we have to identify the configuration with $\ell_{max}, m_{\ell_{max}} = \ell_{max}$ and $S_z = 0$, that is in accordance with Fermi exclusion principle. We note that this configuration corresponds to $\ell = m_\ell = 2$ and it is explicitly:

$(\ell_1 m_{\ell_1})^{s_{z_1}}$	ℓm_ℓ					
$(00)^+$	$(11)^+$	$(10)^+$	$(00)^-$	$(11)^-$	$(10)^-$	22

and it has the form of single determinant:

$$d_{2,2} = \begin{vmatrix} Y_{00}(\hat{\mathbf{n}}_1) & Y_{11}(\hat{\mathbf{n}}_2) & Y_{10}(\hat{\mathbf{n}}_3) \\ Y_{00}(\hat{\mathbf{n}}_1) & Y_{11}(\hat{\mathbf{n}}_2) & Y_{10}(\hat{\mathbf{n}}_3) \\ Y_{00}(\hat{\mathbf{n}}_1) & Y_{11}(\hat{\mathbf{n}}_2) & Y_{10}(\hat{\mathbf{n}}_3) \end{vmatrix}_{\uparrow} \times \begin{vmatrix} Y_{00}(\hat{\mathbf{n}}_4) & Y_{11}(\hat{\mathbf{n}}_5) & Y_{10}(\hat{\mathbf{n}}_6) \\ Y_{00}(\hat{\mathbf{n}}_4) & Y_{11}(\hat{\mathbf{n}}_5) & Y_{10}(\hat{\mathbf{n}}_6) \\ Y_{00}(\hat{\mathbf{n}}_4) & Y_{11}(\hat{\mathbf{n}}_5) & Y_{10}(\hat{\mathbf{n}}_6) \end{vmatrix}_{\downarrow}$$

By applying ladder operators formalism in the way described above one arrives to the following linear combinations of determinants $d_{\ell, m_{\ell}}$:

$$\begin{aligned} d_{2,1} &= \frac{1}{\sqrt{2}} \begin{vmatrix} Y_{00}(\hat{\mathbf{n}}_1) & Y_{11}(\hat{\mathbf{n}}_2) & Y_{1-1}(\hat{\mathbf{n}}_3) \\ Y_{00}(\hat{\mathbf{n}}_1) & Y_{11}(\hat{\mathbf{n}}_2) & Y_{1-1}(\hat{\mathbf{n}}_3) \\ Y_{00}(\hat{\mathbf{n}}_1) & Y_{11}(\hat{\mathbf{n}}_2) & Y_{1-1}(\hat{\mathbf{n}}_3) \end{vmatrix}_{\uparrow} \times \begin{vmatrix} Y_{00}(\hat{\mathbf{n}}_4) & Y_{11}(\hat{\mathbf{n}}_5) & Y_{10}(\hat{\mathbf{n}}_6) \\ Y_{00}(\hat{\mathbf{n}}_4) & Y_{11}(\hat{\mathbf{n}}_5) & Y_{10}(\hat{\mathbf{n}}_6) \\ Y_{00}(\hat{\mathbf{n}}_4) & Y_{11}(\hat{\mathbf{n}}_5) & Y_{10}(\hat{\mathbf{n}}_6) \end{vmatrix}_{\downarrow} \\ &+ \frac{1}{\sqrt{2}} \begin{vmatrix} Y_{00}(\hat{\mathbf{n}}_1) & Y_{11}(\hat{\mathbf{n}}_2) & Y_{10}(\hat{\mathbf{n}}_3) \\ Y_{00}(\hat{\mathbf{n}}_1) & Y_{11}(\hat{\mathbf{n}}_2) & Y_{10}(\hat{\mathbf{n}}_3) \\ Y_{00}(\hat{\mathbf{n}}_1) & Y_{11}(\hat{\mathbf{n}}_2) & Y_{10}(\hat{\mathbf{n}}_3) \end{vmatrix}_{\uparrow} \times \begin{vmatrix} Y_{00}(\hat{\mathbf{n}}_4) & Y_{11}(\hat{\mathbf{n}}_5) & Y_{1-1}(\hat{\mathbf{n}}_6) \\ Y_{00}(\hat{\mathbf{n}}_4) & Y_{11}(\hat{\mathbf{n}}_5) & Y_{1-1}(\hat{\mathbf{n}}_6) \\ Y_{00}(\hat{\mathbf{n}}_4) & Y_{11}(\hat{\mathbf{n}}_5) & Y_{1-1}(\hat{\mathbf{n}}_6) \end{vmatrix}_{\downarrow} \\ d_{2,0} &= \frac{1}{\sqrt{6}} \begin{vmatrix} Y_{00}(\hat{\mathbf{n}}_1) & Y_{10}(\hat{\mathbf{n}}_2) & Y_{1-1}(\hat{\mathbf{n}}_3) \\ Y_{00}(\hat{\mathbf{n}}_1) & Y_{10}(\hat{\mathbf{n}}_2) & Y_{1-1}(\hat{\mathbf{n}}_3) \\ Y_{00}(\hat{\mathbf{n}}_1) & Y_{10}(\hat{\mathbf{n}}_2) & Y_{1-1}(\hat{\mathbf{n}}_3) \end{vmatrix}_{\uparrow} \times \begin{vmatrix} Y_{00}(\hat{\mathbf{n}}_4) & Y_{11}(\hat{\mathbf{n}}_5) & Y_{10}(\hat{\mathbf{n}}_6) \\ Y_{00}(\hat{\mathbf{n}}_4) & Y_{11}(\hat{\mathbf{n}}_5) & Y_{10}(\hat{\mathbf{n}}_6) \\ Y_{00}(\hat{\mathbf{n}}_4) & Y_{11}(\hat{\mathbf{n}}_5) & Y_{10}(\hat{\mathbf{n}}_6) \end{vmatrix}_{\downarrow} \\ &+ \frac{2}{\sqrt{6}} \begin{vmatrix} Y_{00}(\hat{\mathbf{n}}_1) & Y_{11}(\hat{\mathbf{n}}_2) & Y_{1-1}(\hat{\mathbf{n}}_3) \\ Y_{00}(\hat{\mathbf{n}}_1) & Y_{11}(\hat{\mathbf{n}}_2) & Y_{1-1}(\hat{\mathbf{n}}_3) \\ Y_{00}(\hat{\mathbf{n}}_1) & Y_{11}(\hat{\mathbf{n}}_2) & Y_{1-1}(\hat{\mathbf{n}}_3) \end{vmatrix}_{\uparrow} \times \begin{vmatrix} Y_{00}(\hat{\mathbf{n}}_4) & Y_{11}(\hat{\mathbf{n}}_5) & Y_{1-1}(\hat{\mathbf{n}}_6) \\ Y_{00}(\hat{\mathbf{n}}_4) & Y_{11}(\hat{\mathbf{n}}_5) & Y_{1-1}(\hat{\mathbf{n}}_6) \\ Y_{00}(\hat{\mathbf{n}}_4) & Y_{11}(\hat{\mathbf{n}}_5) & Y_{1-1}(\hat{\mathbf{n}}_6) \end{vmatrix}_{\downarrow} \\ &+ \frac{1}{\sqrt{6}} \begin{vmatrix} Y_{00}(\hat{\mathbf{n}}_1) & Y_{11}(\hat{\mathbf{n}}_2) & Y_{10}(\hat{\mathbf{n}}_3) \\ Y_{00}(\hat{\mathbf{n}}_1) & Y_{11}(\hat{\mathbf{n}}_2) & Y_{10}(\hat{\mathbf{n}}_3) \\ Y_{00}(\hat{\mathbf{n}}_1) & Y_{11}(\hat{\mathbf{n}}_2) & Y_{10}(\hat{\mathbf{n}}_3) \end{vmatrix}_{\uparrow} \times \begin{vmatrix} Y_{00}(\hat{\mathbf{n}}_4) & Y_{10}(\hat{\mathbf{n}}_5) & Y_{1-1}(\hat{\mathbf{n}}_6) \\ Y_{00}(\hat{\mathbf{n}}_4) & Y_{10}(\hat{\mathbf{n}}_5) & Y_{1-1}(\hat{\mathbf{n}}_6) \\ Y_{00}(\hat{\mathbf{n}}_4) & Y_{10}(\hat{\mathbf{n}}_5) & Y_{1-1}(\hat{\mathbf{n}}_6) \end{vmatrix}_{\downarrow} \end{aligned}$$

Bibliography

- [1] S. Goyal, D. L. Schutt, and G. Scoles, *Phys. Rev. Lett.* **69**, 933 (1992).
- [2] C. Callegari, K. K. Lehmann, R. Schmied, and G. Scoles, *J. Chem. Phys.* **115**, 10090 (2001).
- [3] K. K. Lehmann and G. Scoles, *Science* **279**, 2065 (1998).
- [4] G. Scoles and K. K. Lehmann, *Science* **287**, 2429 (2000).
- [5] S. Grebenev, J. P. Toennies, and A. F. Vilesov, *Science* **279**, 2083 (1998).
- [6] J. Tang, Y. J. Xu, A. R. W. McKellar, and W. Jäger, *Science* **297**, 2030 (2002).
- [7] F. Paesani, A. Viel, F. A. Gianturco, and K. B. Whaley, *Phys. Rev. Lett.* **90**, 073401 (2003).
- [8] S. Moroni, A. Sarsa, S. Fantoni, K. E. Schmidt, and S. Baroni, *Phys. Rev. Lett.* **90**, 143401 (2003).
- [9] A. R. W. McKellar, Y. Xu, and W. Jäger, *Phys. Rev. Lett.* **97**, 183401 (2006).
- [10] J. Tang, A. R. W. McKellar, F. Mezzacapo, and S. Moroni, *Phys. Rev. Lett.* **92**, 145503 (2004).
- [11] S. Moroni, N. Blinov and P.-N. Roy, *J. Chem. Phys.* **121**, 3577 (2004).
- [12] W. Topic, W. Jäger, N. Blinov, P.-N. Roy, M. Botti and S. Moroni, *J. Chem. Phys.* **125**, 144310 (2006).

- [13] S. Baroni and S. Moroni, Phys. Rev. Lett. **82**, 4745 (1999).
- [14] S. Baroni and S. Moroni: *Reptation quantum Monte Carlo: a round-trip tour from classical diffusion to quantum mechanics*, in *Quantum Monte Carlo Methods in Physics and Chemistry*, edited by M. P. Nightingale and C. J. Umrigar, Kluwer Academic Publishers, 1999.
- [15] J. P. Toennies and A. F. Vilesov, Angew. Chem. **43**, 2622-2648 (2004).
- [16] M. Y. Choi, G. E. Douberly, T. M. Falconer, W. K. Lewis, C. M. Lindsay, J. M. Merritt, P. L. Stiles, and R. E. Miller, Int. Rev. Phys. Chem. **25**, 15-75 (2006).
- [17] F. Stienkemeier and K. K. Lehmann, J. Phys. B: At. Mol. Opt. Phys. **39**, R127-R166 (2006).
- [18] M. Barranco, R. Guardiola, S. Hernández, R. Mayol, J. Navarro, and M. Pi, J. Low Temp. Phys. **142**, 1 (2006).
- [19] S. Paolini, S. Fantoni, S. Moroni, and S. Baroni, J. Chem. Phys. **123**, 114306 (2005).
- [20] S. Paolini, *Rotational dynamics of molecular impurities solvated in ^4He clusters*, PhD thesis, Scuola Internazionale Superiore di Studi Avanzati, Trieste, 2006.
- [21] Y. J. Xu, W. Jäger and J. Tang, and A. R. W. McKellar, Phys. Rev. Lett. **91**, 163401 (2003).
- [22] J. Tang and A.R.W. McKellar, J. Chem. Phys. **121**, 181 (2004).
- [23] K. von Haeften, S. Rudolph, I. Simanovski, M. Havenith, R. E. Zillich, and K. B. Whaley, Phys. Rev. B **73**, 054502 (2006).
- [24] P. Cazzato, S. Paolini, S. Moroni, and S. Baroni, J. Chem. Phys. **120**, 9071 (2004).
- [25] J. Tang and A. R. W. McKellar, J. Chem. Phys. **119**, 754 (2003).
- [26] A. R. W. McKellar, J. Chem. Phys. **125**, 164328 (2006).

-
- [27] H. Hoshina, J. Lucrezi, M. N. Slipchenko, K. E. Kuyanov, and A. F. Vilesov, *Phys. Rev. Lett.* **94**, 195301 (2005).
- [28] S. Grebenev, B. Sartakov, J. P. Toennies, and A. F. Vilesov, *Science* **289**, 1532 (2000).
- [29] S. Grebenev, B. Sartakov, J. P. Toennies, and A. F. Vilesov, *Phys. Rev. Lett.* **89**, 225301 (2002).
- [30] D. Ceperley and M. Kalos, *Monte Carlo Methods in Statistical Physics*, editor K. Binder, Springer-Verlag, 1979.
- [31] M. Kalos, and P. Whitlock: *Monte Carlo Methods, Volume I: Basics*, Wiley, New York, 1986.
- [32] N. Metropolis, A. Rosenbluth, M. Rosenbluth, A. Teller, and E. Teller, *J. Chem. Phys.* **21**, 1087 (1953).
- [33] H. Risken, *The Fokker-Planck equation: methods of solution and applications*, Berlin Springer-Verlag, 1989.
- [34] G. Parisi, *Statistical field theory*, Addison-Wesley, 1988.
- [35] D. Ceperley, *Quantum Monte Carlo Methods*, Université de Lausanne, Lausanne, 1994.
- [36] P. Reynolds and D. Ceperley, *J. Chem. Phys.* **77**, 5593 (1982).
- [37] M. Casula, C. Filippi and S. Sorella, *Phys. Rev. B* **72**, 085121 (2005).
- [38] K. S. Liu, M. H. Kalos and G. V. Chester, *Phys. Rev. A* **10**, 303 (1974).
- [39] H. Trotter, *Proc. Am. Math. Soc.* **10**, 545 (1959).
- [40] R. Moszynski, T. Korona, P. E. S. Wormer, and A. van der Avoird, *J. Chem. Phys.* **103**, 321 (1995).
- [41] D. Blume, M. Lewerenz, F. Huisken, and M. Kaloudis, *J. Chem. Phys.* **105**, 8666 (1996).
- [42] C. de Michelis and L. Reatto, *Phys. Lett. A* **50**, 275 (1974).

- [43] C. Pierleoni, D. Ceperley, ChemPhysChem **6**, Iss. 9, 1872 (2005).
- [44] J. E. Gubernatis and M. Jarrell, Phys. Rep. **269**, 135 (1996).
- [45] S. Grebenev, M. Hartmann, M. Havenith, B. Sartakov, J. P. Toennies, and A. F. Vilesov, J. Chem. Phys. **112**, 4485 (2000).
- [46] M. Hartmann, R. Miller, J. P. Toennies, and A. F. Vilesov, Phys. Rev. Lett. **75**, 1566 (1995).
- [47] A. R. W. McKellar, J. Chem. Phys. **121**, 6868 (2004).
- [48] A. R. W. McKellar, Y. Xu, W. Jäger, and C. Bissonnette, J. Chem. Phys. **110**, 10766 (1999).
- [49] L. Surin, A. Potapov, B. Dumesh, S. Schlemmer, Y. Xu, P. Raston, and W. Jäger, Phys. Rev. Lett. **101**, 233401 (2008).
- [50] A. Conjusteau, C. Callegari, I. Reinhard, K. K. Lehmann, and G. Scoles, J. Chem. Phys. **113**, 4840 (2000).
- [51] K. Peterson and G. C. McBane, J. Chem. Phys. **123**, 084314 (2005).
- [52] T. G. A. Heijmen, R. Moszynski, P. E. S. Wormer, and A. van der Avoird, J. Chem. Phys. **107**, 9921 (1997).
- [53] K. K. Lehmann, J. Chem. Phys. **126**, 024108 (2007).
- [54] E. Krotscheck, V. Apaja, A. Rimnac, and R. Zillich, J. Phys: Condensed Matter **15**, 95 (2003).
- [55] E. W. Draeger and D. M. Ceperley, Phys. Rev. Lett. **90**, 065301 (2003).
- [56] R. N. Barnett and K. B. Whaley, J. Chem Phys. **99**, 9730 (1993).
- [57] F. Paesani and F. A. Gianturco, J. Chem. Phys. **116**, 10170 (2002).
- [58] C. Callegari, *Molecular rotation and dynamics in superfluid ^4He nanodroplets*, PhD thesis, Princeton University, 2000.
- [59] A. R. W. McKellar, J. Chem. Phys. **127**, 044315 (2007).

-
- [60] G. A. Parker and R. T. Pack, *The Journal of Chemical Physics* **64**, 2010 (1976).
- [61] M.-C. Chan and A. R. W. McKellar, *J. Chem. Phys.* **105**, 7910 (1996).
- [62] C. E. Chuaqui, R. J. Le Roy, and A. R. W. McKellar, *J. Chem. Phys.* **101**, 39 (1994).
- [63] D. Blume, M. Lewerenz, P. Niyaz, and K. B. Whaley, *Phys. Rev. E* **55**, 3664 (1997).
- [64] A. A. Mikosz, J. A. Ramilowski, and D. Farrelly, *J. Chem. Phys.* **125**, 014312 (2006).
- [65] T. G. A. Heijmen, R. Moszynski, P. E. S. Wormer, and A. van der Avoird, *J. Chem. Phys.* **107**, 9921 (1997).
- [66] R. E. Zillich, Y. Kwon, and K. B. Whaley, *Phys. Rev. Lett.* **93**, 250401 (2004).
- [67] K. K. Lehmann, *J. Chem. Phys.* **114**, 4643 (2001).
- [68] M. Barranco, J. Navarro, and A. Poves, *Phys. Rev. Lett.* **78**, 4729 (1997).
- [69] R. Guardiola, *Phys. Rev. B* **62**, 3416 (2000).
- [70] J. C. Slater, *Quantum theory of atomic structure*, Vol. 1, New York, McGraw-Hill, 1960.
- [71] T. Škrbić, S. Moroni, and S. Baroni, *J. Phys. Chem. A* **111**, 7640 (2007).
- [72] T. Škrbić, S. Moroni, and S. Baroni, *J. Phys. Chem. A* **111**, 12749 (2007).

Acknowledgments

I would like to use this opportunity to thank my supervisors Stefano Baroni and Saverio Moroni for their constant and overwhelming support that was crucial for me to arrive at this stage, to defend my PhD thesis, that was my big goal and dream. Last five years that I have spent in SISSA and Trieste will forever stay in my memory as one of the best years in my life. Also, I would like to thank all the friends that I have met here, and last, but not the least, my husband Branislav for his love and care.

Tatjana